Development and Characterization of Novel Garnet and Gold Thin Films for Photonic and Plasmonic Applications

A Thesis Submitted to the Faculty of the University of Minnesota

By

Prabesh Dulal

In Partial Fulfillment of the Requirements for the Degree of

Doctor of Philosophy

Adviser: Professor Bethanie J. Hills Stadler

August, 2017

Acknowledgements

I express my sincere gratitude to my friends, colleagues and family who have supported me directly and indirectly throughout graduate school. Thanks to my adviser Prof. Beth Stadler, whose expert guidance along with an equally amiable personality made graduate school a stimulating experience, both academically and personally.

Thanks to the past and present members of the Stadler group, especially to Dr. Andy Block and Dr. Eliot Estrine who helped me get up to speed with various aspects of my research. Thanks to all the technical assistance provided by the staff of University of Minnesota Nanofabrication center and the University of Minnesota characterization facility.

Thanks to my undergraduate adviser, Prof. Steve (Doc) Feller for introducing me to the world of science and engineering and continuing to provide me with guidance and advice.

Thanks to my parents, Hari and Radhika Dulal and my sister, Pratistha Dulal for the unconditional love and unwavering belief in me.

Abstract

The massive amount of data that we produce and share today is the result of advancements made in the semiconductor and magnetic recording industries. As the number of transistors per unit area in integrated circuits continues to rise, power dissipation is reaching alarming levels. Photonics, which essentially is a marriage of semiconductor with laser technology has shown great promise in tackling the issue of power dissipation. The first part of this work focuses on optical isolators, which are essential to halt back-reflections that interfere with the laser source of the photonic systems. Novel terbium iron garnet thin-film optical isolators have been developed on semiconductor platforms and their magneto-optical properties are explored. Modesolver and finite-difference simulations are done to assess their device-feasibility and efficiency. Subsequently, a new photonic device has been developed using current semiconductor microelectronic fabrication techniques.

Advancement in magnetic recording is equally vital to keep up with the demand for more data at faster speeds as the current perpendicular recording technique is fast-approaching its areal density limitations. Heat assisted magnetic recording (HAMR) is the next step in the evolution of hard drives. HAMR involves heating of magnetic media using plasmonic near field transducers (NFTs), which must be able to withstand elevated temperatures for extended times. The second part of this work presents a statistical crystallographic study of thermally induced deformation of Au NFTs. Subsequently, the

most thermally stable crystallographic orientation for Au NFT has been determined that could lead to significant improvements in HAMR drive reliability.

Table of Contents

List of Figures

List of Equations

List of Tables

1 Introduction

An infographic from Intel corporation, illustrated in Figure 1-1 shows that in 2013, there was 4 ZB of digital data produced and over 1.5 billion GB transferred worldwide every minute. 2017 is projected to bring 3 times more connected devices than people on Earth leading to a thirteen-fold growth in mobile traffic compared to 2012 [1]. These astronomical figures can be attributed to the omnipresence and every growing usage of the internet.

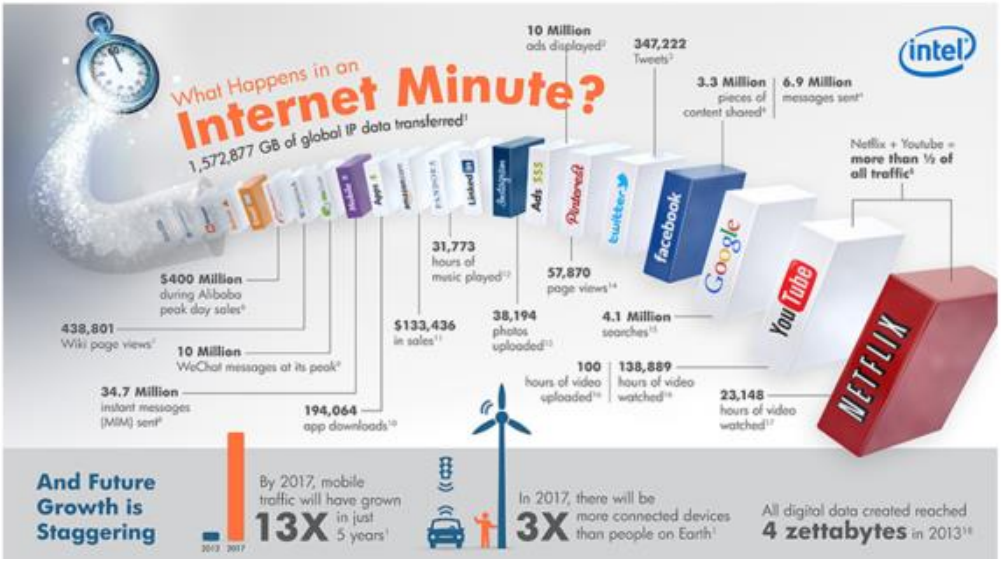

Figure 1-1: What happens in an internet minute? Intel's look at 2013-2017 [1].

Advancement in semiconductor technology is the forerunner of the exponential growth of digital data shown in Figure 1-1. Guided by Moore's law, which was an observation made by Intel's co-founder Gordon Moore in 1965 that the number of transistors on integrated circuits (and hence the computing performance) doubled every year. Following Moore's prediction, the transistor count per unit area has increased from

~1000 in 1970 to over 10 billion today [2]. However, with this exponential increase in number of transistors, the power being dissipated by integrated circuits is reaching alarming levels. An alternative technology is quickly required to keep up with the ever-growing need for more computing speed. The first part of this thesis discusses how photonics, which is essentially the marriage of semiconductors with optics and lasers is a promising solution to this problem.

Another contributor to the data increases presented in Figure 1-1 is the advancement in magnetic storage technology. While the semiconductor industry was making great progress processing data using integrated circuits, the magnetic recording industry was exploring ways to store data using hard drives. One of the first breakthroughs came in 1956 when IBM developed the first hard disk drive which had 5MB of storage capacity [3]. Today, Seagate has 12TB drives commercially available [4]. The traditional measure of hard disk drive capacity is the areal density, which loosely refers to the data that can be stored per unit area of the drive media. Like the growth in the number of transistors per Si chip, areal density of hard drives has also doubled every 3 years since 1955. However, moving forward, the superparamagnetic limit poses a serious threat to this growth trend [5]. The second part of this thesis discusses the application of plasmonics for HAMR (Heat assisted magnetic recording) which promises potential solutions to the current challenges in magnetic recording.

1.1 Photonics: Merging optics and semiconductor technology

1.1.1 Optical Fibers and telecommunication

The commercial development of fiber optics in the 1970s revolutionized the field of telecommunications. With broader bandwidth, insusceptibility to electromagnetic interference, low transfer loss and minimal heat dissipation, fiber optics has continued to allow for much faster transfer of data over greater distances with high security and efficiency as compared to copper wires [6].

1.1.2 Semiconductor technology

Semiconductor technology is one of the most important innovations of the past century. The ever-growing impact of computers on all aspects of the society has led to the surging need for smaller and faster devices. Governed by Moore's law, VLSI (very large scale integration) technology has seen a monumental increase in the number of transistors per square inch on integrated circuits. As the of density of electronic wires in integrated circuits increases exponentially, the resistance and hence the power density and heat dissipation also rise accordingly [7]. Additionally, there is the problem of interconnect bottleneck, which refers to the diminished performance of integrated circuits due to the connection between different components rather than due to the internal speed of individual components [8]. Due to these complications, VLSI technology is rapidly approaching its physical limitations.

1.1.3 Integrated photonics

Since fiber optics offers low power dissipation and wide bandwidth, the idea of replacing electronic interconnects with optical interconnects between integrated circuits is not only becoming increasingly popular, but also a necessity for the semiconductor industry to keep up with the growing demand for computing power. This integration of Si semiconductors and optical interconnects is broadly termed as silicon photonics. This field has garnered much attention today because it has been shown that photonics integration can be achieved using the microelectronic fabrication techniques that are already being used in the semiconductor industry. An example is the 100 Gbps silicon photonics optical transceivers developed by both IBM [9] and Intel [10] , who have been actively involved in the integration of optical components on semiconductor platforms in recent years.

1.1.4 Components of Integrated photonic circuits

An optical communication system comprises of several components [11]; lasers to generate the photons, modulators to imprint signal on the photons, waveguides to propagate the photons, and detectors to extract the signal. Also needed are optical multiplexers (to combine) and demultiplexers (to separate) different wavelengths for high bandwidth data transmission. Amplifiers are needed for long distance propagation and optical isolators are required to prevent back reflections and stabilize lasers. Today, almost all the components are capable of being CMOS (complementary metal oxide semiconductor) integrated [12]. What is still lacking is an optical isolator that can be monolithically integrated with semiconductor platforms.

1.1.5 Optical Isolators

When light travels through two different materials with different refractive indices, there occurs a significant amount of loss due to back reflection. This phenomenon can be explained by Equation 1.1, where *R* is the back reflection at any given interface and n_1 and n_2 denote the refractive indices of the materials on either side of the interface [13]. For an example when light enters from air (n_1=1) into a silicon waveguide (n_2=3.5), 31% of the light is lost due to the reflection from the interface as calculated from Equation 1.1.

$$\%R = \left[\frac{n_1 - n_2}{n_1 + n_2}\right]^2 \times 100\%$$

Equation 1.1: Reflection due to the mismatch in refractive index.

An optical isolator is the optical analogue of an electronic diode which only allows light to propagate in the forward direction, and it blocks all back reflections. Without an optical isolator, these back reflections will cause detrimental impact on the laser cavity. Some examples of the effect of unwanted feedback in the laser cavity are: spurious amplification, intensity instability and frequency jumps [14].

Figure 1-2 (a) shows the image of a commercially available bulk isolator, and Figure 1-2 (b) is the schematic showing its different components. A bulk isolator consists of garnet films, a permanent magnet and a polarizer. When a linearly polarized beam passes through an isolator (forward propagation) under the application of a magnetic field, its polarization rotates by 45° as it passes through the garnet film. This is demonstrated by

a clockwise rotation in Figure 1-2 (c). Any back reflections will go back through the garnet crystal, where it will be rotated 45° counter-clockwise with respect to the reflected beam. This is 45° clockwise with respect to the laser source, resulting in a total of 90° from the initial beam, and hence this back reflected polarization can be blocked by a polarizer without impacting the transmission of the forward propagating signal.

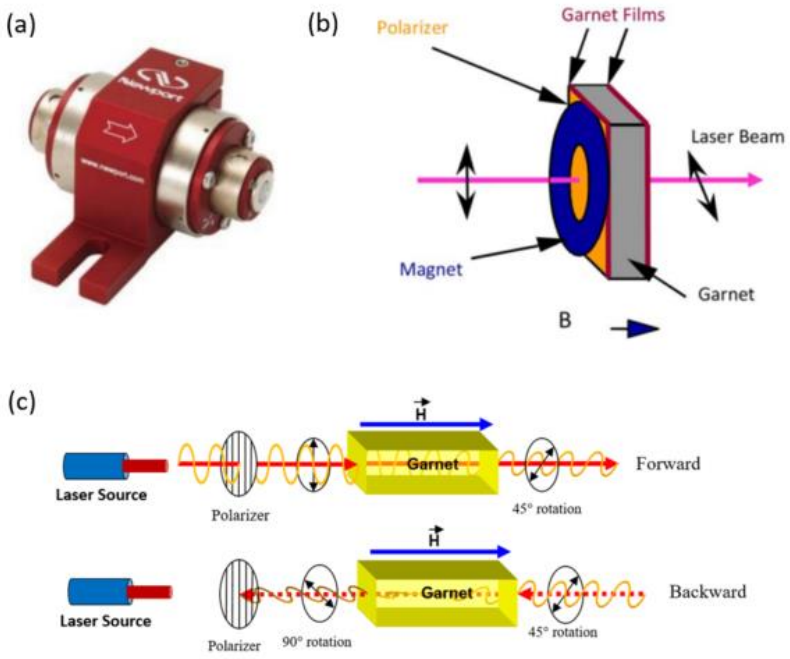

Figure 1-2: (a) A commercially available bulk optical isolator from Newport [15] , (b) Schematic showing the different components [13] and (c) operating principle of a bulk isolator (adapted from Sang-Yeob Sung's Ph.D. thesis) [16]

1.1.6 Faraday rotation

A linearly polarized light beam is equivalent to the combination of two equal but opposite circularly polarized beams. When this beam is passed through a magnetized material, it experiences a phenomenon called Zeeman splitting, which leads to the

splitting of the dispersion curve of the two polarizations. This leads to a difference in refractive index, and hence a difference in velocity for the two polarizations. This difference is termed as the magneto-optic circular birefringence, more commonly known as Faraday rotation (FR) because this results in the rotation of the linear polarization caused by the Faraday Effect.

Faraday rotation can be mathematically represented using off diagonal terms in the dielectric tensor (ε) in Equation 1.2

$$\varepsilon = \begin{bmatrix} n^2 & 0 & i\varepsilon_{xz} \\ 0 & n^2 & 0 \\ -i\varepsilon_{xz} & 0 & n^2 \end{bmatrix}$$

Equation 1.2: The dielectric tensor

Here, the diagonal components ($\varepsilon_{XX}=\varepsilon_{YY}=\varepsilon_{ZZ}$) are essentially the squares of the index of refraction of the material, $i = \sqrt{-1}$, n is the refractive index of the magneto-optical material and ε_{xz} is related to the Faraday rotation as Equation 1.3.

$$\varepsilon_{xz} = \frac{n\lambda\theta_F}{\pi}$$

Equation 1.3: Relationship of the off diagonal component with Faraday Rotation.

Faraday rotation (θ_F) depends upon three different components, the magnetization of the material (M), thickness of the material (d) and a material constant called the Verdet constant (V) as shown in Equation 1.4. For a magnetically saturated material, Faraday

rotation has units of °/cm, signifying the amount of rotation per unit length (or thickness) of the material.

$$\theta_F = VdM$$

Equation 1.4: Faraday rotation

1.1.7 Magneto-optical materials

For optical isolator applications, low optical loss is equally as important as good magneto-optic properties. These are the two main criteria used to gauge the feasibility of a material for optical isolator applications. Mathematically, the figure of merit (FoM), given by Equation 1.5, can be used to combine the two criteria in order to compare materials, where θ_F is the Faraday rotation and α is the absorption coefficient (both per unit length).

$$FoM = \frac{\theta_F}{\alpha}$$

Equation 1.5: Figure of Merit

Iron garnets offer both high θ_F and low loss at the optical communication wavelength (1550nm) and hence are the most widely used material for this application. Although maghemite, an iron based perovskite [17] and cobalt ferrite [18] exhibit high θ_F , they also have high values of α, and hence don't produce high FoM.

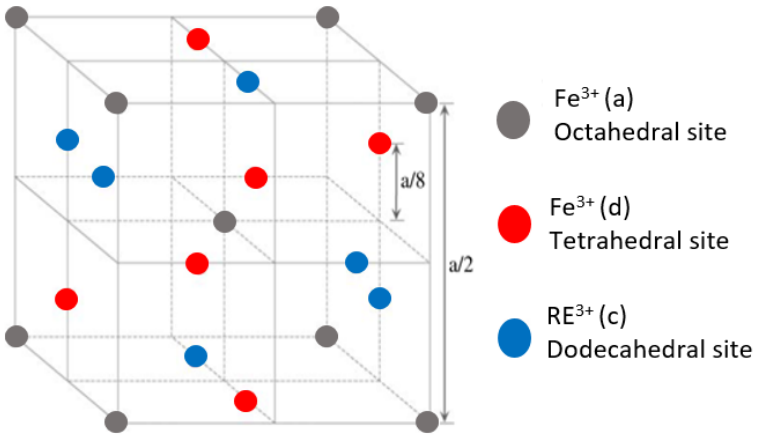

Figure 1-3: Schematic of the garnet unit cell showing the position of the different cations.

A rare-earth iron garnet ($C_3A_2D_3O_{12}$) has a complex crystal structure, containing three cation sublattices as shown in Figure 1-3. Here the rare-earth ions (valence =3^+) are present in the dodecahedral (c) sites. Fe^{3+} ions are situated in the octahedral (a) sites and the tetrahedral (d) sites. The Fe^{3+} ions in the two different sites are coupled antiferromagnetically. However, they do not have equivalent spins. This leads to the ferrimagnetic behavior that garnets exhibit. The net magnetization and Faraday rotation of the material depends upon the contribution of each sublattice which is temperature and wavelength dependent and is represented by Equation 1.6. Here c(λ), a(λ) and d(λ) are the wavelength dependent magneto-optic coefficients. M_c (T), M_a (T) and M_d(T) are the magnetizations of the dodecahedral, octahedral and tetrahedral sublattices respectively (Figure 1-3).

$$\theta_F(T,\lambda) = c(\lambda)\, M_c(T) + a(\lambda)\, M_a(T) + d(\lambda)\, M_d(T)$$

Equation 1.6: Sublattice contributions to Faraday rotation.

Among the different rare earth iron garnets used for isolators, yttrium iron garnet (YIG) is the one of the most extensively used for optical isolator applications [19]. While the Faraday rotation of pure YIG at 1550nm is only 200 °/cm [20], doping YIG with rare earth ions, which substitute the Y^{3+} ions by entering the dodecahedral sites, significantly enhances its magneto-optical properties. For an example, Bi doped YIG (Bi:YIG) films have -1700 °/cm [21] and Ce-doped YIG (Ce:YIG) films exhibit -1100 °/cm [22] to -4500 °/cm [23], depending upon various factors like growth conditions, dopant concentration and substrate choice. Per convention, a positive sign of Faraday rotation denotes that the material rotates the polarization right handed around the magnetic field and vice versa.

1.1.8 Waveguide device and birefringence

Waveguide isolator devices are made by integrating garnet materials with semiconductors. Apart from the magneto-optical properties of the garnets, the performance of these devices also heavily relies upon the geometry of a waveguide.

Figure 1-4 shows how the Faraday rotation in a waveguide with a rectangular cross section compares to one with a square cross-section. Due to the anisotropy in shape, the modal propagation constants for the orthogonal transverse electric (TE) and transverse magnetic (TM) modes are different in a non-square waveguide. This difference disallows a monotonic conversion between the TE and TM modes, which is required to achieve Faraday rotation. A square waveguide on the other hand leads to

optical isolation because the propagating energy can fully convert from one mode to the other. However, due to limitations in lithography, a perfectly square waveguide can't be guaranteed. Low fabrication tolerance will hamper optical isolation.

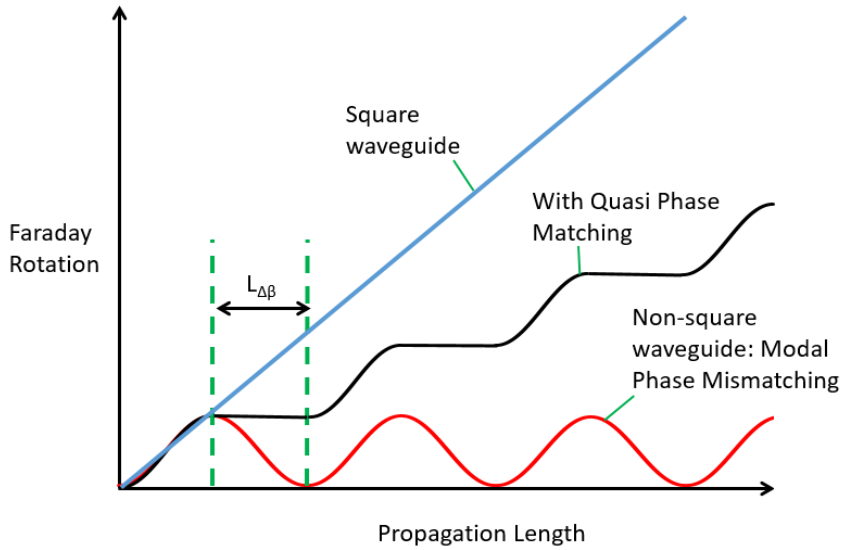

Figure 1-4: Schematic showing the effects of phase velocity mismatch and the solution: quasi phase matching (QPM).

Many researchers have taken different approaches to tackle this problem. Tien *et. al.*, proposed a waveguide model with periodic regions of reversed Faraday rotations using a serpentine top conductor to periodically reverse the magnetization in the garnet waveguide. They argued that the back and forth pattern would compensate for the shape birefringence, resulting in a 45° Faraday rotation if the period of the conductor matched the beat length of the waveguide [24], [25]. This model led to the development of the first magneto-optic waveguide modulator which used a serpentine electric circuit with YIG grown on a lattice matching $Gd_3Ga_5O_{12}$ substrate [26]. In this device, the

magnetic field switches periodically following the right-hand rule of electricity and magnetism, so the polarization of light at the output of the isolator has been rotated by 45° due to the current traveling through the serpentine conductor.

Murata *et. al*. were able achieve a 100% TE-TM mode conversion with just 8 Oe field using liquid phase epitaxy (LPE) grown $(BiNdLu)_3$ $(FeAlLu)_5O_{12}$ films by controlling stress and growth induced birefringence [27]. A different approach was taken by Wolfe *et. al*., who proposed to tackle the problem of birefringence by exploiting the compensation temperature of garnets [28]. The Faraday rotation of garnet is negative above its compensation temperature and positive below its compensation temperature. Inspired by the idea of periodic reversal of Faraday rotation, Wolfe *et. al*. used laser annealing of garnet films to create permanent reversal of the sub-lattice magnetizations. They made use of Ga^{3+} ions doped in YIG films, which upon annealing diffused from tetrahedral to octahedral sites (refer to section 1.1.7) giving rise to a film with two compositions that were periodically below and above the compensation temperature of YIG.

Here, quasi-phase matching (QPM) technique is explored in a new way to cope with shape induced birefringence. As seen from the red curve in Figure 1-6, the polarization rotation in a non-square waveguide reaches a peak and then reverts back to zero periodically due to the shape-induced modal phase-mismatching. QPM waveguide employs a periodic structure to allow for a phase mismatch over a coherence distance (also called half beatlength, $L_{\Delta\beta}$) but prevents the conversion in the wrong (downward in Figure 1-4) direction, hence preventing the polarization rotation from reverting back to zero as it travels through the waveguide. In the case of an SOI (Silicon on Insulator)

waveguide, QPM was achieved by using a periodic upper cladding that alternates between magneto-optic (MO) garnet and a non-magnetooptic (non MO) material. A schematic of such device is shown in Figure 1-5.

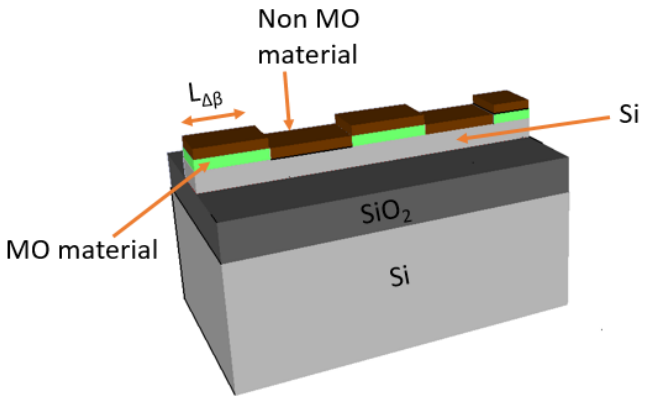

Figure 1-5: Schematic of quasi phase matched (QPM) SOI waveguide.

1.1.9 Photonics work in this thesis

Chapter 3 of this thesis shows that although the use of YIG as seedlayer allows for the growth of better magneto-optic Bi:YIG and Ce:YIG, there are negative implications of this seedlayer when it comes to developing monolithically integrated waveguide devices with garnet claddings. Alternative seedlayers are explored and new materials that don't require any seedlayers are also presented. Later in chapter 3, two different types of optical isolator devices are introduced; one type has garnet claddings on Si waveguides and the other has garnet on quartz substrates. Quasi-phase-matching (QPM) is explored for both types of devices to overcome birefringence. Chapter 4 presents a study where the Faraday rotation of garnet isolators is enhanced by developing them as Fabry-Perot interferometers.

1.2 Plasmonics for next generation of magnetic recording

1.2.1 History of magnetic recording

Magnetic recording refers to the storage of data in the form of electric signals by selectively magnetizing different portions of a magnetic material. The history of magnetic recording can be traced back to 1844 when Samuel F.B. Morse sent the phrase “What hath God wrought!” in the form of an electric signal from Washington to Baltimore [30]. In 1898, Valdemar Poulsen developed the world's first working magnetic recorder called the Telegraphone [31]. This paved way for the many new technologies. The revolution in magnetic recording that has literally changed the way the world works. Fast forward to today, the field has made quantum leaps because of its application in computers, which began in 1956 with the development of the first hard disk drive by IBM [3].

1.2.2 Magnetic recording technology today

Hard drives currently dominate the magnetic storage device market. As of 2017, most hard drives are developed using perpendicular magnetic recording technology [32] whose schematic is shown in Figure 1-6. The system comprises of three components: recording head, recording medium and the read head. The recording head comprises of an electromagnet that moves across the recording medium and 'writes' bits selectively in the media. The read head uses a GMR (giant magneto-resistance) or TMR (tunneling magneto-resistance) based read sensor and provide access to the stored data.

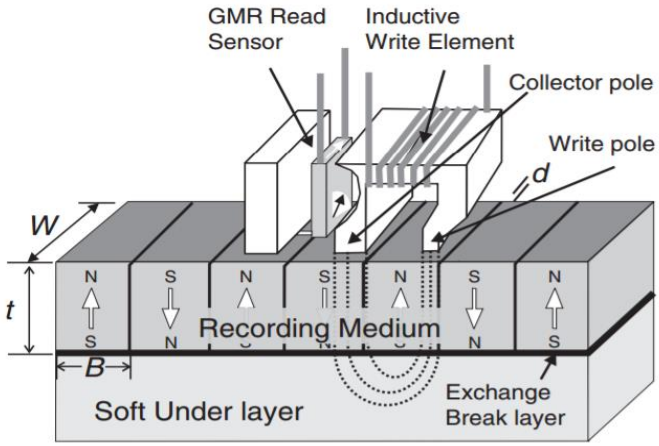

Figure 1-6: Schematic of a perpendicular magnetic recording system [32].

1.2.3 Areal density

As computers became faster, yet smaller and more portable over the years, magnetic storage devices had to follow the same trend. The demand was to increase the storage capacity while reducing the device size. This is quantified by the recording industry using the term “areal density”, which refers to the number of bits stored per unit area of the recording medium. Thanks to the technological innovations made along the way, there has been an exponential increase in magnetic areal storage density in the last 60 years. Figure 1-7 shows that the areal density has doubled every 3 years since 1955 [5].

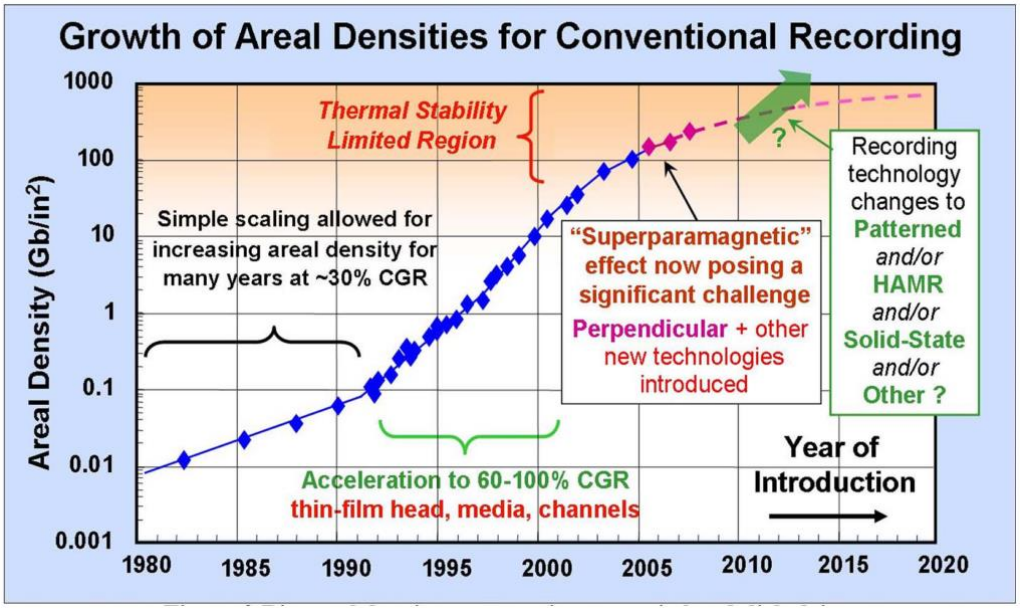

Figure 1-7: Bit areal density progress over the years in magnetic storage devices [5].

1.2.4 Superparamagnetic limit

In the recent years, there has been a lot of focus on increasing areal density by reducing the size of an individual magnetic bit. A major consideration while doing this is the signal to noise ratio (SNR). The SNR is proportional to the number of magnetic grains (N) in a bit as shown by Equation 1.7. Therefore, to preserve the SNR, the grains comprising the individual bit also need to get smaller as the size of each magnetic bit gets smaller.

$$SNR = \log(N)$$

Equation 1.7: Signal to noise ratio.

The problem however is that as the grains get smaller the magnetization of the grains can be affected by temperature fluctuations that cause random flipping of their

magnetic moments [33], [34]. This phenomenon is termed as the “superparamagnetic limit”, which as shown in Figure 1-7 is posing a serious threat to the progress in areal density [35].

The criteria for stability in magnetic recording is shown by Equation 1.8, where K_u is the magnetic anisotropy of the material (media), *V* refers to the grain size, k_B is the Boltzmann constant and *T* is the temperature.

$$\frac{K_u V}{k_B T} > 70$$

Equation 1.8: Criteria for thermal stability.

This relation suggests that if *V* is reduced, higher K_u is needed to achieve thermal stability in recording. However, as shown by Equation 1.9, increasing K_u means that higher field (H) is required for writing.

$$H = \frac{2K_u}{M_S}$$

Equation 1.9: Writability: relationship of write field with anisotropy.

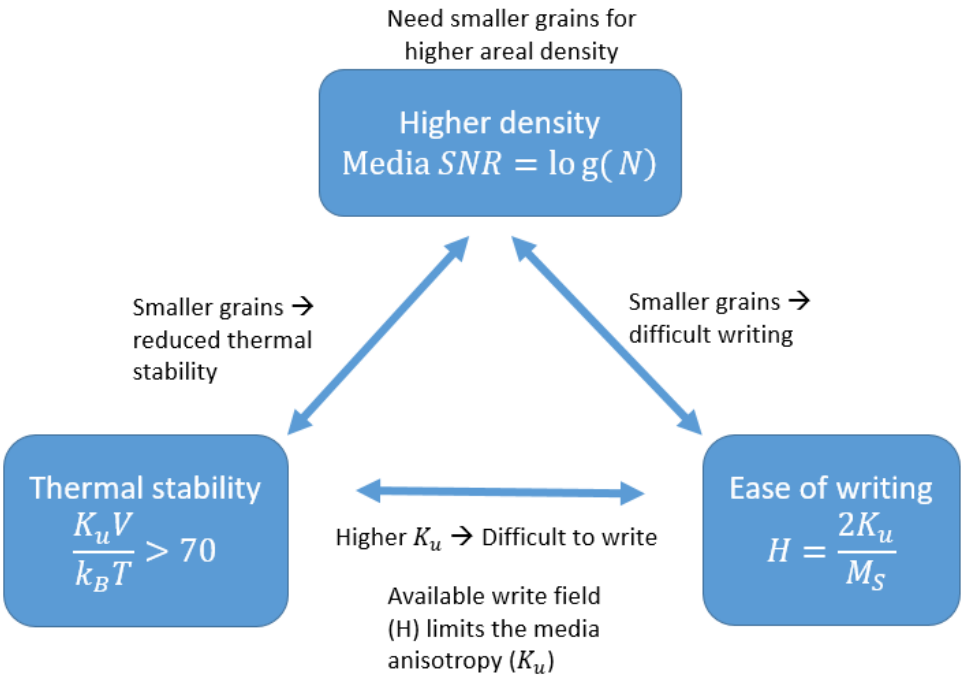

Figure 1-8: The magnetic recording trilemma.

Today, high K_u materials like FePt have been developed with grain sizes as small as 3 nm [34], [36]. However, the magnetic coercivity of such high anisotropy materials is larger than the field that can be generated by the current recording head. This means that the data cannot be stored in these materials unless the magnetic coercivity of the recording media is lowered. These essential considerations for magnetic recording are collectively referred to as the 'magnetic recording trilemma' and is summarized in Figure 1-8.

1.2.5 Heat assisted magnetic recording (HAMR)

HAMR is the technology that puts forward a solution to the current magnetic recording trilemma. The working principle of HAMR is showed in Figure 1-9. A very precise thermal

spot is created in the media by focusing the electromagnetic energy from a laser. This thermal energy increases the temperature of the media. As the temperature comes close to its Curie temperature, the coercivity of the media drastically reduces, consequently reducing the field required to write the data [33], [34]. After writing is complete, the heating process is ceased and the recording media is rapidly cooled to room temperature using a heat sink. This allows for the material to come back to the state of maximum anisotropy and coercivity and hence the data is permanently stored. The signal is read back by using a TMR (Tunneling magnetoresistance) based read sensor.

Hence, employing thermal treatment, HAMR proposes a solution to the magnetic trilemma allowing for smaller grains with high anisotropy by reducing the required write field.

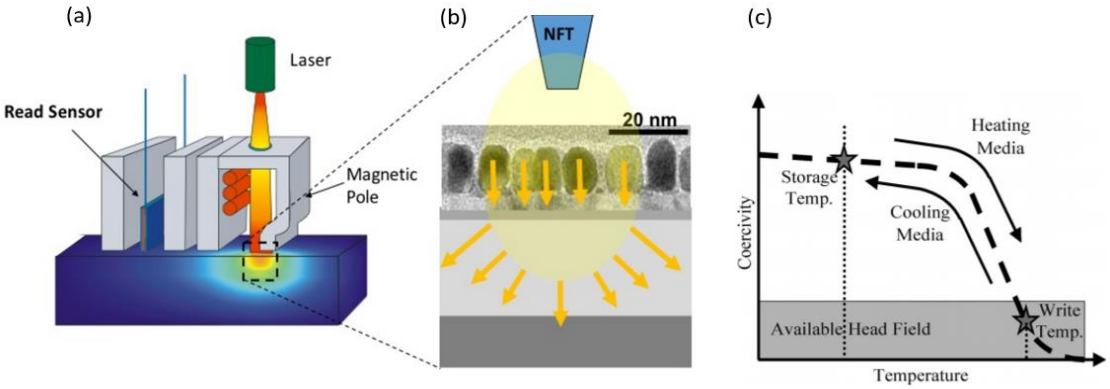

Figure 1-9: Schematic of heat assisted magnetic recording [33], [37].

1.2.6 Light delivery in HAMR

Light delivery for HAMR is done by using a waveguide that transports the electromagnetic energy coming from a laser as shown in Figure 1-9 (a). For high areal density, this energy is radiated and converted into thermal energy creating a hot spot in the media where the bit is written. Hence the hot spot must be very precise, in the order of a new nanometers. One of the early approaches to light delivery was the solid immersion lens [35], whose physics can be explained by the relation in Equation 1.10. Here, d is the minimum spot size, λ is the wavelength and NA is the numerical aperture of the focusing lens. The smallest value of d that can be achieved by this (diffraction limited) system was 240nm [33], which was not feasible for HAMR.

$$d = \frac{0.51\ \lambda}{NA}$$

Equation 1.10: Spot diameter in solid immersion lens technique [33].

To reduce the size of the thermal spot, another approach was taken by forcing the light through a subwavelength aperture [35]. However, reduction in the size of the aperture (d) also led to extremely low transmission efficiency (T) as explained by the relation in Equation 1.11.

$$T = \left(\frac{64\pi^2}{27}\right).\left(\frac{d}{\lambda}\right)^4$$

Equation 1.11: Transmission efficiency dependence on aperture size [35].

By this method, creating a thermal spot in the media would only be possible if there was a huge incident focused power which would require a very high power laser source. Using a high-power laser is obviously not possible as that would mean a bulkier and more expensive device and more energy to dissipate in the system. A different approach to increase the local incident power was explored by using plasmonics.

1.2.7 Plasmonics for Near Field transducers (NFTs)

Plasmonics refers to the study of the interaction between the electromagnetic field and free electrons in a metal. The electric component of the wave excites the free electrons causing them to have collective oscillations. By patterning the metal in specific geometries, the electromagnetic energy can be localized at its surface. With this approach, the diffraction limit, which restricts the localization of light into subwavelength dimensions in conventional optics can be avoided.

Plasmonic nanostructures are capable of producing high local power densities in a very efficient manner. This property can be utilized to couple the electromagnetic energy travelling through the waveguide of a HAMR writer into a near field transducer (NFT) made of a plasmonic material as shown in Figure 1-9 (b). This would allow for sub-diffraction-limited wavelengths to be focused in the media to create hot spots of a few nanometers dimensions. Hence, leading to high areal density [38].

1.2.8 Plasmonics work in this thesis

Several materials such as Au, Ag, TiN, ZrN etc have been investigated for the HAMR NFT application. Au is highly preferred because of its chemical stability, high melting point and high thermal conductivity [38]. However, the negative aspects of Au are its mechanical softness (high ductility) and its low energy barriers to surface diffusion. These are critical because plasmonic performance of the Au NFT is dependent upon its shape, which needs to remain intact while being heated to high temperatures.

The plasmonic work on this thesis (chapter 5) is dedicated to a crystallographic study for better understanding of the mechanical stability of the Au NFTs upon thermal treatment. At the end, the most durable orientation for Au NFT is proposed for operations in elevated temperatures.

2 Experimental and Simulation Methods

2.1 Thin film growth by sputtering

2.1.1 General working principle

Sputtering is a physical vapor deposition method used for the growth of thin films. It is a widely-used technique both in the semiconductor and disc-drive industries because of its reliability, scalability, range of materials and quality of films (density and adherence) [39].

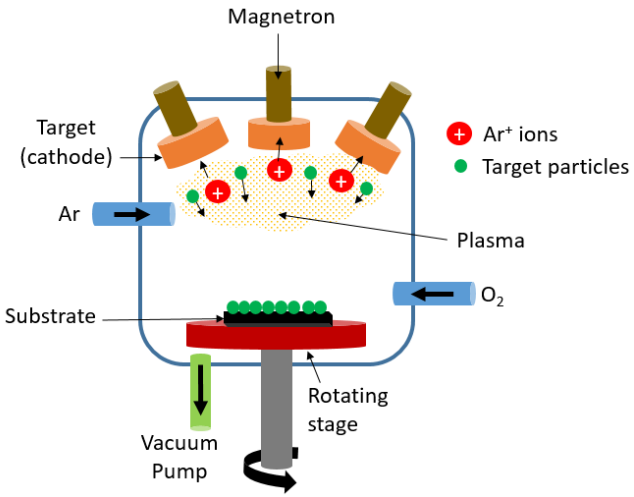

Figure 2-1: Schematic of thin film growth by sputtering.

Figure 2-1 shows the schematic of the sputtering process used for the growth of all the garnet films presented in this thesis. This setup is termed as sputter-down configuration. The deposition chamber consists of sputtering targets that are connected to the negative terminal. Subjecting Ar gas into an electromagnetic field creates a cloud of positively charged Ar ions hence producing the Ar plasma. The Ar^+ ions accelerate

towards the targets (cathodes). Upon collision, the kinetic energy of the ions is transferred into the atoms of the target, which are ejected and travel across the chamber to condense on the substrate as thin films.

2.1.2 Magnetron, RF, reactive and co-sputtering

Several modifications can be made in the sputtering process depending upon the application. The films discussed in this thesis were deposited using a combination of magnetron, RF (radio frequency) and reactive co-sputtering.

The collision of the charged ions with the target leads to the generation of secondary electrons from the surface of the target. A magnetron is placed behind each target to generate a donut-shaped magnetic flux at the surface, thus constraining the motion of the secondary electrons close to the target. This greatly increases the ionization efficiency [40] which creates a dense plasma in the vicinity of the target, leading to a faster deposition rate compared to non-magnetron sputtering.

If the material is electrically conducting, a DC power source can create a stable plasma. However, if the target material is non-conducting (eg: dielectrics or oxidized metal targets), the Ar^+ ions accumulate and charge the target, eventually terminating the plasma. This issue is resolved by applying a technique called RF sputtering, in which an AC power source (radiofrequency range) is used instead of DC. By applying the AC field, the positive charges accumulated during one half of the AC cycle can be neutralized by the electron bombardment in the next cycle. Because electrons are more mobile than

ions, the surface obtains a net negative charge, and a stable plasma can be achieved so dielectric films can be grown[41].

All the oxide films reported in this thesis were deposited by using reactive sputtering. O_2 gas was flowed into the system using a ring placed around the inner circumference of the chamber, surrounding the substrate holder. Depending upon the material, multiple targets were sputtered simultaneously. This process is termed as co-sputtering. The atoms of the metals ejected from the different targets react with oxygen and consequently deposit an oxide layer on the surface of the substrate.

2.1.3 Critical sputtering parameters

The quality and efficiency of reactive magnetron co-sputtering depends upon several parameters, some of which are: bias voltage, chamber pressure, Ar/O_2 ratio and target thickness.

The bias voltage is controlled by tuning the RF input power. During co-sputtering, a calibration is first performed by supplying each target with a different power to achieve the targeted film composition. While higher power leads to faster depositions, higher power also leads to significant heating of the targets, and hence special attention must be provided while sputtering materials that have a low melting point. For an example, Fe can be sputtered at 220W, but Bi has low melting point and should not be sputtered above 20W (2” diameter targets).

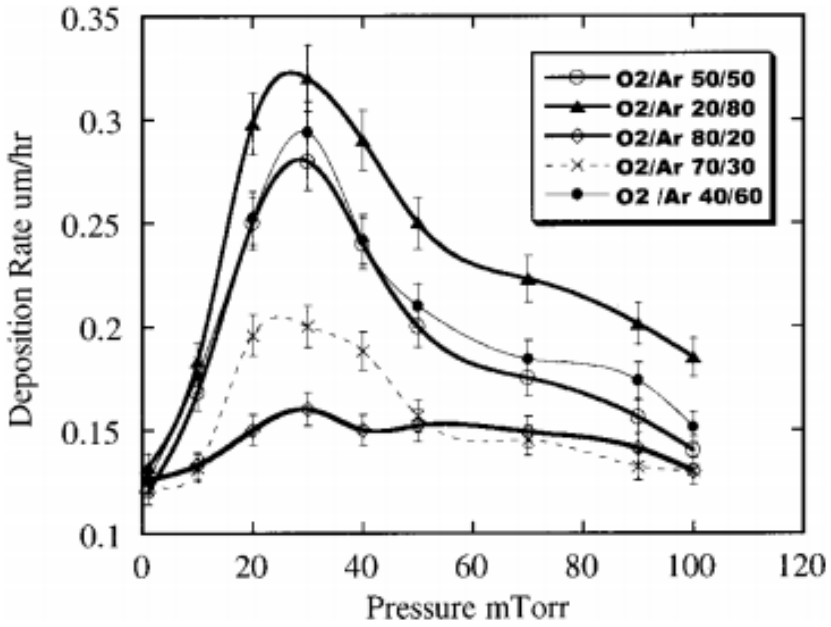

Figure 2-2: Dependence of deposition rate on chamber pressure and O2/Ar ratio for zirconium titanate thin films [42].

To ensure the purity and quality of the thin films, the chamber is first vacuumed to below $2x10^{-5}$ torr with the combination of a roughing (mechanical) and a turbo pump. Chamber pressure during deposition is another critical deposition parameter. At low pressures, the sputter yield is low because there are less number of Ar^+ ions to bombard the targets. The sputter yield rises as the pressure is raised because more ions are created to bombard the targets. However, if the pressure is too high, the number of neutral Ar atoms increases along with the increase in the number of Ar^+ ions. This leads to collisions and scattering in the plasma lowering the sputter yield [42]. Hence, it is important to find an optimal sputtering pressure. In the case of reactive sputtering with O_2, the ratio of O_2/Ar is critical as well. If the O_2 partial pressure is too high, the targets tend to oxidize, hence making them less conductive and lowering the sputtering yield.

The effect of chamber pressure and O_2/Ar ratio (partial pressure) is shown in Figure 2-2. The parameters here are specific to zirconium titanate films but the trend holds true for the deposition of all the oxide thin films developed in this work.

Target thickness is another important parameter for magnetic materials like Fe. If the target is too thick, the flux from the magnetrons is shunted inside the target such that it no longer extends into the plasma, hence leading to low sputtering rate.

Target	Thickness (in.)	Purity (%)	Power range (W)
Fe	0.0625	99.95	220-240
Tb	0.125	99.9	100-120
Y	0.250	99.95	100-120
Ce	0.250	99.9	20-60
Bi	0.250	99.999	0-10
Y_3Fe_5	0.250	99.95	240
Si	0.0625	99.95	100-250

Table 2-1: List of sputtering targets used for this work.

All the sputtering targets used for this work were 2.0" in diameter, obtained from Kurt J. Lesker. A table with their respective thicknesses, purity and range of sputtering power is given in Table 2-1. Deposition pressures for specific cases will be discussed in the results section.

2.2 Rapid thermal annealing

The as-deposited oxide films grown in this work were amorphous in nature and a post-anneal was required for crystallization and formation of the garnet phase. Previous work by Sung *et. al*. has showed that rapid thermal annealing (RTA) is preferred over

traditional furnace annealing because of its low thermal budget that provides for better compatibility with semiconductor device processing [43], [44]. In addition, the entire process takes a few minutes compared to hours in a traditional tube furnace.

The University of Minnesota Nano Center's RTA (model RTP-600) was used for this work. In the RTP-600 system, a Si wafer with the substrates placed on top is loaded into the heating chamber which consists of a small quartz lined chamber that is rapidly heated by high intensity, tungsten-halogen lamps. Samples are heated at a rate of 100-150°C/second, held at a fixed temperature (900°C for most garnets in this work) for 2 minutes and then cooled down at 100-150°C/second. Annealing was done while supplying 10 SLPM (standard liters per minute) of O_2 to facilitate the formation of the crystalline garnet phase.

2.3 X-Ray diffraction (XRD)

XRD was the primary characterization methodology used for the phase analysis of the films. To understand the methodology of phase analysis by XRD, it is first important to know the fundamentals of the crystal structure.

2.3.1 Crystal structure

The crystal structure of a material refers to the spatial arrangement of its atoms and molecules. For the ease of visualization, the atoms or ions of a crystalline structure are thought of as solid spheres with specific diameters. The term 'lattice' is used to describe

the three-dimensional array of points coinciding the positions of the spheres representing the atoms/ions. A crystal structure is formed by the repetition of a specific arrangement of atoms/ions. These smallest repeating entities are called 'unit cells'. The unit cell can have different geometries and can be classified into seven crystal systems: cubic, hexagonal, tetragonal, rhombohedral, orthorhombic, monoclinic and triclinic [45]. The two materials discussed here (garnet and gold) fall under the cubic category. Cubic geometry has all three axes of equal length and perpendicular to each other.

The arrangement of atoms in certain planes in the unit cell are described using the Miller indices (*hkl*). Some of the most basic and widely seen planes are shown in Figure 2-3. The Miller indices are used for the calculation of distance between two parallel lattice planes. This distance is denoted by the notation d_{hkl}, and is calculated by the relation shown in Equation 2.1, where *h,k,l* are the Miller indices and *a* is the lattice parameter of the crystal, which is the physical dimension of the unit cell.

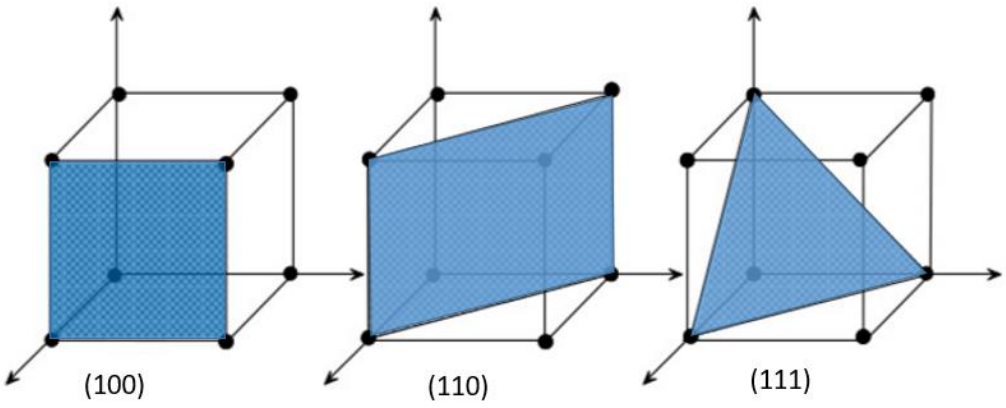

Figure 2-3: Miller indices for the three basic planes of atomic arrangements.

$$d_{hkl} = \sqrt{\frac{a^2}{h^2 + k^2 + l^2}}$$

Equation 2.1: Interplanar lattice spacing.

2.3.2 Bragg's law

When a material is subjected to X-ray radiation, the X-rays can scatter off its lattice planes. Interference occurring among the rays scattered from different lattice planes can be used to determine the crystal structure of the material. This can be explained with the help of the schematic shown in Figure 2-4 which is referred to as Bragg's condition.

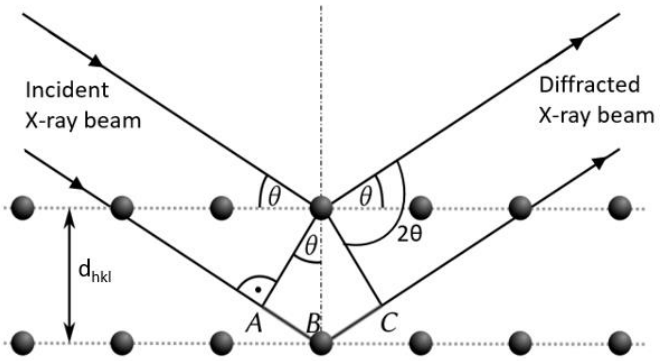

Figure 2-4: Schematic of the Bragg's condition.

Here, both the incident beam and the diffracted beam form an angle θ with the lattice planes. However, the ray that strikes the bottom lattice plane travels a slightly longer distance before scattering compared to the top lattice plane. From Figure 2-4, this extra

distance, ABC = $2d_{hkl}sin\theta$ since AB=BC=$d_{hkl}sin\theta$, where d_{hkl} is the spacing between the lattice planes. Figure 2-4 only shows 2 planes, but this distance consecutively gets extended for the rays that reflect off the 3rd, 4th, 5th planes and so on. Bragg's law states that when this extra distance is equal to an integer multiple of the wavelength of the incident x-rays, then there occurs a constructive interference that leads to the formation of a specific diffraction pattern that signifies the lattice spacing of the crystal. The mathematical representation of Bragg's law is given in Equation 2.2, where n is an integer value, λ is the wavelength of the X-rays, d_{hkl} is the lattice spacing and θ is the angle made by the incident beam with the lattice plane.

$$n\lambda = 2d_{hkl}sin\theta$$

Equation 2.2: Bragg's law for X-ray diffraction

If the Bragg's condition is not fulfilled at any angle, then there is no constructive interference, which signifies that there is no symmetric arrangement of atoms in the material. This is the case in amorphous or non-crystalline materials.

XRD phase analysis refers to the process of analyzing the specific diffraction patterns to determine the crystal structure of the specimen. All the XRD analysis carried out in this work was performed using University of Minnesota Characterization facility's Bruker D8 Discover 2D diffractometer, whose configuration is shown in Figure 2-5. A Co Kα source is used to generate the X-rays that are focused using a 0.8mm collimating tube. Sample is mounted on the translation stage and a goniometer is used to position the sample throughout the measurement.

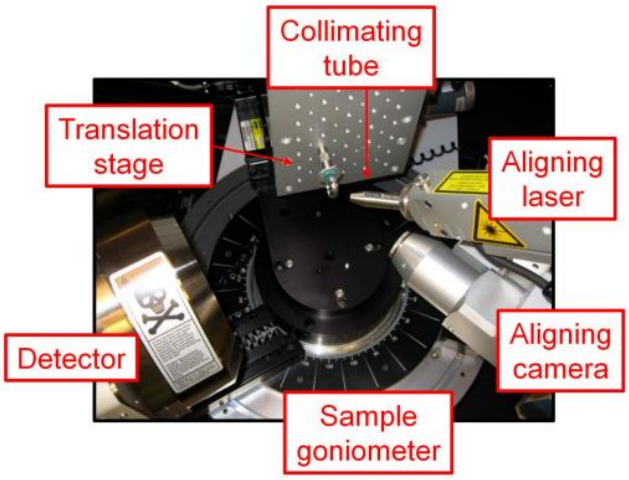

Figure 2-5: Geometry of Bruker 2D X-ray diffractometer [46].

The scattered x-rays coming from polycrystalline samples are projected onto the detector, and can be described in 3D space using the Ewald sphere shown in Figure 2-6. The direction of diffracted beam is defined by the angles 2θ (longitude) and Υ (latitude).

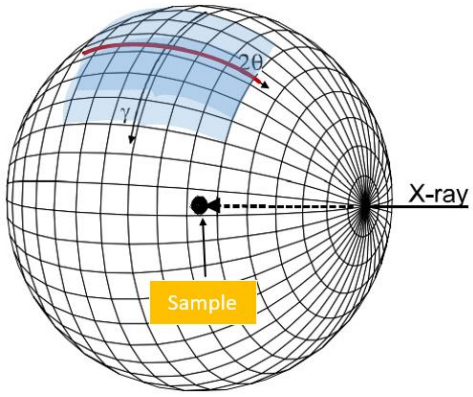

Figure 2-6: Ewald sphere representing the XRD scan. 1D detector covers only the red line and 2D detector covers the blue region. [47], [48].

In a conventional diffraction system, XRD patterns are only collected by a 1D detector. This only covers the equator of the Ewald sphere shown by the red arc in Figure 2-6. However, the 2D detector in the D8 discover can cover a large area of the Ewald sphere by simultaneously detecting both 2θ and ϒ angles (ϒ refers to the blue region in Figure 2-6). Hence, 2D XRD system allows for the characterization of crystal structures in a short, single scan [47], [48].

2.4 Scanning electron microscopy (SEM)

JEOL 6500 SEM was used for microscopic imaging of the garnet and gold films. In an SEM setup, an electron source, such as tungsten, is used to generate an electron beam. Using a combination of condenser lenses, the beam of electrons is focused to a precise spot on the sample surface. Once the electrons reach the surface, they interact with the sample and are either absorbed or scattered, producing a variety of signals. The scattered electrons cause the emission of secondary electrons (SE), backscattered electrons (BSE) or diffracted backscattered electrons (EBSD). Inelastically scattered electrons emit electromagnetic radiation (characteristic X-rays). SE provide information on the surface topography of the samples, EBSD can be used to determine the crystal structure, and the characteristic X-rays can be used for compositional analysis. These processes can be detected by specialized detectors.

2.5 Electron dispersive X-ray spectroscopy (EDS)

Oxford Inca X-Act EDS detector of University of Minnesota Nano center's JSM-6610LV SEM was used for the compositional analysis of the thin films. For EDS measurements, the incident electron beam must excite an inner shell electron in the sample material to a higher energy state, creating an electron hole in the process. An electron from the higher-energy shell descends to occupy the vacancy, during which it releases energy in the form of X-ray radiation. This emitted X-ray beam is collected by an EDS detector. The elemental composition of the specimen can be determined from the energy of the X-rays, which indicates the difference in energy between the two atomic shells and are element specific. Using this information, the compositions of the films can be determined.

2.6 Electron Backscattered diffraction (EBSD)

University of Minnesota characterization facility's EBSD system from Oxford Instruments HKL was used for the crystallographic analysis of the garnet and Au films.

The configuration of the EBSD system is shown in Figure 2-7. When the electrons coming from the SEM column diffract off the crystallographic planes of the sample material, they are projected upon the phosphor detector to create diffraction patterns which are governed by Bragg's condition (section 2.3.2). These patterns are termed as Kikuchi lines which, as shown in Figure 2-8, are characteristic to the spacings of the lattice planes. Hence, they can be used to determine a material's crystal structure.

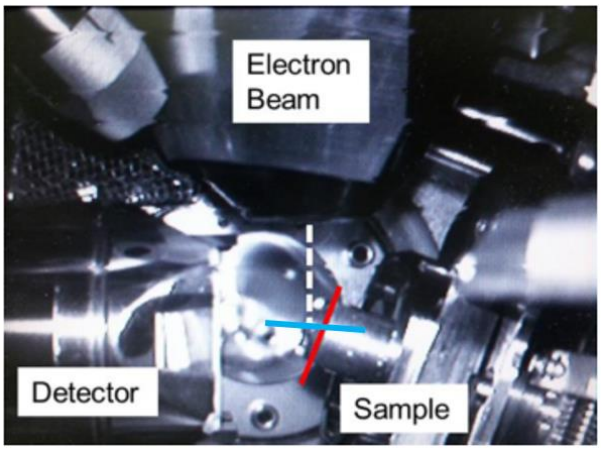

Figure 2-7: Electron backscattered (EBSD) system configuration. Picture courtesy: Eliot Estrine [49].

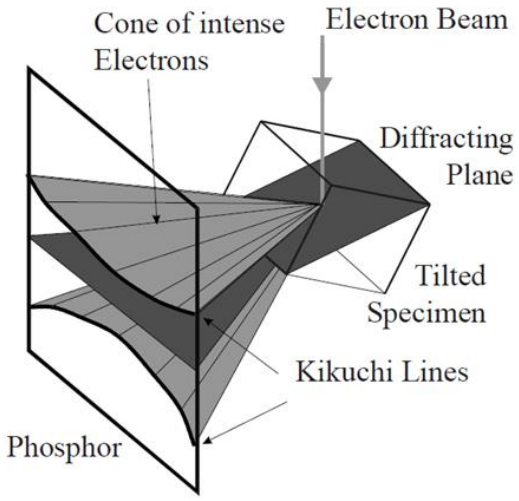

Figure 2-8: Diffraction cones, Kikuchi lines created by backscattered electrons.

For the study of garnet films, a conventional EBSD setup was used. In this setup, the samples were placed at a 70° tilt as shown by the red line in Figure 2-7. For the case of Au films, EBSD was done in a transmission setup (t-EBSD), also referred to as TKD.

2.7 Faraday rotation measurements

Faraday rotation measurements were performed using the optical configuration shown in Figure 2-9. In this arrangement, the path of the laser is represented by the red ray. The sample is mounted such that the film is normal to the propagation of light and is placed between the two home-made electromagnets. The polarizing beam splitter sends TE (Transverse electric)-polarized light to one detector and TM (Transverse magnetic)-polarized light to the other. The difference is found using a lock-in amplifier and is used to calculate Faraday rotation. A half wave plate is used to calibrate the measurements by rotating the light known amounts before and after applying the magnetic field.

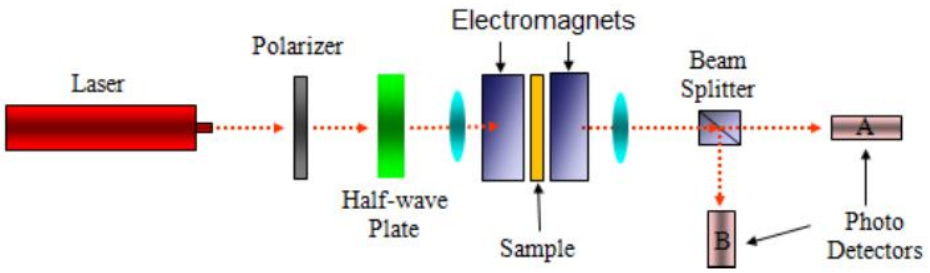

Figure 2-9: Schematic of Faraday rotation measurement setup.

The data from the two detectors is collected by a National Instruments (NI) module using Lab-view software. The field is measured by a DC Gaussmeter.

The raw data obtained from the detector is in millivolts. This is later converted into degrees of rotation by scaling the voltage signal of the rotation data obtained by

switching the field with the voltage signal obtained by the rotation of the half-wave plate with zero applied field.

An example of the Faraday rotation calculation procedure is shown in Figure 2-10. Here, a 1550nm laser is used. The field is switched from 0 to 3000 Oe, back to zero followed by -3000 Oe and zero. The half wave plate is rotated 0.01 ° per turn. The Faraday rotation (θ_F) is obtained by the relation shown in Equation 2.3, where a is the change in the TE-TM signal while switching the field from 0 to 3000 Oe (or from -3000 Oe to 0). TE-TM denotes the difference in the signal obtained from the two detectors, b denotes the average change in TE-TM signal obtained by the multiple rotations of the half-wave plate, c is the rotation of the half-wave plate in degrees and t denotes the thickness of the sample.

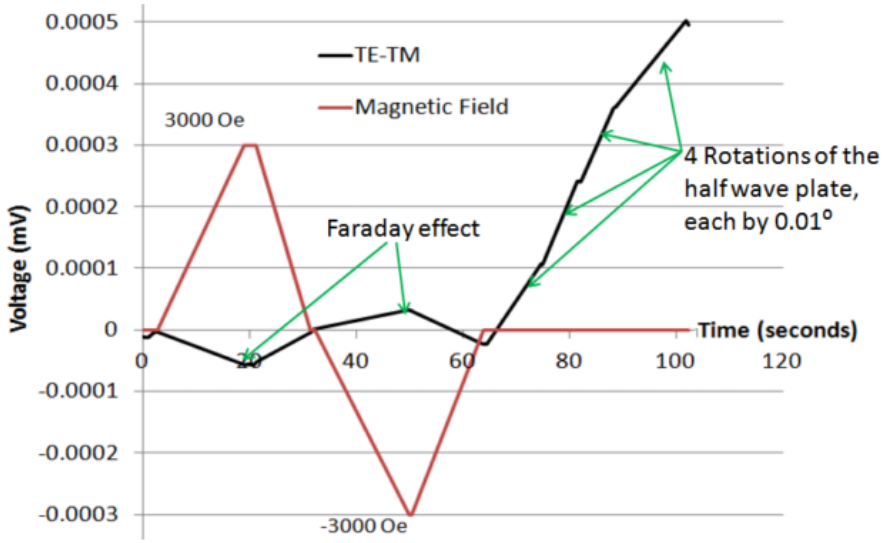

Figure 2-10: Example showing the typical raw data obtained from the detectors.

$$\theta_F = \frac{\left(\frac{a}{b}\right) c * 2}{t}$$

Equation 2.3: Relation for calculation Faraday rotation from the Faraday rotation measurement setup.

In the data shown in Figure 2-10, a ≈ 0.0000445 mV, b ≈ 0.000134 mV, c = 0.01°, t = 240nm. These parameters lead to the Faraday rotation value of -277°/cm. The negative sign represents the left-handed rotation of the polarization which can be observed from the counterclockwise rotation of polarization that is determined by performing a prior calibration using a control sample.

2.8 Vibrating Sample Magnetometry (VSM)

VSM is an instrument that measures the magnetic properties of materials by generating magnetic hysteresis loops. The idea behind this technique is that when a magnetized sample is vibrated in the periphery of a coil, the flux in the coil changes. A schematic of the instrument is shown in Figure 2-11.

During a measurement, the sample is attached to the tip of a vibrating rod that is placed between two electromagnets. Depending upon the type of measurement, the sample can be placed perpendicular or parallel to the direction of the applied field. An induced emf is created in the pick-up coils by the oscillating sample. The magnitude of the induced emf is proportional to the magnetic moment of a sample. A range of magnetic

moments are obtained by sweeping the field from -5000 Oe to 5000 Oe for the garnet films studied in this work. Upon sweeping, a hysteresis loop is generated which gives information about important parameters like the coercivity, remnance and saturation magnetization of the films.

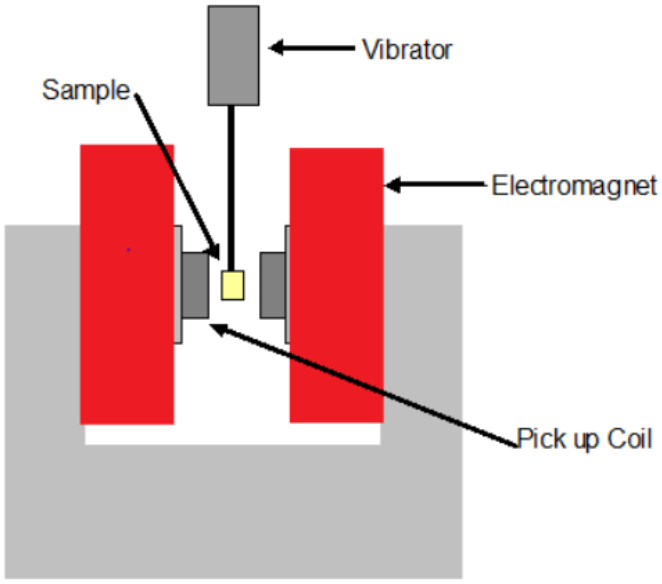

Figure 2-11: Schematic of the vibrating sample magnetometer (VSM).

2.9 Profilometery

The thickness of the films was measured using University of Minnesota Nano center's KLA-Tencor P-16 and P-7 surface profilometers. Prior to deposition, small portion of the substrate is masked using a polymer. This masked off area is lifted-off post-deposition with the help of sonication in acetone.

The profilometer consists of a sample holder with a vacuum chuck that is used to hold the samples in place while a stylus tip scans across a specified distance of the sample at

a specified force, generating a profile data. The step height and hence the thickness of the samples can be determined by post-processing of the data using the software provided by KLA tencor. Typically, vertical features from 10nm to 3mm can be measured using the P-7 and the P-16.

2.10 Spectroscopic ellipsometry

Refractive index (n) and extinction coefficients (k) of the garnet films were determined using University of Minnesota Characterization facility's J.A. Wollam VASE spectroscopic Ellipsometer which has a spectral range of 250-1100nm.

The polarization state of light can be decomposed into TE and TM components that can be denoted by E_{TE} and $E_{TM.}$ Polarization is defined using the phase delay between the TE and TM components. 0 °refers to a linearly polarized state, whereas 90° refers to circular polarization. Anything between 0 ° to 90 ° phase delay means the light has an ellipticity. When a light wave with a certain ellipticity is incident upon the sample, the interaction with the sample surface causes a change in ellipticity. This difference in ellipticity between the incident beam versus the reflected beam is measured by the ellipsometer. This difference can be used to determine the optical properties of the sample material. Mathematically, the phenomenon is denoted by the term reflection coefficient (ρ) that is given by the relation in Equation 2.4. This ratio can be decomposed into two components; the change in amplitude (ψ) and phase shift (Δ) of the incident wave [41]. Experimental values of ψ and Δ, generated by different ρ are fitted onto theoretical models to determine the optical constants (n, k) of the material.

$$\rho = \frac{E_{TE\,(reflected)}/E_{TE\,(incident)}}{E_{TM\,(reflected)}/E_{TM\,(incident)}} = \tan\psi e^{i\Delta}$$

Equation 2.4: Reflection coefficient of a thin film in ellipsometry measurement [41].

2.11 Reflectance/Transmittance measurements

The reflectance and transmittance measurements of garnet films on various transparent and non-transparent substrates were carried out on the Perkin Elmer Lambda 950 UV-VIS spectrometer. The detailed configuration of the system can be found in page 25 of the Perkin Elmer Lambda 650/850/950 hardware guide [50]. The equipment has a spectral range of 250-2500nm and a resolution of up to 0.01 nm.

The light sources are deuterium and tungsten halogen lamps. Using a combination of mirrors, the light is focused into a double monochromator to select the wavelength that is incident on the sample. For transmission measurements, the beam then passes through the sample into a transmission compartment for analysis. For reflection measurements, the beam passes through the sample compartment into the reflection compartment where it is reflected off the sample into an analysis monochromator. The spectrometer's software plots the spectrum obtained from the sample as reflection/transmission vs. wavelength, while subtracting a background that is simultaneously obtained from a reference sample.

2.12 Device Simulations

2.12.1 Simulations of SOI waveguides using modesolver methods

As discussed briefly in section 1.1.9, ultra-thin layers of YIG, called seedlayers are used for the growth of Ce:YIG and Bi:YIG for SOI (silicon on insulator) waveguide isolators. In this semiconductor-core device, the waveguide has a higher index of refraction (n ≈ 3) than the garnet layer (n ≈ 2). A schematic of mode propagation in this device is shown in Figure 2-12. As light propagates through the waveguide, the evanescent tail extends through the seedlayer before reaching the Ce:YIG layer, where the nonreciprocal interaction takes place. A software package called WGMODES©, written as MATLAB scripts by the University of Maryland was used for the simulation of seedlayers [51].

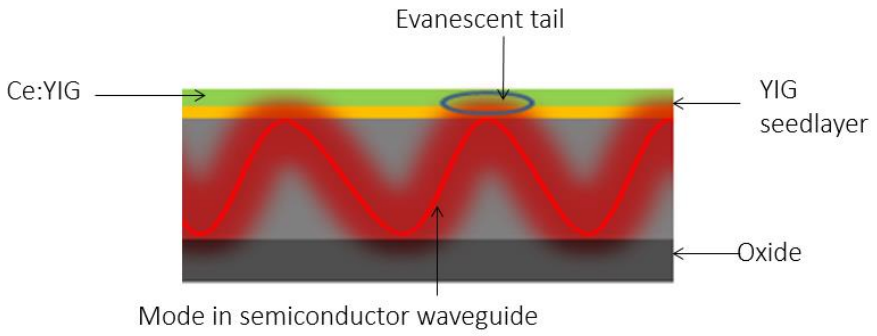

Figure 2-12: Schematic of mode propagation in an SOI waveguide with garnet cladding.

The polarization state of electromagnetic waves can be described using a set of values called the Stokes parameters (S_1, S_2, S_3) which can be visualized using the Poincare sphere shown in Figure 2-13. In this sphere, the equator represents all orientations of linearly polarized light and the north and the south poles represent right and left circular

polarizations, respectively. All other points in on the sphere represent elliptically polarized states where the ellipticity rises with the distance from the equator [52]–[54].

S_1 describes the preponderance of the horizontal linear polarization intensity over the vertical linear polarization intensity. S_2 describes the preponderance of the +45 ° linear polarization intensity over the -45 ° linear polarization intensity. S_3 parameter describes the preponderance of the RCP (right circularly polarized) intensity over the left circular polarization (LCP) intensity. Hence, S_3 parameter describes the degree of nonreciprocal polarization mode conversion and is directly related to ε_{xz} of the dielectric tensor shown in Equation 1.2. Larger S_3 parameters indicate larger the magneto-optical effects and hence devices with smaller footprint. For this work, the S_3 Stokes parameter for the TE-like polarized mode was calculated by finite-difference modesolver, a typical representation of the parameters is shown in Figure 2-14.

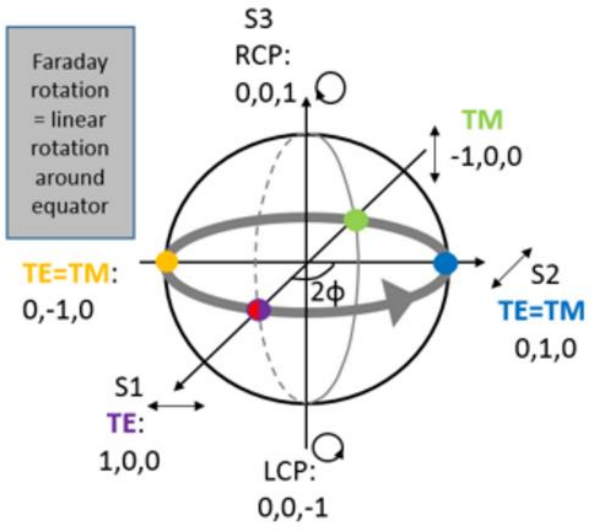

Figure 2-13: The Poincare sphere used for the visualization of the polarization in terms of Stokes S_1, S_2 and S_3 parameters. Adapted from Cui Zhang's Ph.D. thesis [54].

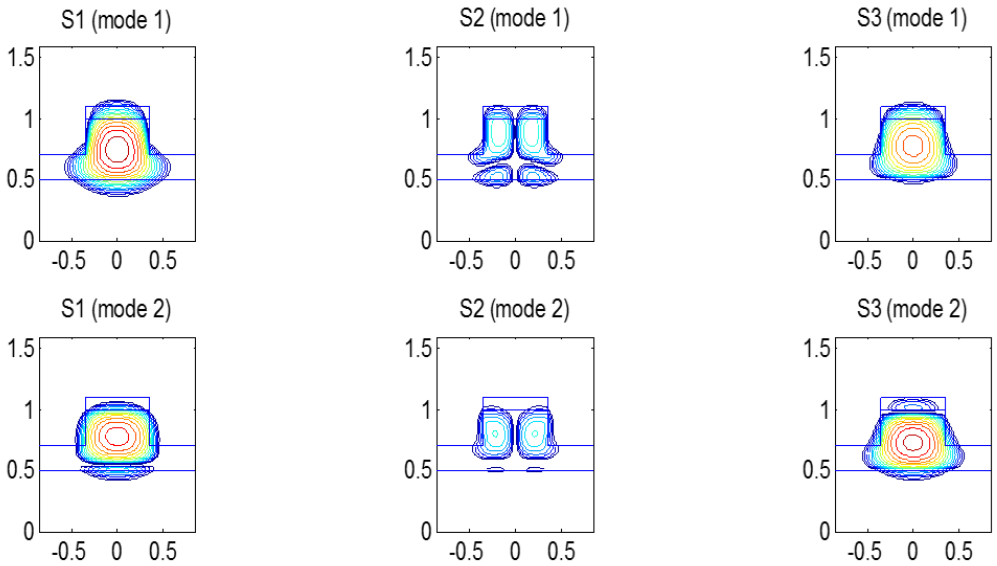

Figure 2-14: Stokes parameters; S_1, S_2, S_3 for top: TE-like modes and bottom: TM-like modes for a device whose detailed dimensions are given in Figure 3-3.

2.12.2 Finite-difference time-domain (FDTD) simulations

Waveguide devices of different anisotropic properties, shape and sizes were simulated using the FDTD software package from Lumerical solutions.

FDTD is a numerical analysis method that solves Maxwell's equations at several points in a 3-D simulation region. As the name suggests, FDTD is a time-domain method. However, the frequency analysis of the electromagnetic signals can be carried out by the software by employing Fourier transform. The main attraction of the FDTD package is that its algorithm allows for very accurate simulation of the propagation of electromagnetic waves in waveguides requiring low processing power and shorter times.

To describe the simulation setup, an example of YIG is used. The refractive index of YIG (n) =2.1 and the Faraday rotation (θ_F) at 1550nm is typically 200 °/cm. From Equation 1.2 and Equation 1.3, the permittivity tensor for YIG with these specific values of n and θ_F is calculated to be:

$$\varepsilon = \begin{bmatrix} 4.41 & 0 & 0.00036167i \\ 0 & 4.41 & 0 \\ -0.00036167i & 0 & 4.41 \end{bmatrix}$$

Equation 2.5: Permittivity tensor for YIG

FDTD doesn't allow for the direct entry of permittivity tensors, it only takes the eigenvalues and eigenvectors of a matrix. Hence the tensor must be diagonalized first. This is done by the help of a unitary rotation matrix (U) such that ($UU^T=U^TU=1$) and is given by:

$$U = \begin{bmatrix} \frac{1}{\sqrt{2}} & 0 & \frac{1}{\sqrt{2}}i \\ 0 & 1 & 0 \\ \frac{1}{\sqrt{2}} & 0 & -\frac{1}{\sqrt{2}}i \end{bmatrix}$$

Equation 2.6: Rotation matrix

The complex conjugate transpose of U is given by:

$$U^\dagger = \begin{bmatrix} \frac{1}{\sqrt{2}} & 0 & \frac{1}{\sqrt{2}} \\ 0 & 1 & 0 \\ -\frac{1}{\sqrt{2}}i & 0 & \frac{1}{\sqrt{2}}i \end{bmatrix}$$

Equation 2.7: Complex conjugate of the rotation matrix

Now, the matrix (ε) can be diagonalized using the following, where ε_D gives the eigenvalues of the diagonalized matrix.

$$\varepsilon_D = U\varepsilon U^{\dagger}$$

Equation 2.8: Relation used to diagonalize the permittivity tensor.

Upon diagonalization, ε_D will have the following values for this specific YIG:

$$\varepsilon_D = \begin{bmatrix} 4.4104 & 0 & 0 \\ 0 & 4.4100 & 0 \\ 0 & 0 & 4.4096 \end{bmatrix}$$

Equation 2.9: Eigenvalues of the permittivity tensor of YIG

However, these values correspond to the squares of refractive index (n^2), and hence the square root needs to be taken to obtain diagonal n_{xx}, n_{yy} and n_{zz} terms which results in the following:

$$\sqrt{\varepsilon_D} = \begin{bmatrix} 2.1001 & 0 & 0 \\ 0 & 2.1000 & 0 \\ 0 & 0 & 2.0999 \end{bmatrix}$$

Equation 2.10: n_{xx},n_{yy},n_{zz} values for YIG

These are the values that are entered in the FDTD software to define the anisotropic material.

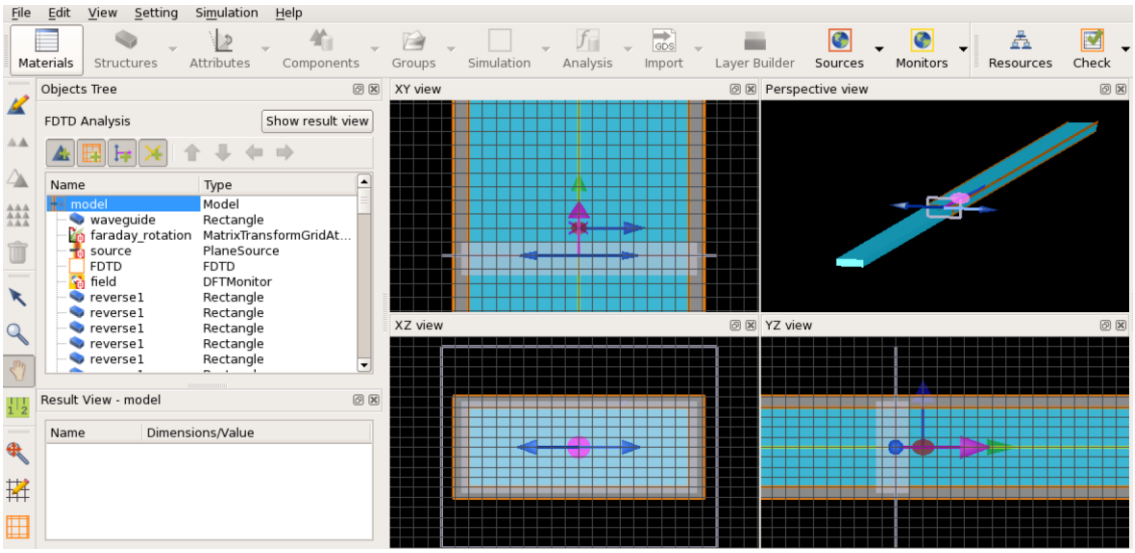

Figure 2-15: Screenshot of a typical garnet waveguide simulation setup in Lumerical FDTD solutions.

After defining the waveguide using these values, a plane wave light source is added to the simulation setup to propagate light along the length of the waveguide. Most of the simulations presented here are carried out in the telcon wavelength (1550nm). Perfectly matched layer (PML) boundaries are setup to avoid stray reflections. An electromagnetic field monitor is added along the center of the waveguide. The change in the electric and magnetic field as light propagates through the waveguide is recorded. In this way, garnet waveguide devices are simulated and their performance is analyzed. More details for specific device designs are discussed in section 3.10. A typical simulation setup in the FDTD software with different views is shown in Figure 2-15.

2.13 Waveguide fabrication

Waveguides were developed using the process of photolithography. A schematic of the process is given in Figure 2-16.

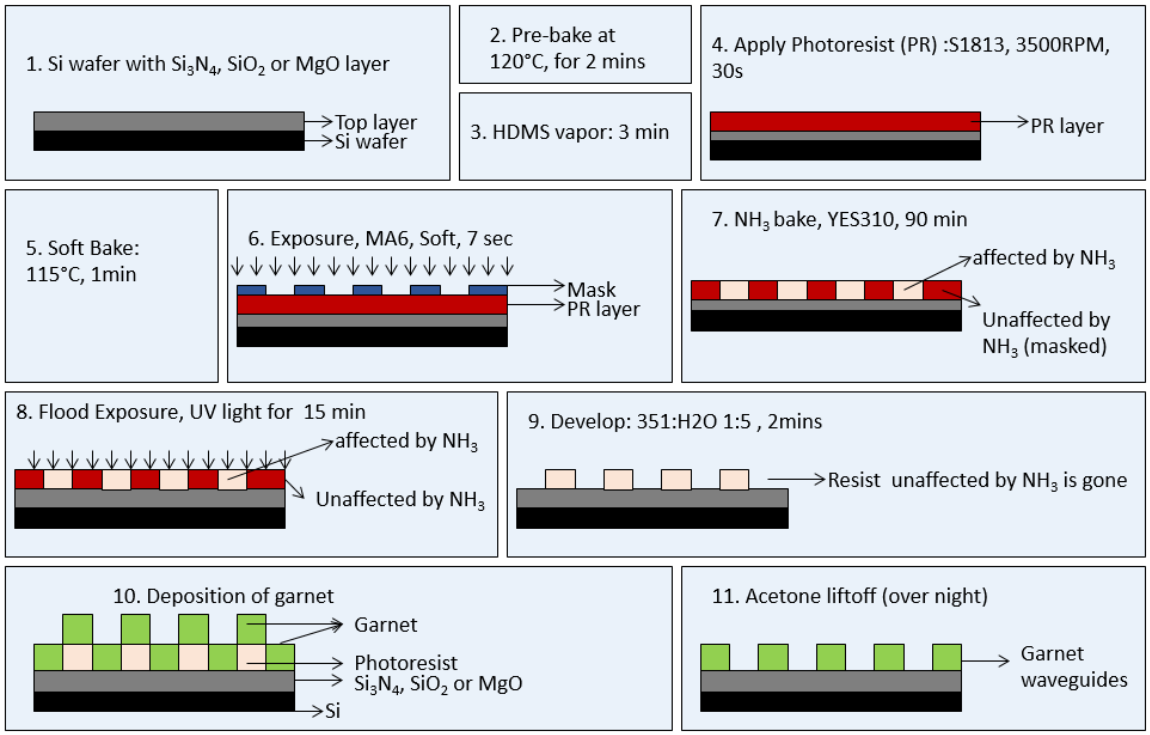

Figure 2-16: Garnet waveguide fabrication by the procedure of photolithography.

First, the substrates were pre-baked on a hot plate at 120 °C for 2 minutes. Following this, they were introduced into the HMDS (hexamethyldisilizane) vapor for 3 minutes. HMDS promotes the adhesion of the photoresist to the substrates by forming a thin hydrophobic layer. After this, the photoresist (S1813) was spun coated for 30 seconds at 3500 RPM. This produced a 1.3 mm layer on top of the substrates. To improve photoresist adhesion and to avoid mask contamination. The coated substrates were then soft baked at 115 °C for a minute before exposure.

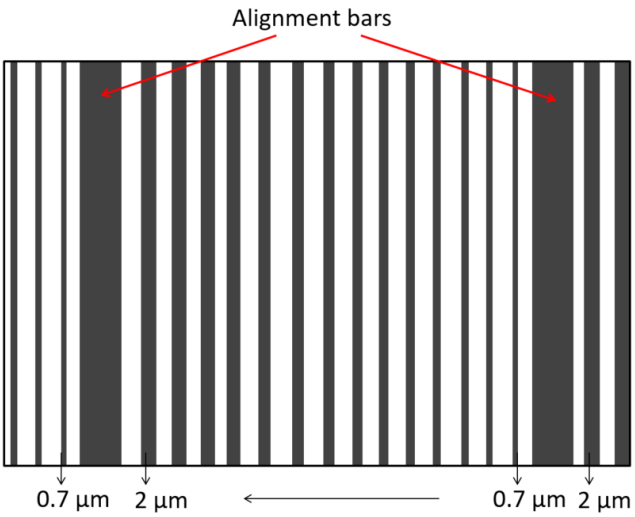

Figure 2-17: Schematic of the mask used for the fabrication of garnet waveguides. The numbers in the bottom represent the width of the features. White: Glass, black: patterns defined with chrome. Note: Figure not to scale.

The exposure was carried out on the KarlSuss MA6 contact aligner for 7 seconds using soft contact between the mask and the sample. A schematic of the mask used in the process is shown in Figure 2-17. The samples were then baked for 90 minutes in the YES310 image reversal NH_3 oven to allow for the NH_3 gas to react with the exposed resist making it insoluble in the developer. Next, UV light flood exposure was carried out on the samples for 15 minutes. During the flood exposure, the UV light reacts with the previously unexposed areas making them easily removable during the development process. Development was carried out by immersing the samples in a 351:H_2O 1:5 developer for 2 minutes. During this process, the resist that was unexposed during the first exposure was removed. Next, the garnet film was sputtered onto the substrates by RF sputtering with argon plasma in an oxygen reactive environment. This was followed

by an overnight acetone liftoff, which removed all the remaining photoresist along with the garnet deposited on top of the unwanted resist. After this, the samples were annealed at 900 °C for 2 minutes in an oxygen environment to allow the garnet waveguides to crystallize.

3 Integration of garnet isolators with semiconductors

3.1 Background and motivation

The work towards integrating garnet materials on semiconductor platforms to develop integrated optical isolators started in the early 1990s. A conceptual picture of such device is shown in Figure 3-1.

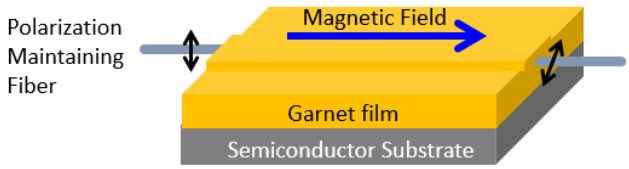

Figure 3-1: Conceptual schematic of an early semiconductor-integrated waveguide isolator.

Garnet and semiconductor materials have very different lattice parameters (e.g. YIG= 12.37 Å and Si= 5.43 Å) [16] and thermal expansion coefficients. Hence, growing YIG on Si was a challenging endeavor for a long time. Several approaches have been taken to achieve this integration goal, majority of which involved GGG (gadolinium gallium garnet) substrates. Razeghi *et. al*. grew various III-V quantum wells directly onto GGG [55]. Mizumoto *et. al*. took a different approach by using an InGaAs layer to lattice match to GGG followed by growing InP [56]. Note that these involved GGG substrates, but no garnet films. Yokoi *et. al*. came up with a hybrid integration technique in 1995 where garnet film grown on GGG was wafer bonded onto Si [57]. Stadler *et. al*. grew garnet films on InP and GaAs substrates using MgO buffer layers [58]. Stadler *et. al*. later came up with a method that reliably produced phase pure YIG on non-garnet substrates

by rapid thermal annealing (RTA) sputtered films in a fully oxidizing environment [43]. However, the mismatch in thermal expansion coefficients (e.g. YIG= 10.4 ppm/ ^{o}C, Si= 2.33 ppm/ ^{o}C) [16] often leads to stress and cracking in the films that lead to large optical losses. This problem was tackled by patterning the YIG into waveguides on Si before annealing [44], which significantly reduced the cracking of the films and hence the optical losses.

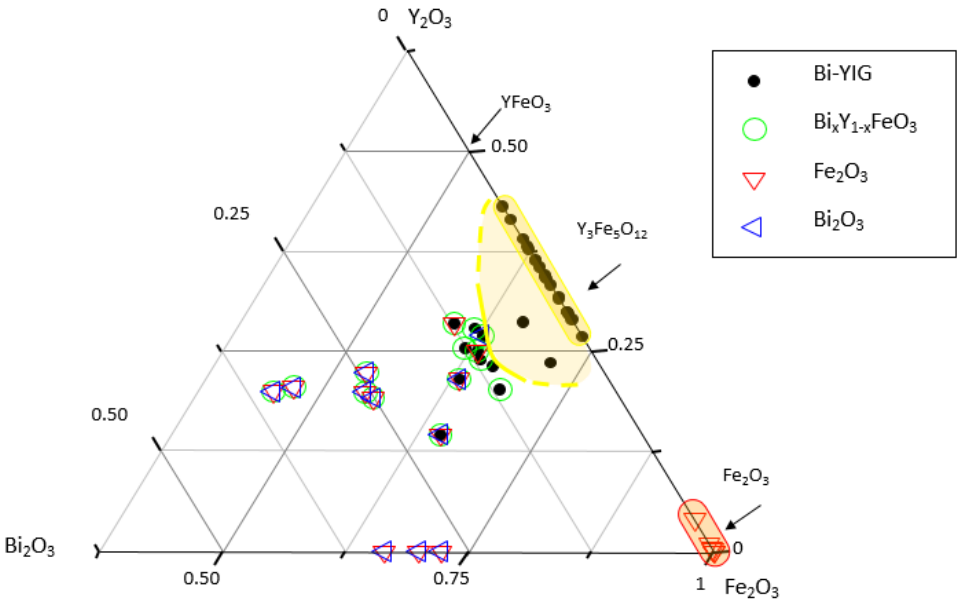

Figure 3-2: Ternary phase diagram of Bi:YIG. Adapted from Sang-Yeob Sung's Ph.D. thesis [16].

As discussed in section 1.1.7, Bi:YIG and Ce:YIG have significantly larger coefficients of Faraday rotation compared to YIG. Hence, to reduce device footprints, these substituted garnets would be preferred. However, as shown by the ternary phase diagram in Figure 3-2, there is a very little window for the formation of garnet (highlighted yellow region). Any attempt to grow Bi:YIG (or Ce:YIG) on non-garnet substrates leads to the formation

of other unwanted oxide phases that lead to optical losses and usually no Faraday rotation [16]. The solution to this problem came in 2011 from Bi *et. al*. [59] who discovered that phase pure Ce:YIG and Bi:YIG phases could be achieved (without other unwanted phases) by a two-step deposition process in which an ultra-thin (20nm minimum) pure YIG 'seedlayer' was first deposited on a semiconductor substrate by the method of Stadler *et. al*. [43] before depositing thicker layers of Ce:YIG or Bi: YIG. Later, Gomi *et. al*. realized that Ce:YIG has a significantly larger coefficient of Faraday rotation than YIG and Bi:YIG [60]. This paved the way for work in reduction in device footprint.

From a commercial point of view, a monolithically integrated optical isolator is highly desirable because of its ease in processing and cost-efficiency. This was first shown by Bi *et. al*. [64] in 2011 using a Ce:YIG cladded SOI (silicon on insulator) racetrack resonator. This device comprised of a 290µm Si ring resonator with a sputtered Ce:YIG cladding on a YIG seedlayer, and is the shortest reported isolator device to date. Almost all the recent devices (both FR and NRPS based) have employed Ce:YIG as the magneto-optical material. Some examples are: a 4mm long Si interferometer with wafer-bonded Ce:YIG [61], a 1.8mm (diameter) Si ring with wafer-bonded Ce:YIG [62], and a 920µm long Si interferometer with adhesive-bonded Ce:YIG [63].

3.2 Implications of using YIG seedlayers in garnet clad waveguide isolators

To study the effects of YIG seedlayers in waveguide isolators, Light propagation (TE-like mode) was simulated in SOI waveguides with 100nm claddings of Ce:YIG grown on YIG seedlayers (0-100nm) with a saturating magnetic field parallel to the light propagation. A cross section schematic of the device is shown in Figure 3-3.

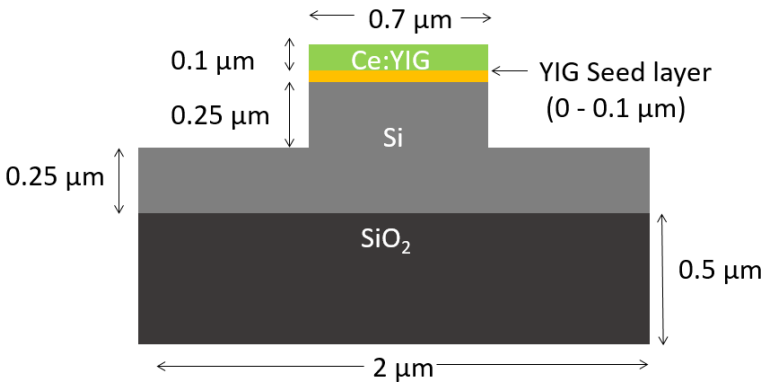

Figure 3-3: Cross-sectional schematic of an SOI waveguide with garnet (Ce:YIG/YIG) cladding.

Reported Faraday rotation coefficients were used, including 200°/cm [20] for the YIG seedlayer and a range of values (-1100°/cm [65], -1263°/cm [64], -3300 °/cm [66], -3700°/cm [21], -4500°/cm [23]) for the Ce:YIG layer. The lower values in this range are attributed to incomplete crystallization of Ce:YIG [64]. The results are shown in Figure 3-4 plotted against varying thicknesses of the YIG seedlayer. This allows for a direct comparison to be drawn between various configurations of Ce:YIG and seed (YIG) layers. The description of the technical details of the simulations and definition of Stokes parameters (y-axis) is given in 2.12.1.

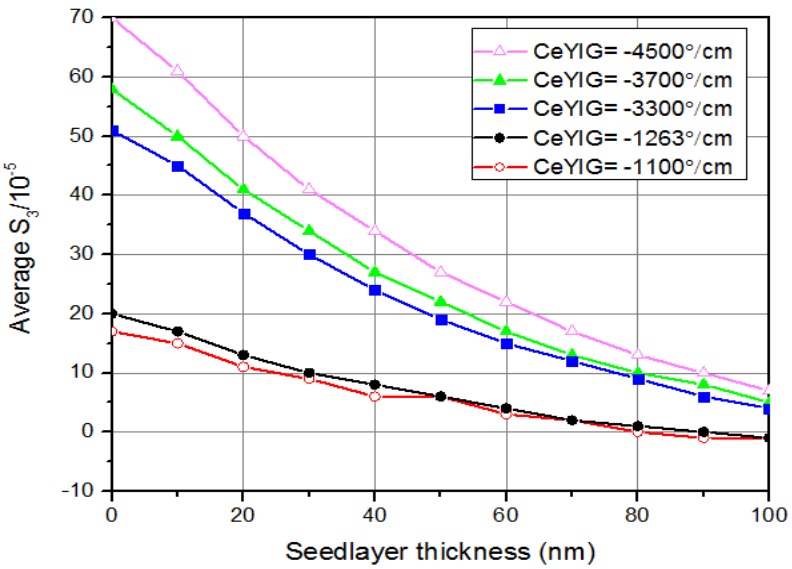

Figure 3-4: Average S_3 Stokes parameters for TE-like modes in SOI waveguides with Ce:YIG/YIG claddings plotted vs thickness of YIG seedlayer (Device schematic in Figure 3-3). The claddings use 0–100 nm YIG seedlayer (200°/cm) and a fixed thickness (100 nm) Ce:YIG layer (varying Faraday rotation).

Previous work by Block *et al.* has shown that a YIG seedlayer must be at least 45nm thick for complete crystallization of a doped cladding [21]. However, the results shown in Figure 3-4 suggest that even a 20nm-thin seedlayer, as used in Ref. [64], reduces the net magneto-optic (MO) effect of the garnet-cladded SOI waveguides by almost 30% (as seen in all the curves by comparing 0 vs. 20nm seedlayer thickness). If a 45nm YIG seedlayer would allow complete crystallization of an ideal Ce:YIG cladding, thereby obtaining Faraday rotation as high as -4500 °/cm, 45nm would still separate the guided mode from the active cladding. Therefore, the S_3 parameter would be reduced by 57% (S_3 = 70 vs. 30 x10^{-5}) as shown by the pink curve ($t_{seedlayer}$ = 0 vs. 45nm) in Figure 3-4. The net MO effect is comparable to a cladding with only -2000 °/cm and no seedlayer, which has not been achieved to date. In fact, these simulations show that the best Ce:YIG

cladding material to date is the -3700°/cm Ce:YIG that required a 45nm YIG seedlayer [21]. Figure 3-4 shows that this cladding will lead to almost twice the S_3 parameter, which means twice the effective MO mode conversion per unit length than the next highest reported value for bottom-seeded Ce:YIG (on Si), -1263°/cm [64] (S_3 = 25 vs. 13 x10^{-5}). This can be seen from the green ($t_{seedlayer}$ = 45nm) and black ($t_{seedlayer}$ = 20nm) curves.

In addition to reducing the MO effect, the seedlayer also adds processing steps. In most reports, the seedlayer is annealed outside of the processing vacuum before the Ce:YIG cladding can be deposited. As mentioned in the introduction, however, a one-step YIG/Ce:YIG anneal was recently introduced that works even when the undoped YIG seed is on top of the cladding (and therefore not between the cladding and the guide). Unfortunately, the Faraday rotation of that Ce:YIG was only -1100°/cm [65], so it is 36% less effective than the -3700°/cm Ce:YIG (45nm seedlayer) that was determined to be the best cladding above (S_3 = 25 vs. 16 x10^{-5}). This can be seen in Figure 3-4 from the green ($t_{seedlayer}$ = 45nm) and red ($t_{seedlayer}$ = 0nm) curves.

A final concern with YIG seedlayers is that they have Faraday rotations of opposite chirality to that of Ce:YIG. The dramatic results in Figure 3-4 indicate that the YIG layers are not simply optical dead space; they are detrimental to the Ce:YIG performance. These factors stress the importance of finding magneto-optical garnets on semiconductor waveguides that either (1) do not require seedlayers, or (2) have seedlayers with the same chirality as Ce:YIG claddings.

3.3 Exploration of novel garnets

The exploration of garnets that don't require seedlayers or that have the same chirality as Ce:YIG claddings began by analyzing of the crystal structure of the garnet shown in Figure 1-3. In the unit cell of an iron garnet, the rare earth (RE) ions have the largest ionic radii and they reside on the dodecahedral sites. Fe^{3+} ions have smaller radii and they occupy the octahedral and tetrahedral sites. These cations are surrounded by the O^{2-} polyhedra, which are the only anions present in the iron garnets. Table 3-1 shows the ratio of radii between the cations present at the three different sites to that of the O^{2-} anions for some naturally occurring, synthetic and potential garnets that were used to explore the possibilities for making new garnets with the help of the information from naturally occurring and synthetic garnets.

As seen from Table 3-1, the ratio of radii of the cation in the dodecahedral site to that of the O^{2-} anion is under 0.76 for all the listed naturally occurring as well as the synthetic garnets. This information was utilized to determine which RE ions can be used to develop new garnets.

The maximum reported Faraday rotation of Ce:YIG at 1550 nm is -4500 °/cm [23]. This Ce:YIG was grown by substituting 33% of the Y^{3+} ions of the YIG lattice by the Ce^{3+} ions. S.N 6. of Table 3-1 shows that this composition has a dodecahedral cation to anion radii ratio of 0.756. However, as seen in S.N 15. of the table, the ratio in the case of pure cerium iron garnet would be 0.816, which is a plausible reason behind why pure cerium iron garnet cannot be made.

Naturally occurring garnets										
S.N	Garnet	Dodecahedral	radii (Å)	Cation /anion	Octahedral	radii (Å)	Cation/anion	Tetrahedral	radii (Å)	Cation/anion
1	$Mg_3Al_2Si_3O_{12}$	Mg^{2+}	0.89	0.636	Al^{3+}	0.539	0.385	Si^{4+}	0.26	0.186
2	$Mn_3Al_2Si_3O_{12}$	Mn^{2+}	0.96	0.686	Al^{3+}	0.539	0.385	Si^{4+}	0.26	0.186
Available synthetic garnets										
3	$Y_3Fe_5O_{12}$	Y^{3+}	1.016	0.726	Fe^{3+}	0.642	0.459	Fe^{3+}	0.642	0.459
4	$Gd_3Ga_5O_{12}$	Gd^{3+}	1.061	0.758	Ga^{3+}	0.61	0.436	Ga3+	0.47	0.336
5	$Bi_1Y_2Fe_5O_{12}$	Bi^{3+}/Y^{3+}	1.055	0.754	Fe^{3+}	0.642	0.459	Fe^{3+}	0.642	0.459
6	$Ce_1Y_2Fe_5O_{12}$	Ce^{3+}/Y^{3+}	1.058	0.756	Fe^{3+}	0.642	0.459	Fe^{3+}	0.642	0.459
Exploration of new garnets										
7	$Tb_3Fe_5O_{12}$	Tb^{3+}	1.044	0.746	Fe^{3+}	0.642	0.459	Fe^{3+}	0.642	0.459
8	$In_3Fe_5O_{12}$	In^{3+}	0.94	0.671	Fe^{3+}	0.642	0.459	Fe^{3+}	0.642	0.459
9	$Yb_3Fe_5O_{12}$	Yb^{3+}	0.982	0.701	Fe^{3+}	0.642	0.459	Fe^{3+}	0.642	0.459
10	$Eu_3Fe_5O_{13}$	Eu^{3+}	1.073	0.766	Fe^{3+}	0.642	0.459	Fe^{3+}	0.642	0.459
11	$Sm_3Fe_5O_{13}$	Sm^{3+}	1.087	0.776	Fe^{3+}	0.642	0.459	Fe^{3+}	0.642	0.459
12	$Nd_3Fe_5O_{14}$	Nd^{3+}	1.12	0.8	Fe^{3+}	0.642	0.459	Fe^{3+}	0.642	0.459
13	$Bi_3Fe_5O_{12}$	Bi^{3+}	1.132	0.809	Fe^{3+}	0.642	0.459	Fe^{3+}	0.642	0.459
14	$Pr_3Fe_5O_{13}$	Pr^{3+}	1.137	0.812	Fe^{3+}	0.642	0.459	Fe^{3+}	0.642	0.459
15	$Ce_3Fe_5O_{12}$	Ce^{3+}	1.143	0.816	Fe^{3+}	0.642	0.459	Fe^{3+}	0.642	0.459
16	$La_3Fe_5O_{13}$	La^{3+}	1.19	0.85	Fe^{3+}	0.642	0.459	Fe^{3+}	0.642	0.459

Table 3-1: Ratio of radii of cations present the three different sites to that of O^{2-} anion for some naturally occurring, synthetic and hypothetical garnets. The radius of O^{2-} is 1.40 Å. Ionic radii data obtained from Refs: [67]–[69].

3.4 Terbium iron garnets

3.4.1 Film growth

Based on the discussion in section 3.3, terbium iron garnet ($Tb_3Fe_5O_{12}$/TIG) (S.N 7. of Table 3-1) has a cation (Tb^{3+}) to O^{2-} radii ratio of 0.746. This potential garnet was explored by growing films by RF sputtering of Fe and Tb targets at different powers and O_2/Ar partial pressures. Films were post annealed (RTA) at 900 °C for 2 minutes in an O_2 atmosphere. The variation in deposition parameters and corresponding phases obtained en route to the development of TIG are given in Table 3-2. $TbFeO_3$ (terbium ferrite/terbium iron (iii) oxide) was the most commonly observed undesired phase.

Fe sputter power (W)	Tb sputter power (W)	Ar flow (SCCM)	O_2 flow (SCCM)	Resulting phase (XRD)
220	120	20.4	4	$TbFeO_3$
220	120	20.4	3	$TbFeO_3$+garnet
240	120	20.4	3	$TbFeO_3$
220	140	20.4	2	$TbFeO_3$ +garnet
230	110	20.4	2	$TbFeO_3$ +garnet
150	106	20.4	2	$TbFeO_3$ +garnet
210	120	20.4	2	$TbFeO_3$
200	120	20.4	2	TbO_2
220	100	20.4	2	$TbFeO_3$
220	120	20.4	2	Garnet
240	120	20.4	0	$TbFeO_3$

Table 3-2: Sputtering parameters corresponding to the phases determined by XRD.

3.4.2 Crystallinity and compositional analysis

All the films were characterized by XRD for phase information and by EDS for compositional analysis. Figure 3-5 shows the XRD data of the unique phases and their respective stoichiometry. The garnet forming composition was slightly lower than the 3:5 ratio of Tb:Fe of stoichiometric $Tb_3Fe_5O_{12}$ garnet. All the ratios above 3:5 (Tb:Fe) led to the formation of other phases that do not exhibit magneto-optical properties.

After the garnet-forming sputtering conditions were determined, the possibility of different substrates was explored. TIG was successfully grown on quartz, Si and MgO substrates as shown by the XRD results in Figure 3-6. This opened the possibility of using TIG for garnet-core device in addition to SOI devices because all three of these substrates have lower indices of refraction than TIG.

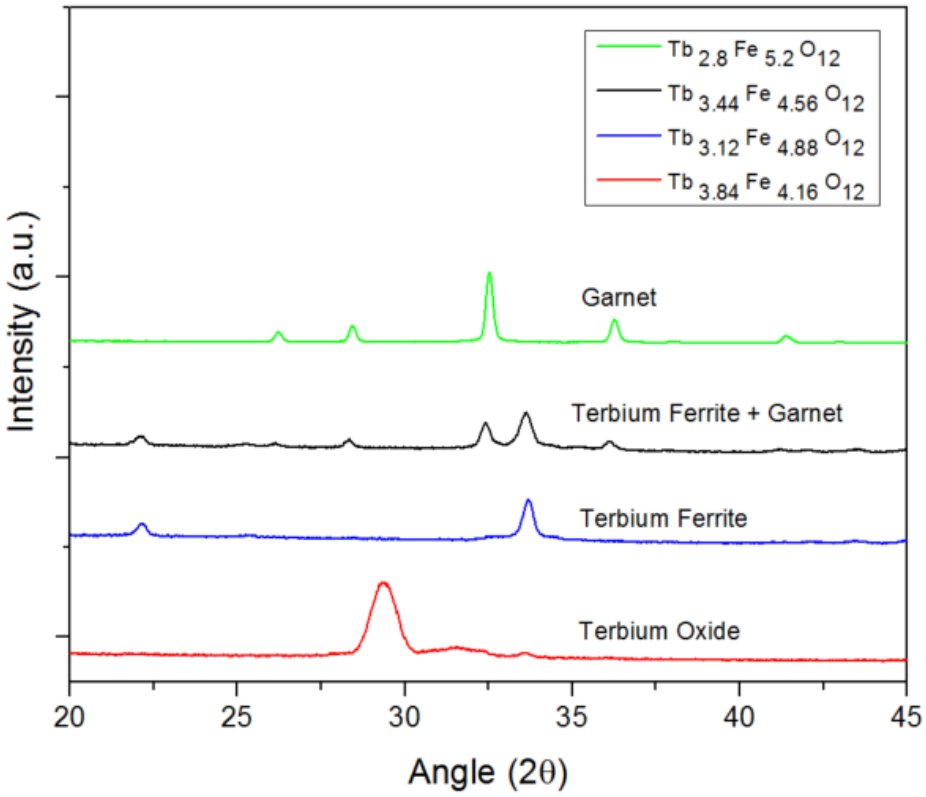

Figure 3-5: Crystallinity (XRD) and corresponding compositional (EDS) analysis of the different phases obtained *en* route to the development of terbium iron garnet.

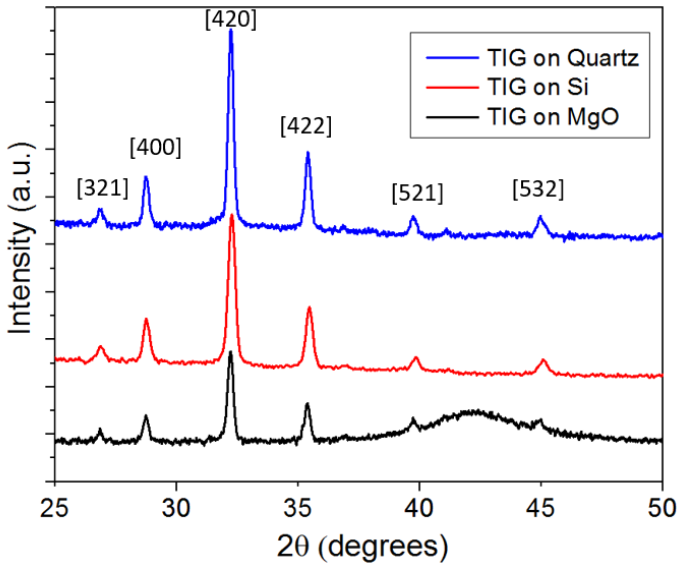

Figure 3-6: XRD of TIG films grown on different substrates.

3.4.3 Magnetic characterization

Magnetic characterization of the TIG films was done using VSM. In-plane and normal-to-plane hysteresis loops were measured by sweeping the field from -5000 to 5000 Oe. The films reached saturation magnetization at ~3500 Oe and had a coercivity of 250 Oe in both configurations (Figure 3-7). These films were 380nm thick.

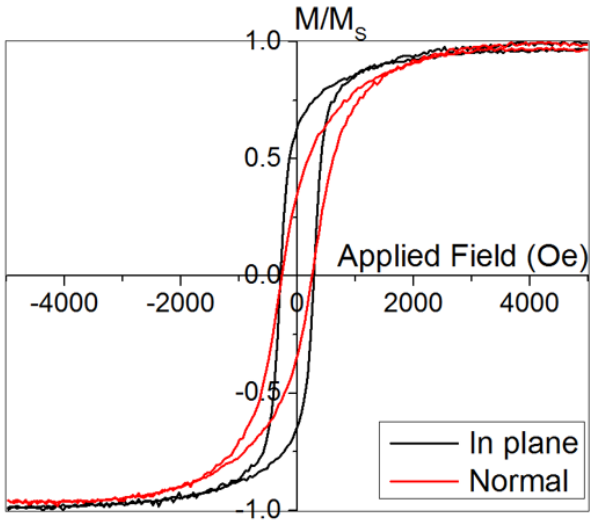

Figure 3-7: Magnetic hysteresis loop of TIG measured using a VSM.

3.4.4 Faraday rotation

Faraday rotation measurements were performed using the setup discussed in section 2.7. A 1550nm laser was used and a field of >2000 Oe was generated using custom made electromagnets. Prior to measuring the TIG films, a control sample (commercially available garnet made by liquid phase epitaxy) which has a negative chirality of Faraday rotation was measured. The raw data obtained from this measurement is shown in Figure 3-8. Following this, the Faraday rotation of the 380nm thick TIG films on double-side-polished Si substrates were measured. An identical measurement with just the bare

Si was done (and later subtracted) prior to measuring the garnet films to rule out the effect of the substrate. The raw data obtained after the subtraction is shown in Figure 3-9.

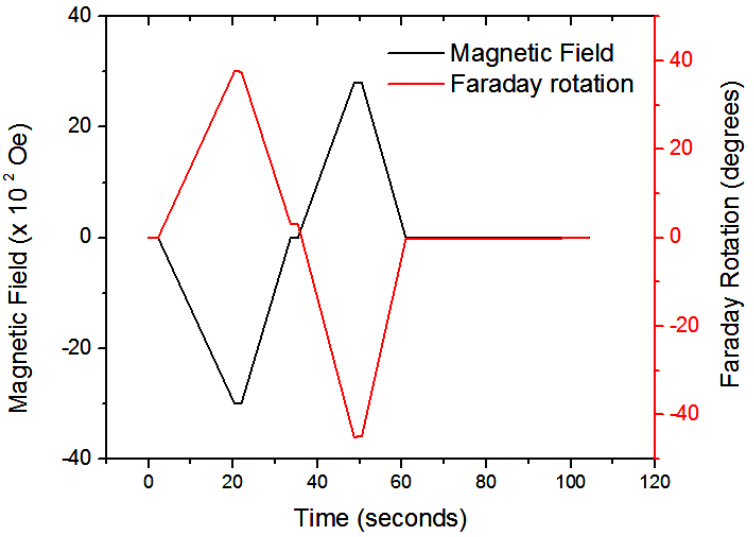

Figure 3-8: Raw Faraday rotation data of a commercially available garnet with negative Faraday rotation.

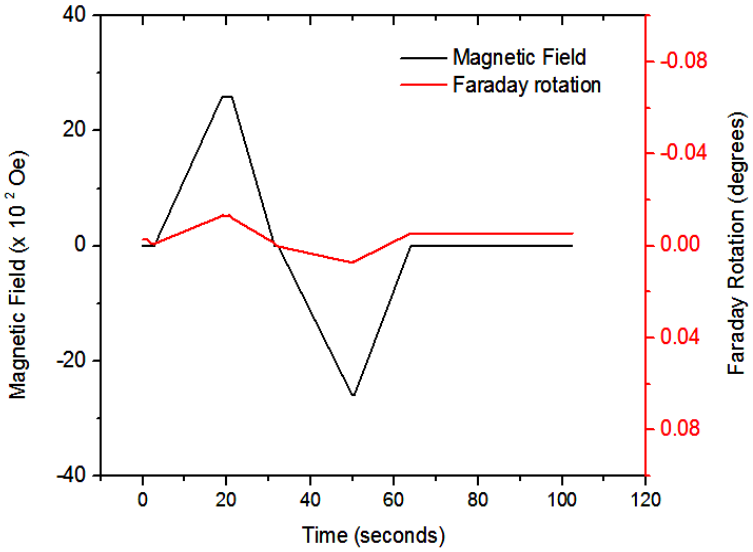

Figure 3-9: Raw Faraday rotation data of a 380nm thick TIG film on double side polished Si substrate.

Post processing of the raw data from Figure 3-9, done by the procedure discussed in section 2.7, resulted in a Faraday rotation value of $\theta_{F(TIG)}$= 500 °/cm. The Faraday rotation data for TIG (Figure 3-9) is opposite in chirality compared to the raw data for the commercially available garnet (Figure 3-8) which has a (known) negative Faraday rotation. Hence it was established that TIG has a positive chirality of Faraday rotation, similar to undoped YIG.

3.4.5 Film morphology

To have a high figure of merit, low optical loss is equally as important as high Faraday rotation. A thick garnet layer is ideal for waveguide applications, but it is hard to obtain without the cracking of films. TIG films of varying thicknesses were grown on Si substrates as observed by the optical micrographs in Figure 3-10.

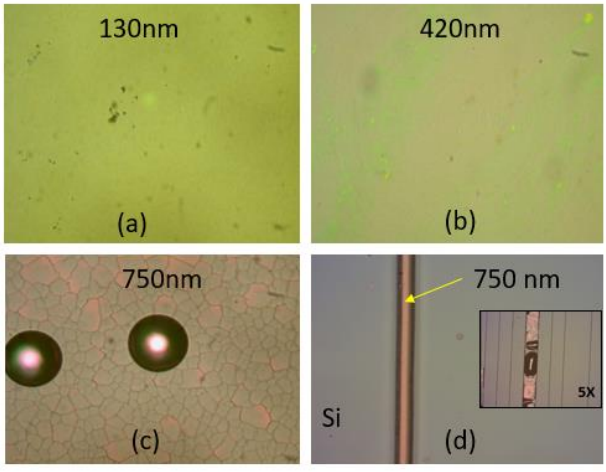

Figure 3-10: Optical micrographs (100 x) of different thicknesses of TIG on Si substrates. (a,b,c): Deposited without patterning. (d) Patterned before deposition. Note that the wide (100um) alignment bar in (d) cracked, but the thin waveguides (0.7-2um) did not.

There was no sign of cracks in the 130 nm and 420 nm TIG films. However, significant amount of cracking was observed in a 750 nm TIG film which can be seen from Figure 3-10 (c). This problem was overcomed by patterning the films using photolithography prior to deposition followed by acetone lift-off before annealing. Figure 3-10 (d) is an optical micrograph of a patterned TIG film of the same thickness as shown in (c), but without any cracks. The patterning procedure is discussed in detail in section 2.13.

Another study of film morphology was carried out by annealing the samples of identical thickness at different temperatures. TIG films on Si substrate annealed at 700°C for 5 mins in oxygen did not crystallize as shown by the SEM image in Figure 3-11 (a). Films annealed 800°C for 2 minutes partially crystallized (b) and films annealed at 800°C for 2 minutes seem to be almost fully crystalline as seen from (c).

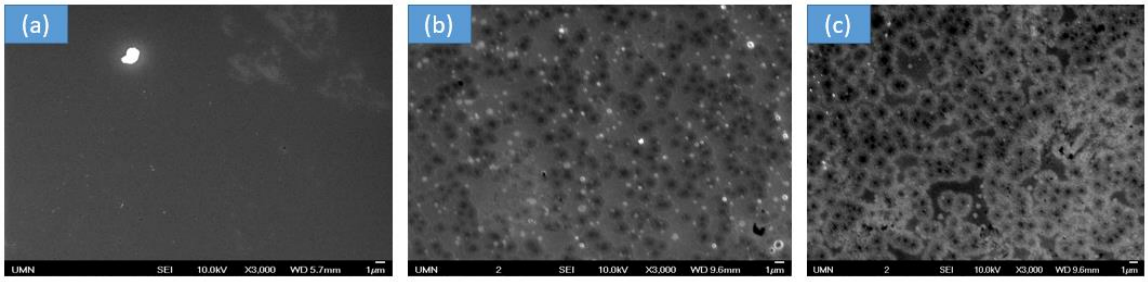

Figure 3-11: SEM image of TIG films on Si substrate annealed (RTA) at (a) 700°C for 5 mins (b) 800°C for 2 mins and (c) 900°C for 2 mins in O_2.

3.5 TIG waveguide fabrication

TIG waveguides (720 nm thick) were fabricated on Si_3N_4, SiO_2 and MgO substrates following the procedure discussed in section 2.13. The thickness and indices of the substrates are given in Table 3-3. The results are shown in the optical micrographs in Figure 3-12.

Substrate	Thickness (µm)	Refractive index (n)
Si_3N_4 on Si	0.9	1.91
SiO_2 (thermal oxide) on Si	1	1.46
MgO sputtered on double polished Si	0.45	1.76

Table 3-3: Different substrates used in the fabrication of TIG waveguides with their corresponding thicknesses and refractive indices.

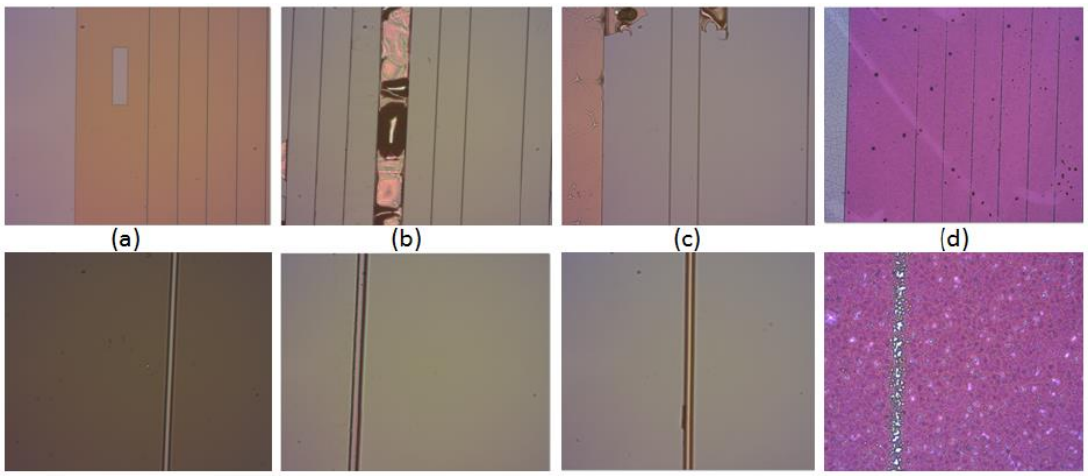

Figure 3-12: Top: 5x and bottom: 50x magnified optical micrographs of 720 nm thick TIG waveguides fabricated by the procedure discussed in section 2.13. (a) Samples prior to annealing. (b) TIG on Si_3N_4 on Si after annealing (c) TIG on SiO_2 on Si after annealing (d) TIG on MgO on Si after annealing. Note that the wide (100um) alignment bar in (b and c) cracked, but the thin waveguides (0.7-2um) did not.

Figure 3-12 (a) shows how the samples looked before annealing. Figures (b-d) are the optical micrographs of the annealed TIG waveguides on Si_3N_4, SiO_2 and MgO substrates respectively. In the case of Si_3N_4 (b) and SiO_2 (c), the waveguides run across the

substrates without showing any signs of breakage or cracking. This ensures that the light can travel through the waveguides with minimal optical loss. However, in the case of MgO (d), the waveguides seemed to have significant amount of cracking and breaking. This was caused by the hygroscopic nature of MgO, which absorbed water during the process of lift-off. This problem can be avoided by first developing the ridges, followed by MgO and TIG deposition respectively. This way, the MgO wouldn't be exposed to wet etching.

3.6 Bismuth doped terbium iron garnets (Bi:TIG)

3.6.1 Combinatorial garnet growth

After the successful development of TIG films, possibilities of doping TIG was explored. A study of combinatorial Bi:TIG films was done by sputtering individual Tb, Fe and Bi targets. Substrates were placed at different sites on the chamber's stage as shown by the diagram in Figure 3-13 where the numbers represent the ratio of (Bi+Tb) to Fe determined by EDS analysis of films at different sites. Based on this analysis, the garnet forming regions (ratio of 0.6) was estimated and is represented by the yellow regions.

The variation observed in Figure 3-13 is due to the different deposition rates of the individual targets. This initial study was helpful moving forward as the garnets developed for this project involved co-sputtering with multiple targets. It highlighted the fact that there might be a significant difference in the composition of the sample depending upon where in the sputtering chamber it is placed.

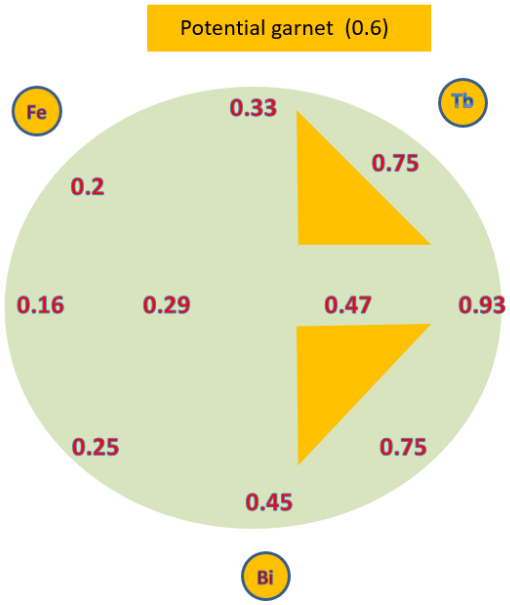

Figure 3-13: Samples placed at different sites of the stage along with their respective (Bi+Tb/Fe) ratios. Yellow regions denote the potential garnet forming areas.

3.6.2 Sputtering parameters, resulting composition and phases

In Bi:TIG, the Bi ions substitute the Tb ions on the dodecahedral sites of the TIG lattice. Sputtering parameters were adjusted to achieve the highest substitution of Bi in $Bi_XTb_{3-X}Fe_5O_{12}$ deposited on Si substrates.

Table 3-4 shows the variation in sputtering parameters and resulting phases. The XRD results of the different phases obtained *en* route to the development of Bi:TIG along with their corresponding elemental compositions is shown in Figure 3-14. It is interesting to note that two different phases (S.N 3 and 4) were obtained by the same sputter power and gas pressures. The difference was in the deposition time (and consequently the film thickness). S.N. 3 was deposited for 20 mins and resulted in

197nm film of mixed (garnet and bismuth ferrite) phases whereas S.N. 4 was deposited for 10 mins and resulted in a 115nm film of phase pure garnet. As seen from Figure 3-14, the mixed phase has a lot more Bi than the phase pure garnet which suggests that the sputtering of Bi:TIG is non-linear that causes a significant increase in the Bi content of the films with longer sputtering times, consequently leading to the formation of bismuth ferrite along with the garnet.

S.N	Bi sputter power (W)	Fe sputter power (W)	Tb sputter power (W)	Ar flow (SCCM)	O_2 flow (SCCM)	Resulting phase (XRD)
1	15	220	110	20.4	2.0	Bismuth iron oxide
2	15	210	100	20.4	2.0	Bismuth iron oxide+terbium ferrite
3	10	220	110	20.4	2.0	Bismuth ferrite +garnet
4	10	220	110	20.4	2.0	Garnet

Table 3-4: Deposition parameters and resulting phases for Bi:TIG. XRD results of corresponding phases are shown in Figure 3-14.

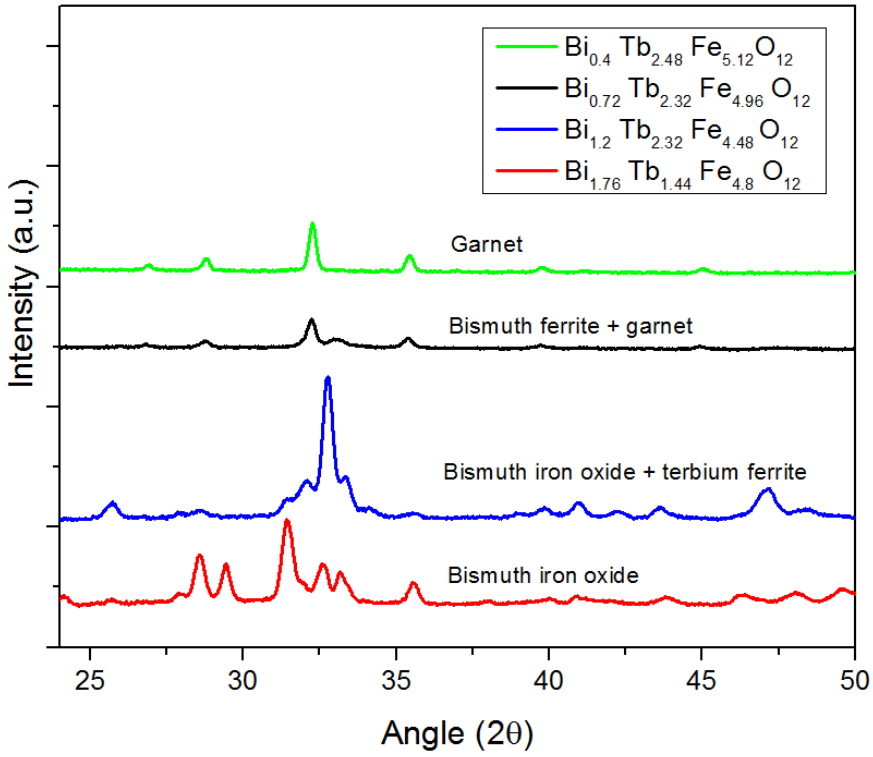

Figure 3-14: Crystallinity (XRD) and corresponding compositional (EDS) analysis of the different phases obtained en route to the development of the bismuth doped terbium iron garnet phase. All films were deposited on Si substrates.

After determining the garnet forming sputtering parameters with highest possible Bi substitution, Bi:TIG was deposited on different substrates. Single phase garnet films were obtained on quartz and Si substrates whose XRD results are shown in Figure 3-15.

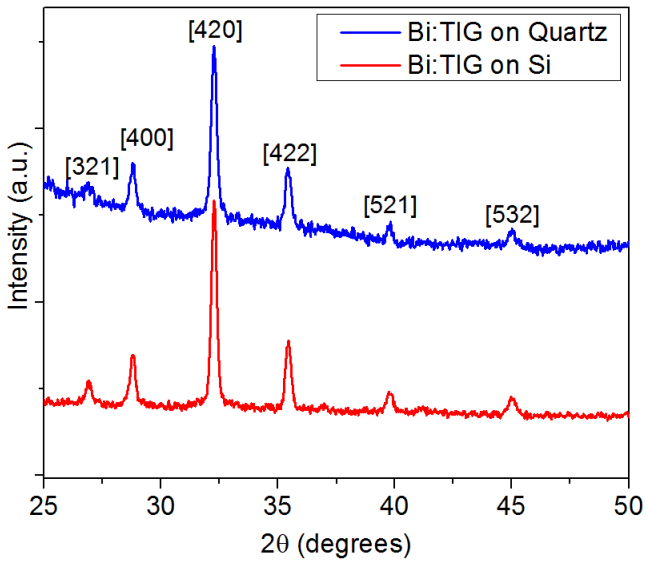

Figure 3-15: XRD of Bi:TIG on quartz and Si substrates.

3.6.3 Film Morphology

Like the TIG films, Bi:TIG films on Si substrate annealed (RTA) at 700°C for 5 mins in oxygen did not crystallize as shown by the SEM image in Figure 3-16(a). Films annealed 800°C for 2 minutes partially crystallized (b) and films annealed at 900°C for 2 minutes seem to be almost fully crystalline as seen in (c). This shows that the crystallization parameters for Bi:TIG is similar to that of pure TIG despite the doping.

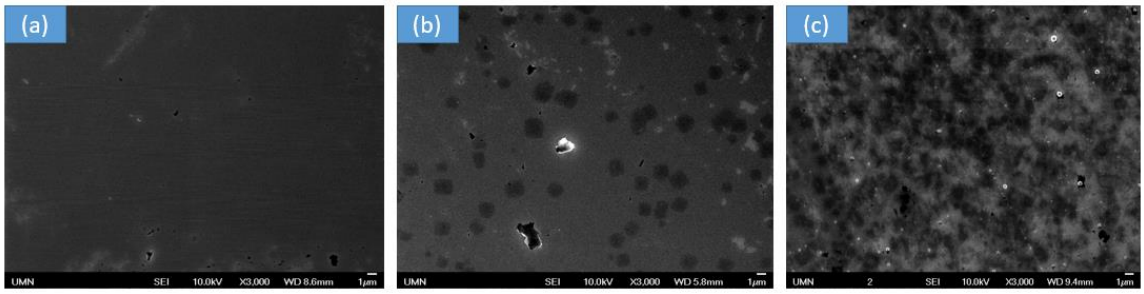

Figure 3-16: SEM images of Bi:TIG films annealed at (a) (a) 700°C for 5 mins (b) 800°C for 2 mins and (c) 900°C for 2 mins in O_2.

3.6.4 Magnetic characterization

In-plane and normal-to-plane magnetic hysteresis loops of Bi:TIG films were measured using VSM (Figure 3-17), sweeping the applied field from -5000 to 5000 Oe.

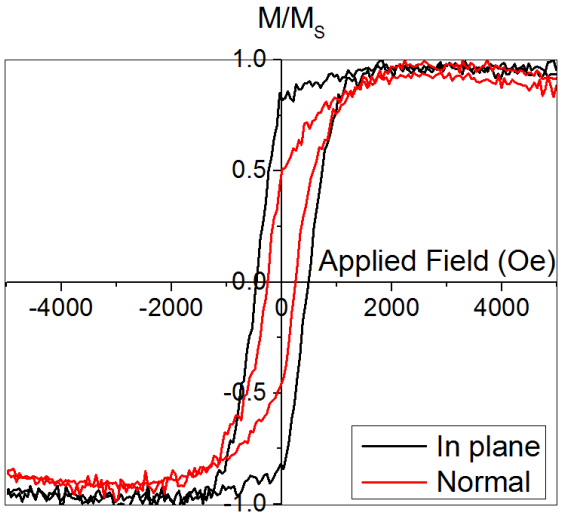

Figure 3-17: In-plane and normal-to-plane magnetic hysteresis loops of Bi:TIG films.

The coercivity for the in-plane configuration and normal-to-plane was 475 Oe and 250 Oe respectively. Saturation field for both configurations was about 2500 Oe. These films were 240nm thick.

3.6.5 Faraday rotation measurement

Faraday rotation measurements were performed at 1550nm, switching the magnetic field from -3000 to 3000 Oe. The raw measurement data is shown in Figure 3-18. A value of -500 deg/cm was obtained after performing the analysis procedure discussed in section 2.7. The chirality of Faraday rotation was determined after a comparison with the values obtained for a commercially available bulk garnet which is shown in Figure 3-8.

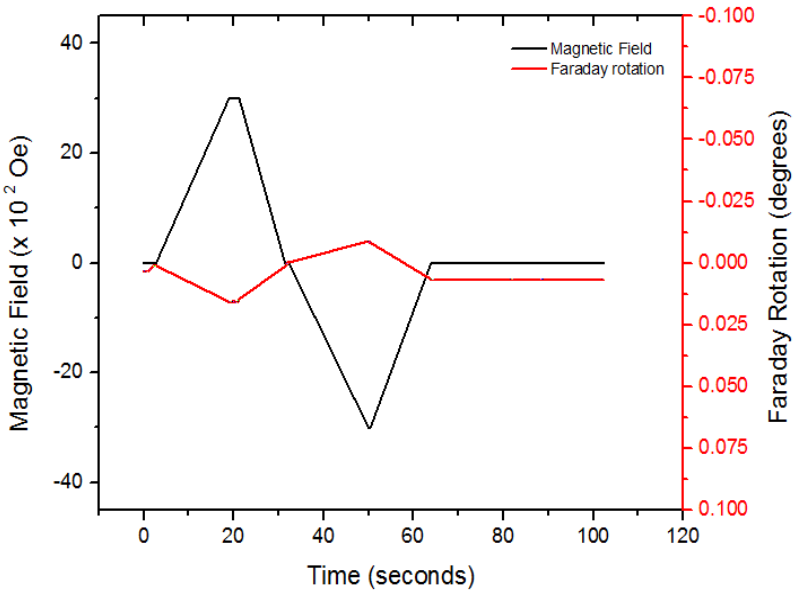

Figure 3-18: Raw Faraday rotation measurement data of Bi:TIG.

3.7 Cerium doped terbium iron garnets (Ce:TIG)

Ce:TIG was successfully grown on Si and quartz substrates whose XRD results are shown in Figure 3-19. Films were obtained by sputtering individual Ce, Tb and Fe targets with reactive O_2 followed by RTA at 900 °C for 2 minutes in O_2 atmosphere.

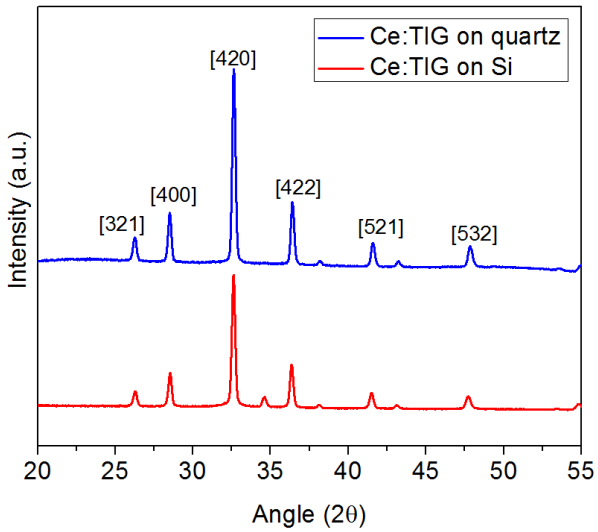

Figure 3-19: Ce:TIG on Si and quartz substrates.

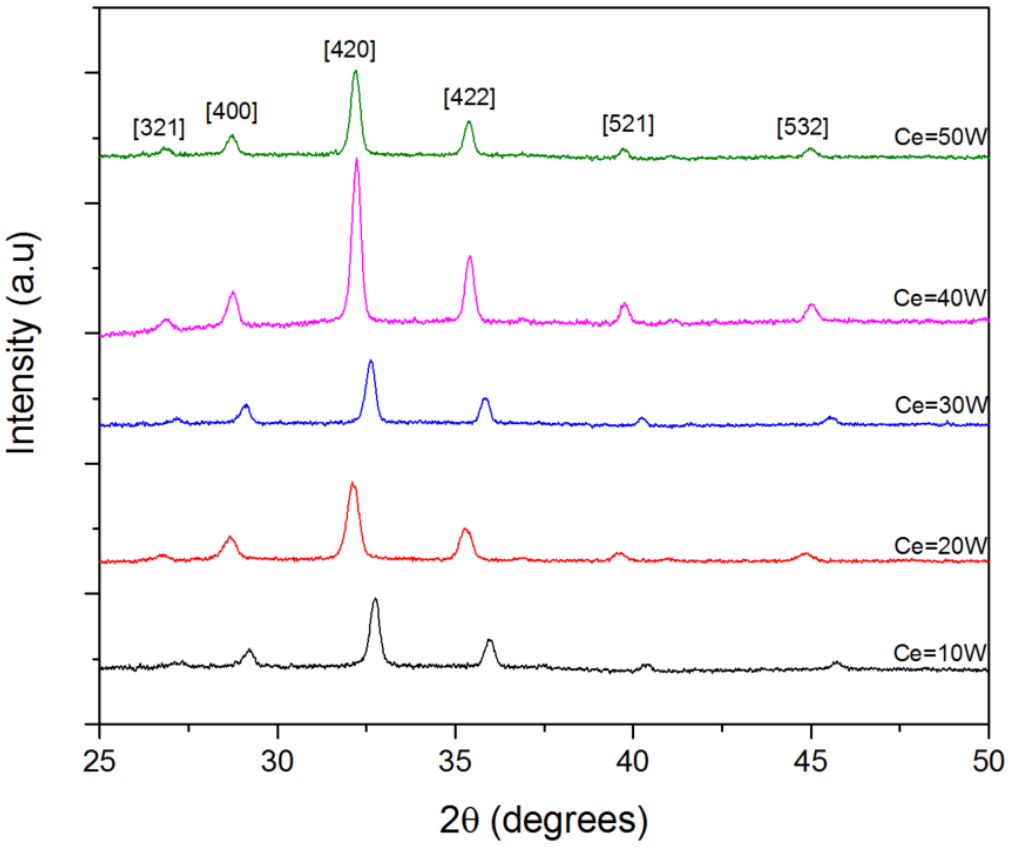

Figure 3-20: XRD of Ce:TIG sputtered at different Ce powers, keeping rest of the parameters the same. Ar=20.4 SCCMs, O_2=2.0 SCCMs, Fe=220W, Tb=110W.

Range of Ce substituted TIG films were explored by sputtering individual Fe, Tb and Ce targets. The sputtering power for Fe and Tb were kept the same (220 W and 110 W respectively). Sputtering Ce at a higher power of (60W) resulted in the formation of the CeO_2 phase shown in Figure 3-21.

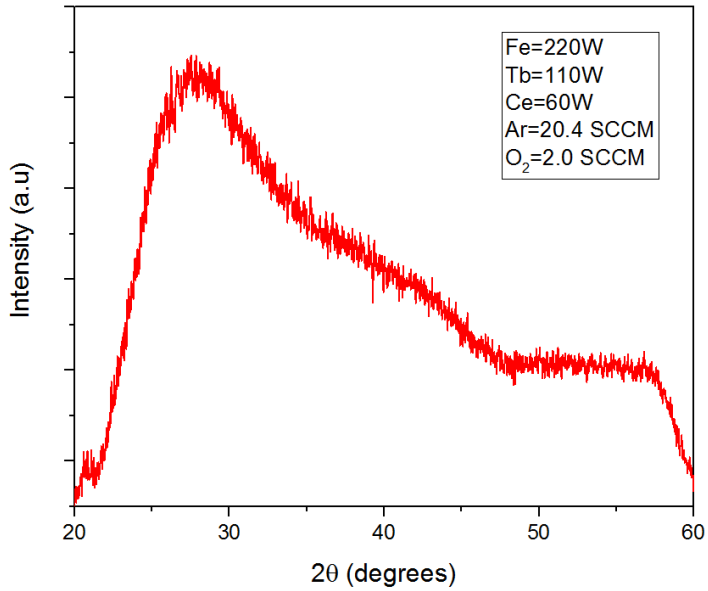

Figure 3-21: CeO_2 phase obtained with higher Ce sputtering power (60W).

Magnetic hysteresis loops were measured using a VSM sweeping the field from -5000 to 5000 Oe. The result for the sample sputtered at 40W Ce is shown in Figure 3-22.

Faraday rotation was measured at 1550nm using the measurement procedure discussed in section 2.7. Sputter power of Ce target vs Faraday rotation of the films is shown in Figure 3-23 which suggests that the film sputtered at 40W of Ce results in the highest Faraday rotation (-2600 °/cm) among the different compositions of Ce:TIG.

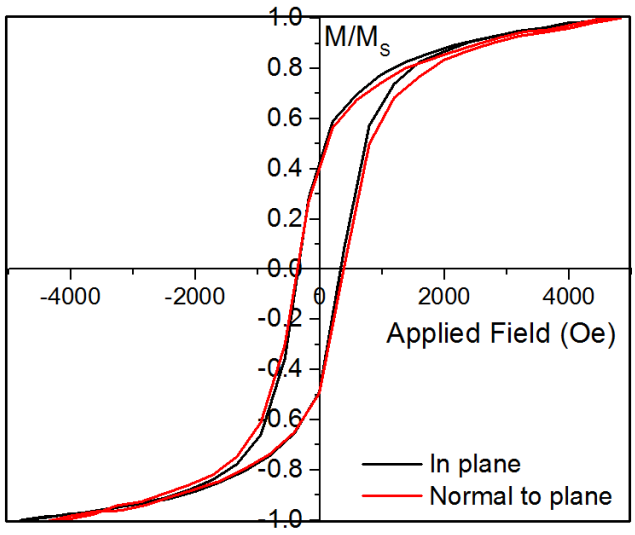

Figure 3-22: Hysteresis loop of Ce:TIG film on Si substrate measured using a VSM.

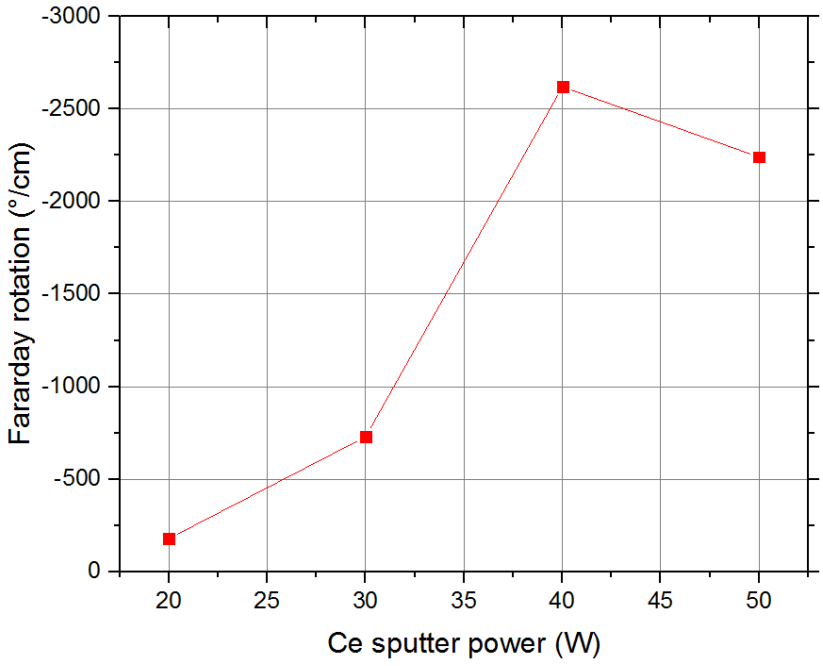

Figure 3-23: Ce:TIG Faraday rotation based on Ce sputtering power.

3.8 Waveguide isolators with doped terbium iron garnets

After the successful development of phase pure TIG, Bi:TIG and Ce:TIG films, the possibilities of waveguide isolator devices (schematic shown in Figure 3-24) using these new garnets were explored. First of all, the feasibility and efficiency of TIG and Bi:TIG as potential seedlayers for Ce:YIG (instead of YIG) was explored as these new garnets have higher Faraday rotation than YIG. Following this, a direct comparison of Ce:YIG claddings was made with identical devices with Ce:TIG claddings.

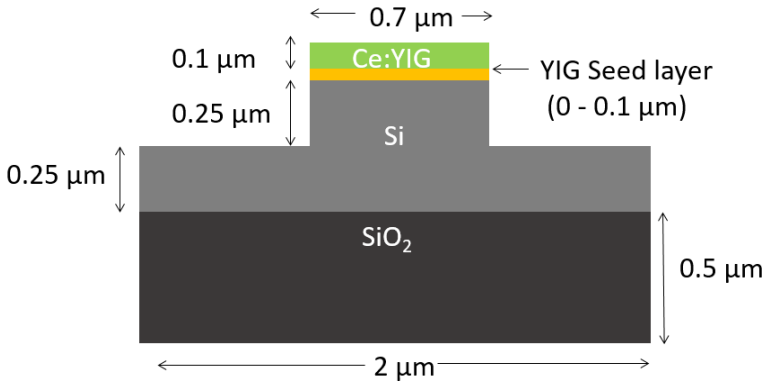

Figure 3-24: Schematic of SOI waveguide isolator with garnet cladding.

3.8.1 Comparisons of different seedlayers for Ce:YIG top cladding

Modesolver simulations were performed to compare the impact of various seedlayers on the net MO effect observed in SOI waveguides with Ce:YIG top claddings whose cross-sectional schematic is shown in Figure 3-24.

Figure 3-25 shows how the average Stokes (S_3) parameter varies with seedlayer thickness for Ce:YIG claddings with different reported values of Faraday rotation: -1263°/cm [64] , -3700°/cm [21] and -1100°/cm [65]**.** For the first two cases (-1263°/cm

and -3700°/cm Ce:YIG), the seedlayers (bottom) are between the guide and the Ce:YIG cladding whose thickness was kept constant at 100nm and the seedlayers were varied from 0-100 nm. For the third case (-1100°/cm Ce:YIG, green), the YIG seedlayer was not between the guide and the cladding but was rather on top of the Ce:YIG [11] . Here, the Ce:YIG thickness was varied from 100-200nm. For the fourth case, (-500 °/cm Bi:TIG, pink) there was no seedlayer required, but the Bi:TIG itself was varied from 100-200nm.

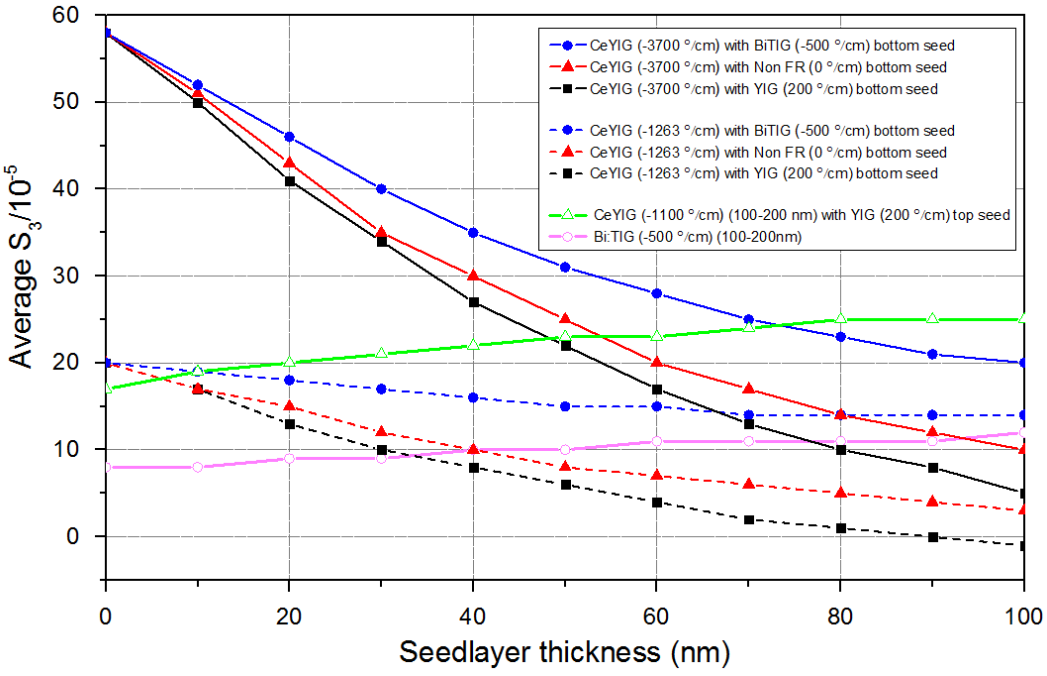

Figure 3-25: Seedlayer thickness plotted against average S_3 Stokes parameters for TE-like modes in SOI waveguides (schematic in Figure 3-3) with different combinations of garnet claddings. Devices with different reported values of Ce:YIG (-1100°/cm [65], -1263°/cm [64] and -3700°/cm [21]) grown on YIG (+) seedlayers are simulated and compared with devices that use non FR (0) seedlayers and Bi:TIG (-) seedlayers [70].

Figure 3-25 demonstrates that seedlayers with opposite chirality have detrimental impact on the net MO effect as seen by comparing seedlayers with +200 °/cm (YIG,

black curves), 0°/cm (eg: adhesion layers, red curves) and -500 °/cm (Bi:TIG, blue curves).

S.N.	Seed material	Seed thickness (nm)	Ce:YIG cladding θ_F (°/cm)	S_3 ($/10^{-5}$)	Corresponding curve in Figure 4	Reference.
i	Bi:TIG	45	-3700	33	blue, solid	Simulation
ii	YIG	45	-3700	25	black, solid	[21]
iii	YIG	top seed (30)	-1100	25	green	[65]
iv	Bi:TIG	20	-1263	18	blue, dotted	Simulation
v	YIG	20	-1263	13	black, dotted	[64]
vi	Bi:TIG	no seed	-500*	<12	pink	This work

Table 3-5: Summary of the specific YIG seedlayer thicknesses used in literature along with their corresponding simulated average S_3 Stokes parameters. Table demonstrates how the S_3 parameter significantly improves for the Ce:YIG grown on Bi:TIG seedlayer [70]. *Bi:TIG only.

Table 3-5 gives a summary of some of the Ce:YIG/YIG claddings simulated in Figure 3-25. The discovery of (iii) was extremely impressive. It used a single anneal and did not involve a layer between the waveguide and cladding. As seen from the green curve in Figure 3-25, if grown thick enough (>180nm), this cladding could have comparable MO effect as (ii). Here, the evanescent tail interacted directly with the Ce:YIG layer without having to pass through a bottom YIG seedlayer, and hence the S_3 parameter would get better with increasing thickness of Ce:YIG. The mode would be confined within the Ce:YIG and not reach the top YIG, and thus the opposite chirality of YIG wouldn't affect the mode conversion. However, the question is whether the Ce:YIG cladding can have high quality crystallinity at the interface with the guide when the seeding occurs from the top of this thick cladding. Even so, (iii) has more than twice the S_3 parameter and hence more than twice the MO impact on mode conversion than (vi). Therefore, Bi:TIG

will not be an effective seedless cladding unless minimal processing steps (i.e.: a single layer cladding with one anneal) are more desirable than a short device length. However, a Bi:TIG seedlayer improves modal interaction for (v) by 38% (S_3= 18 vs. 13/10^{-5}) and for (ii) by 32% (S_3= 33 vs. 25/10^{-5}). Therefore, (ii) has the maximum non-reciprocal effect among all of these reported Ce:YIG MO claddings, and Bi:TIG should be used as its seedlayer in future studies. These simulations highlight that seedlayer chirality is an important factor that has been overlooked in the literature to date.

Inspired by these results, the possibility of growing Ce:YIG film on Bi:TIG seedlayer (Si substrate) was explored and successfully achieved as shown by the XRD and EDS result in Figure 3-26. Here, the Bi:TIG seedlayer was grown by RF sputtering of Fe, Tb and Bi targets followed by 2 minutes annealing at 900 °C in an O_2 atmosphere using RTA. The Ce:YIG layer was grown by RF sputtering of a composite FeY target and a separate Ce target, also followed by 2 minutes annealing (RTA, 900 °C) in an O_2 atmosphere.

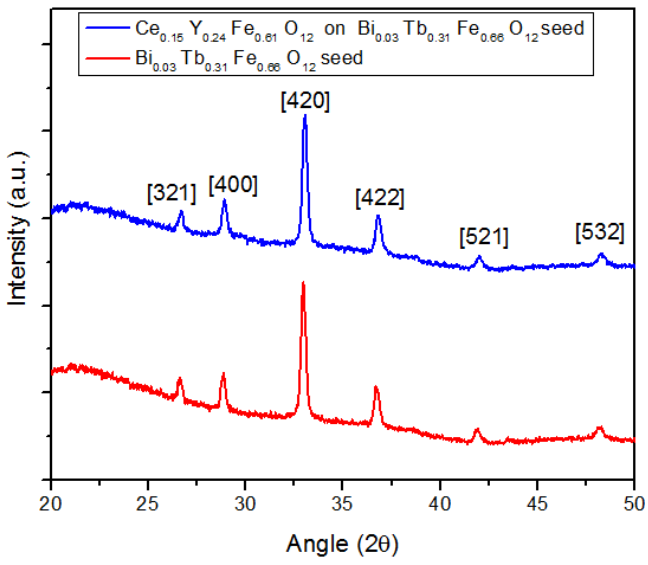

Figure 3-26: Crystallinity (XRD) and corresponding compositional (EDS) analysis of Bi:TIG seedlayer (red) and Ce:YIG top cladding (blue).

3.8.2 Simulation of SOI devices with Ce:TIG compared to Ce:YIG claddings

Light propagation (TE-like mode) was also simulated in SOI waveguides (schematic in Figure 3-24) with claddings of (i) Ce:TIG (100nm) (FR=-2600°/cm) and (ii) Ce:YIG (100-x nm) (FR= -3700°/cm) with YIG seed (x nm) (FR=200°/cm). A saturating magnetic field was kept parallel to the light propagation. The results are shown in Figure 3-27, where the seedlayer thickness is plotted against Stokes average S_3 parameter. The result shows that with increasing thickness of YIG seedlayer, there is a significant reduction in the S_3 parameter. Since Ce:TIG doesn't require a seedlayer, the S_3 parameter remains constant. The -3700 °/cm Ce:YIG used for this simulation is the highest reported Ce:YIG grown on Si substrate, which required a 45nm YIG seedlayer [21]. Figure 3-27 shows that the S_3 parameter in this case would be about $14/10^{-5}$ (red, t_{YIG}=45nm). A Ce:TIG (blue) of the same thickness would have an S_3 parameter of $40/10^{-5}$.

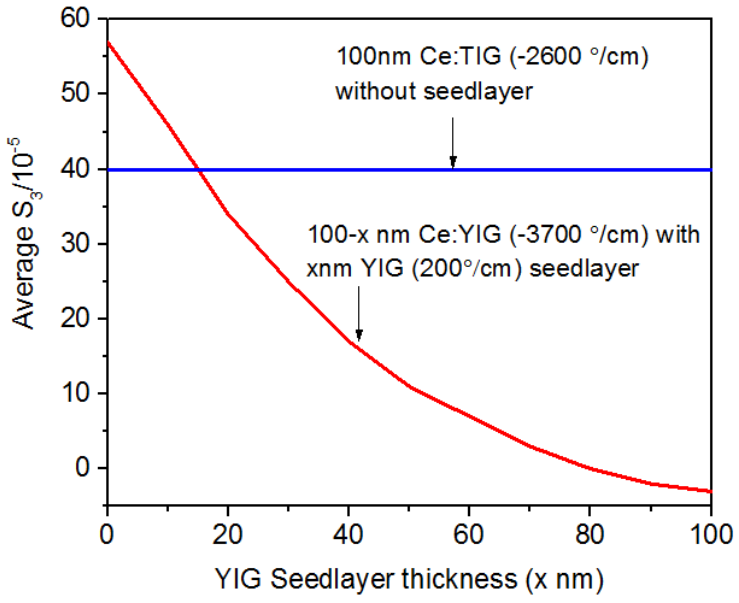

Figure 3-27: Average Stokes S_3 parameter comparison of an SOI waveguide device (identical dimensions) with Ce:TIG cladding (no seedlayer) vs Ce:YIG/YIG (i.e. Ce:YIG cladding with YIG seedlayer).

These results show that Ce:TIG cladding is a lot more efficient than the widely used Ce:YIG/YIG cladding on SOI waveguides. The inefficiency in the case of Ce:YIG is caused due to the opposite Faraday rotation chirality of Ce:YIG and YIG. The fact that Ce:TIG doesn't require a seedlayer makes it an excellent candidate for SOI waveguide optical isolator with garnet claddings even though it has lower Faraday rotation than Ce:YIG.

3.9 Quasi phase-matched (QPM) SOI waveguides

QPM, as introduced in section 1.1.8 can be used to eliminate the birefringence effects that occur when waveguide cross sections are anisotropic. Problems arise from slow growth rates which make it difficult to deposit thick films. In addition, photolithography can limit the ability to decrease waveguide widths, making square cross sections difficult to fabricate. Furthermore, isotropic waveguide cross-sections may be undesirable in semiconductor-core waveguides because this leads to the enhancement in polarization-mode scattering, which can compromise the coherence of the Faraday rotation. The anisotropic shape leads to differences in the propagation constants of TE and TM modes causing a limited, periodic mode conversion as the light propagates. QPM is a design in which the waveguide is segmented (Figure 3-28), with Faraday rotating (FR) and non-FR materials along the length of the waveguide with half the periodicity rotation chirality.

QPM SOI waveguides were designed and fabricated by Cui Zhang of Professor David Hutchings' group at the School of Engineering, University of Glasgow. Half beat length ($L_{\Delta\beta}$), optimum width of the waveguides, and thickness of garnet claddings were determined using modesolver simulations by these Glasgow collaborators. Various types

of garnet claddings were deposited on the waveguides and characterized at the University of Minnesota. Schematic of the waveguide is shown in Figure 3-28 and its cross section is in Figure 3-29. Final devices structures were characterized at Glasgow. Details on device fabrication and characterization can be obtained from the Ph.D. thesis of Dr. Cui Zhang [54].

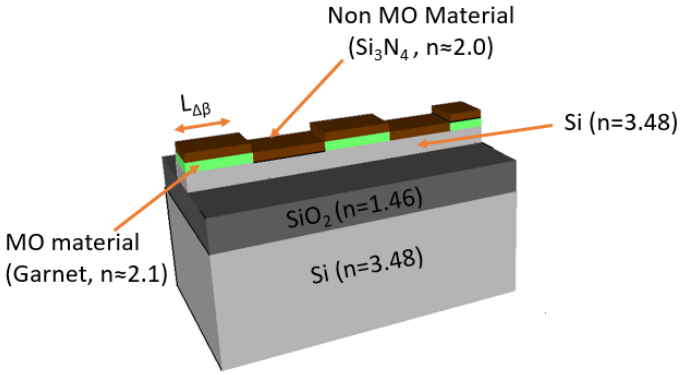

Figure 3-28: Schematic of QPM SOI waveguide with garnet cladding. MO here refers to Magneto-optic. Adapted from Cui Zhang's thesis [54].

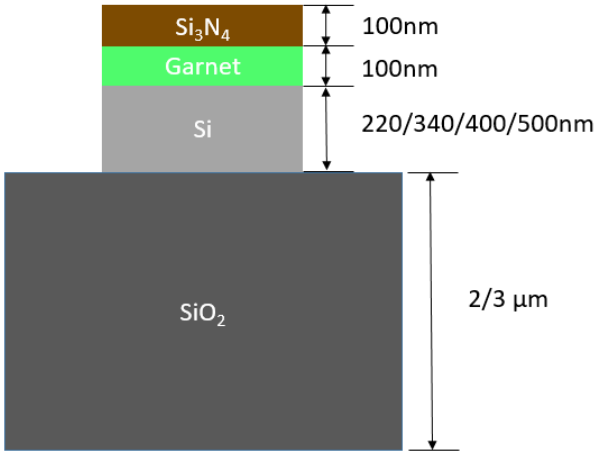

Figure 3-29: Cross section of the QPM SOI waveguide with garnet cladding. Adapted from Cui Zhang's Ph.D. thesis [54].

Waveguides of various heights (220nm, 340nm, 400nm and 500nm) and widths ranging from 600-1100nm were identified to be the most efficient from modesolver simulations. YIG, TIG, Ce:YIG (with YIG seed) and Ce:TIG were deposited on different waveguides by RF sputtering followed by RTA at 900°C for 2 minutes. Figure 3-30 shows optical (left) and SEM (right) images of QPM SOI devices with garnet claddings. The garnet claddings are thin (<100 nm) but this is sufficient to have an almost full interaction with the evanescent tail (discussed in section 2.12.1).

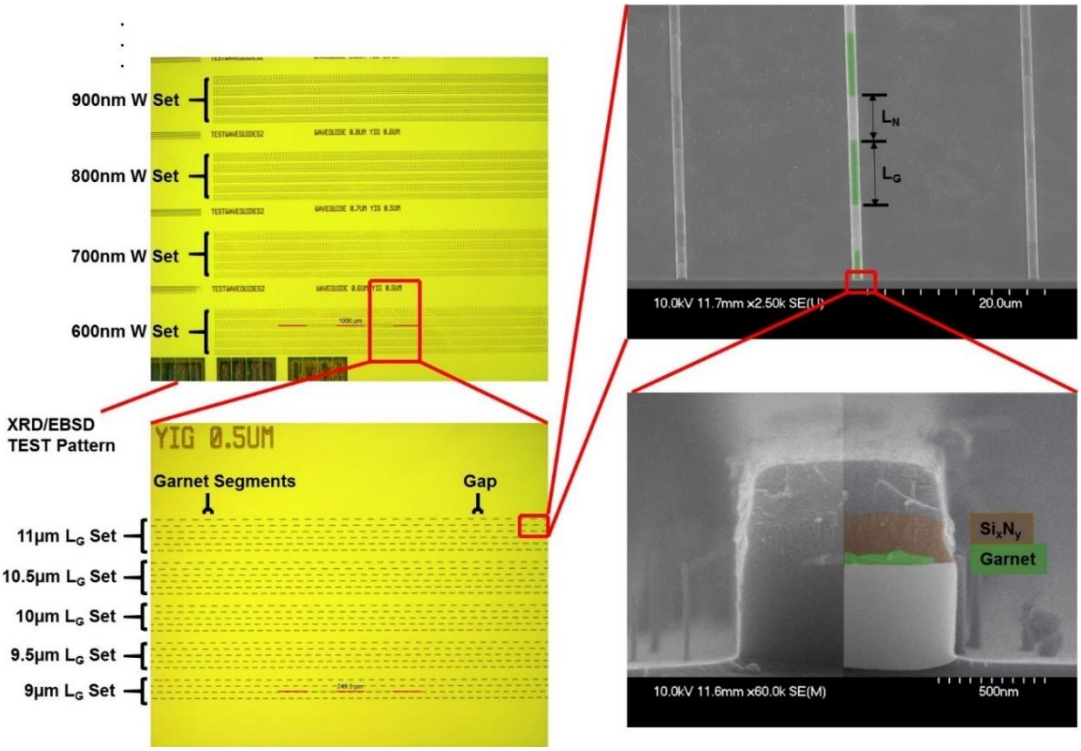

Figure 3-30: Monolithic integration of Faraday Rotation waveguide isolators. Optical (left) and scanning electron (right) micrographs showing the SOI waveguides with different widths (W), different garnet segment lengths (L_G), and a cross section of garnet cladding on SOI waveguides. Images taken by Cui Zhang.

Characterization of the crystallinity of the garnet films was done at the university of Minnesota. Figure 3-31 shows the SEM image of the waveguides and respective EBSD

patterns of Si and garnet. The grey lines on Figures (b) and (c) are the experimentally observed EBSD patterns, and the red and blue lines are the patterns for Si and garnet from the EBSD database. A comparison/matching of the two patterns is used to evaluate the crystal structure of the film. Crystallographic mapping of the garnet cladding was done using EBSD. The different colors in Figure 3-32 (a) represent the different crystallographic orientations of the garnet claddings whose legend is shown in by Figure 3-32 (b). The results suggest that the garnet claddings were partially crystallized and polycrystalline.

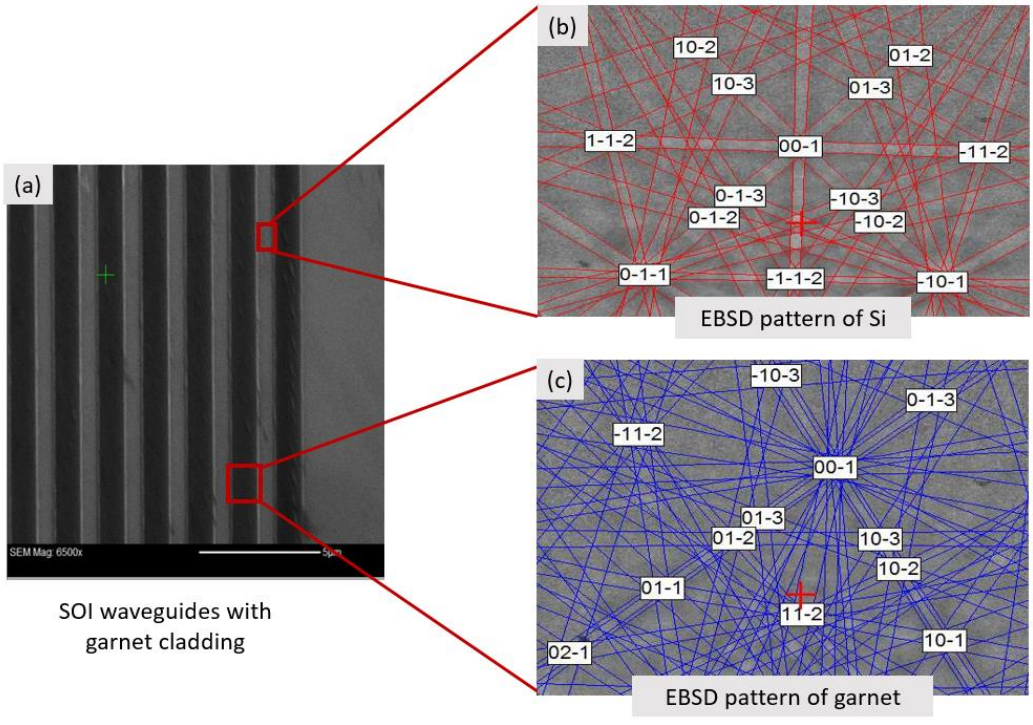

Figure 3-31: (a) SEM image of SOI waveguides and EBSD patterns of (b) Si and (c) garnet.

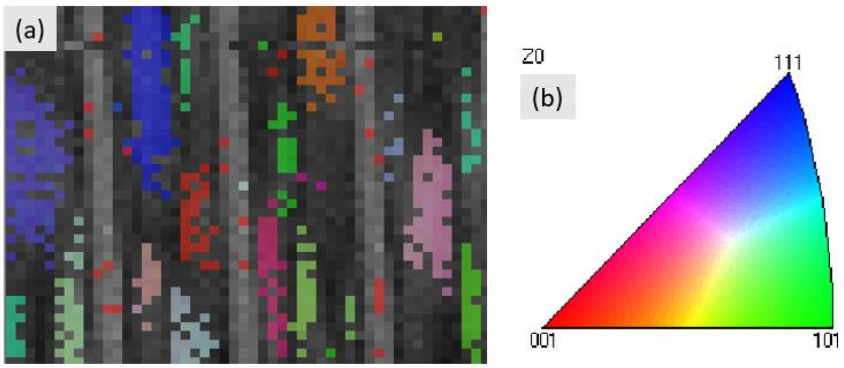

Figure 3-32: (a) EBSD (inverse pole figure) mapping and (b) Index of Crystallographic orientation of the garnet claddings on SOI waveguides.

The collaborative effort with the University of Glasgow has resulted in the first experimental realization of passive TE-mode SOI-integrated isolators using Faraday Rotation (FR), or nonreciprocal polarization conversion, the same phenomenon as that used in conventional optical isolators. These SOI FR isolators are similar in size to the currently popular TM-mode non-reciprocal phase-shift (NRPS) Mach-Zehnder interferometers (MZI) [71] and ring resonators [64]. FR isolators are essentially 1D (all in a continuous line) rather than 2D (e.g., to incorporate interferometer branches and rings), and this 1D geometry will enable very high device densities. Comparison of a Faraday Rotation waveguide vs the simplest form of a Mach-Zehnder Interferometer (MZI), both as TE-mode isolators on Si-on-insulator (SOI) waveguides with garnet top claddings can be seen from Figure 3-33 and Figure 3-34 respectively.

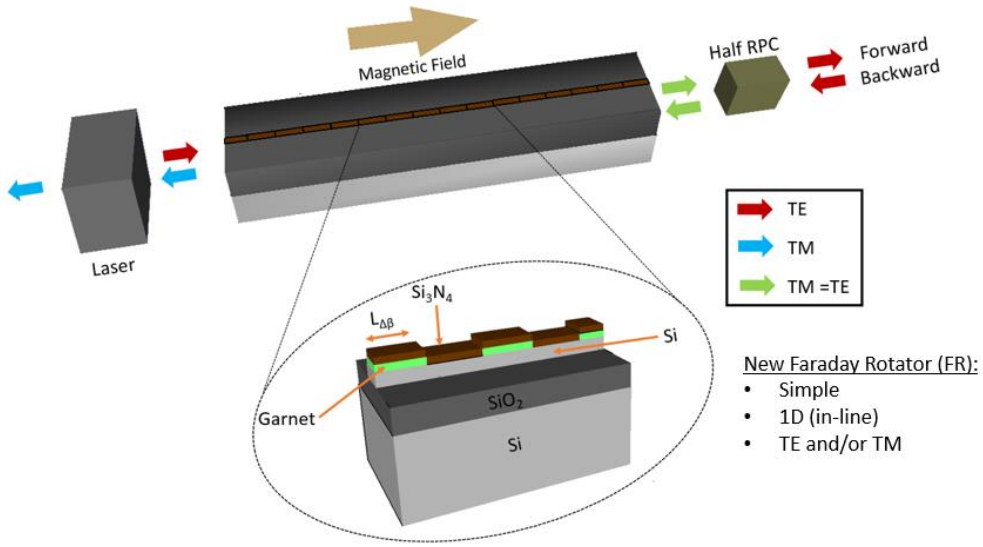

Figure 3-33: Schematic showing the components required for a Faraday Rotation waveguide isolator.

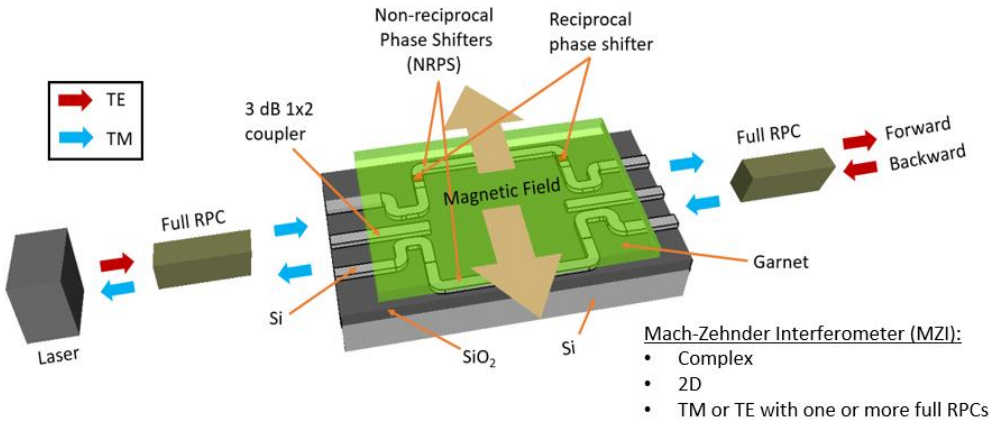

Figure 3-34: Schematic showing the components required for the simplest MZI-based isolator.

Unlike NRPS MZIs and ring resonators, FR isolators only require two elements for TE-mode operation: The Faraday Rotator (FR) and a half reciprocal polarization converter (RPC), Figure 3-33. The RPC is used to convert the [TE=TM] output of the FR to full TE-mode before the light continues into the photonic integrated circuit [53]. This is

considered a half converter because the light is only required to convert from half TE to full TE, and in principle should be more straightforward to realize than a full converter. Although mismatch in the TE and TM modal phase velocities can limit the transfer of energy between the modes in the FR, Figure 3-35, quasi-phase matching (QPM) can be used to compensate for the mismatch and ensure a monotonic flow of energy between the modes [72]. Polarization selectivity to isolate backward traveling TM modes can be provided by the selection rules of the semiconductor quantum well laser, which is essentially transparent to TM-polarized light. If necessary, a polarization filter can also be implemented [73].

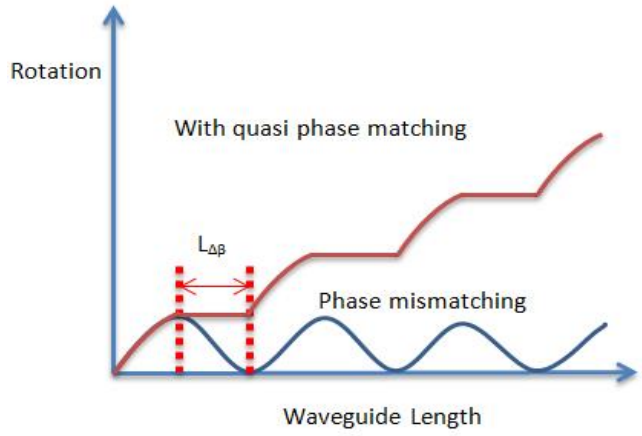

Figure 3-35: Schematic showing both the effects of phase velocity mismatch and the solution.

In contrast, for MZIs (Figure 3-34) to operate as TE-mode isolators, they require a full TE to TM RPC at the input, followed by a 1×2 coupler into the interferometer, where one or both of the waveguide branches have NRPS segments and/or reciprocal phase shifters (RPS). Next, a 2×1 coupler is used at the output where another full RPC [74], [75] is needed. Each one of these components will have affiliated efficiencies and losses, so 2-

component 1D FR isolators have great design appeal. Ring isolators will also need either two full RPCs, one on each end of a garnet top-cladded ring, or garnet could be coated inside the ring with a permanent magnet applying a non-uniform field [76]. However, TE-mode ring isolators have not been demonstrated on SOI to date.

Performance of SOI waveguides with Ce:YIG/YIG and Bi:TIG claddings were evaluated by Cui Zhang. The best isolation ratios among the various waveguides developed/tested were produced by a 500nm SOI isolator with Ce:YIG/YIG cladding (-8dB) and a 340 nm SOI waveguide isolator with Bi:TIG cladding (-11dB). Details on waveguide fabrication and characterization can be obtained from Cui Zhang's Ph.D. thesis [54].

This is the first report of an on-chip integrated TE-mode SOI isolator, and therefore is an important step in achieving new applications for photonic integrated circuits. These FR isolators are simple 2-component 1D (all in-line) waveguides with unique QPM claddings to overcome waveguide birefringence. Compared to NRPS devices, the design is sublimely simple, and the garnet claddings can be saturated at lower applied magnetic fields due to the longitudinal nature of FR which matches the garnet shape anisotropy.

3.10 Garnet core isolator simulations

3.10.1 Design of push/pull garnet isolators

The discovery of novel TIG films with equal, but opposite Faraday rotation chirality inspired a new design for QPM and 'push-pull' garnet core isolators [52], [77].

Waveguide devices were designed using Lumerical Finite Difference Time Domain (FDTD) simulations. Using the measured optical proper properties of TIG and Bi:TIG, the dielectric permittivity tensors, ε_{TIG} (Equation 3.1) and $\varepsilon_{Bi:TIG}$ (Equation 3.2) for these simulations were constructed with n = 2.1, λ = 1550nm , Faraday rotation (TIG) = 500°/cm and (Bi:TIG) = -500°/ cm. Fused quartz (n = 1.46) was used as the substrate material.

$$\varepsilon_{TIG} = \begin{bmatrix} 4.41 & 0 & 0.0009i \\ 0 & 4.41 & 0 \\ -0.0009i & 0 & 4.41 \end{bmatrix}$$

Equation 3.1: Permittivity tensor for TIG

$$\varepsilon_{Bi:TIG} = \begin{bmatrix} 4.41 & 0 & -0.0009i \\ 0 & 4.41 & 0 \\ 0.0009i & 0 & 4.41 \end{bmatrix}$$

Equation 3.2: Permittivity tensor for Bi:TIG

Simulations were performed using garnet waveguides with 2:1 aspect ratios (1.6 µm wide x 0.8 µm thick) whose schematic is shown in Figure 3-36. These dimensions are easy to fabricate, and present an extreme shape anisotropy compared to an isotropic (square) cross section.

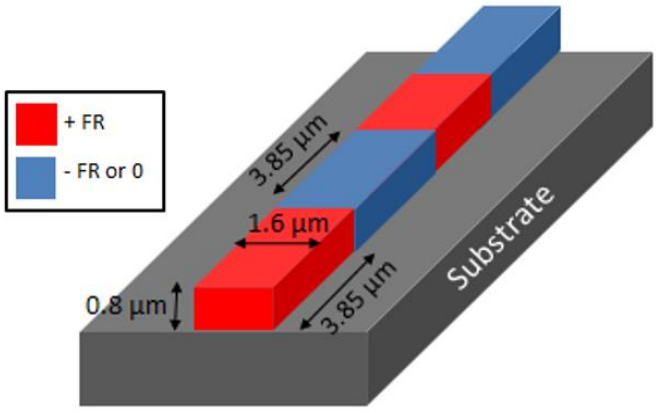

Figure 3-36: Schematic of quasi-phase matched (QPM: +FR & 0) and push-pull (+FR & -FR) garnet waveguides. Here, +FR and -FR refer to segmented materials with positive and negative chirality of Faraday rotation and 0 refers to materials that don't exhibit any Faraday rotation.

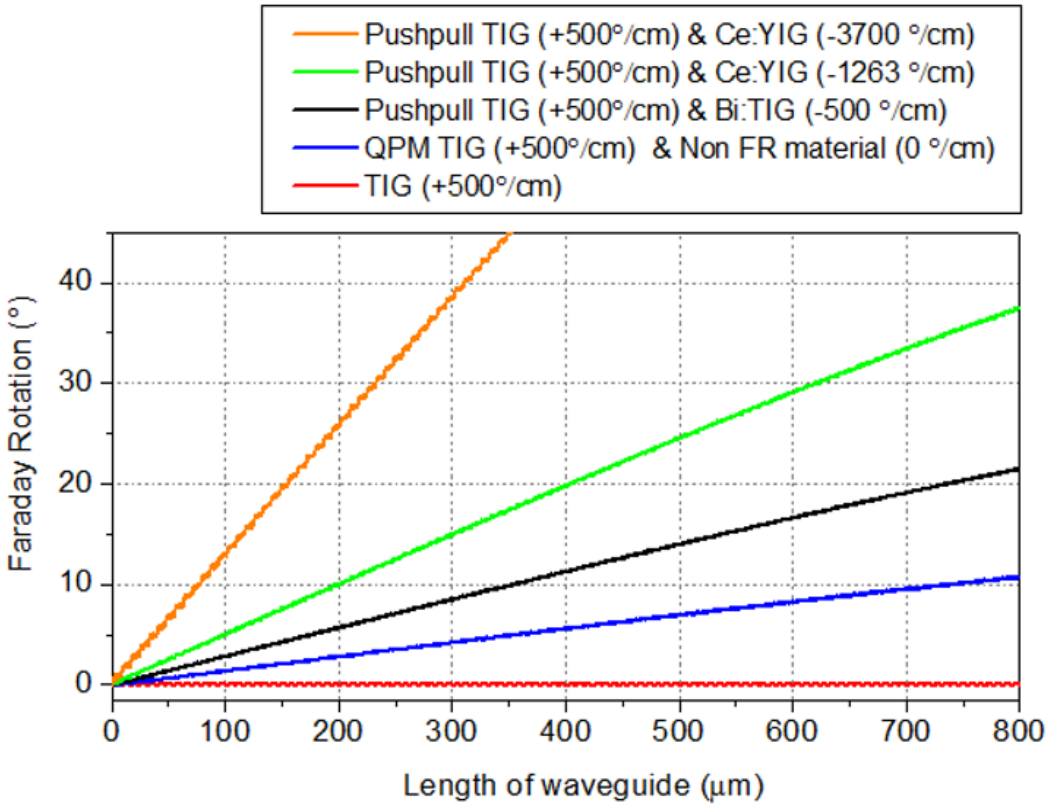

Figure 3-37: FDTD simulations of TIG, QPM TIG and different combinations of push-pull garnet waveguides of 1.6 µm x 0.8 µm cross section. The QPM and push-pull waveguides have 3.85 µm long strips on fused quartz substrate.

When the whole length of the waveguide is TIG, propagating light only rotates a fraction of a degree before returning to zero in a periodic fashion with a beat length of 7.7μm, shown by the red line in Figure 3-37. When propagating down a QPM waveguide, light encounters a new material at each point when it would otherwise rotate back to zero, namely every half beat-length (3.85μm). QPM TIG was simulated with +500 and 0 °/cm segments (blue line in Figure 3-37). This shows the ability of standard QPM to overcome birefringence, although not fully recovering the isotropic Faraday rotation. The opposite chiralities of TIG and Bi:TIG enables QPM to be extended into a novel "push-pull" garnet waveguide that provides much higher net Faraday rotation, as shown by the black line in Figure 3-37.

Push/pull QPM isolators were also simulated using TIG and monolithically-integrated Ce:YIG, which has much higher reported values of Faraday rotation (-1263°/cm [64] and -3700°/cm [21]). These devices had the same (1.6 μm x 0.8 μm) cross-sections. TIG and Ce:YIG segments were alternated every 3.85μm. The results, shown in Figure 3-37 indicate that these devices give rise to a full 45° Faraday rotation using a much smaller device lengths using bottom-seeded Ce:YIG, including only 350 μm using the -3700°/cm [21] Ce:YIG (orange). Full modal conversion (equal to 90° Faraday rotation) would then be reached by backward propagating light (45° forward + 45° backward) such that the reflection would be blocked by any polarization selecting device.

3.10.2 Fabrication tolerance

As with interferometer designs, fabrication tolerances could be an issue for device performance. However, here the issue is not length variations as with interferometers, but cross sectional variations. The periodicity of the QPM waveguide is determined by the differences that arise in the propagation constants of TE and TM modes due to the asymmetry of the height and width. This problem was addressed in the early days of YIG waveguide devices (on GGG) when birefringence was overcome by etch tuning methods [78], [79]. Here, one could pattern QPM strips, and then pattern the guides. If the fabricated width/height ratio doesn't quite match the QPM beatlength, the thickness of the guide would simply be etch-tuned until performance matches specifications.

It is often most economical to use thin films (small height) due to slow deposition rates and wide waveguides (large widths) due to inexpensive photolithography limits. In Figure 3-37, QPM results are shown for very practical dimensions (H=0.8 um and W=1.6um). These dimensions determine the device birefringence (that is, differences in TE vs TM propagation constants), which in turn determines the QPM beatlength.

To estimate the fabrication tolerances on the proposed devices, various widths and heights were simulated. The results are presented in Figure 3-38, Figure 3-39 and Figure 3-40.

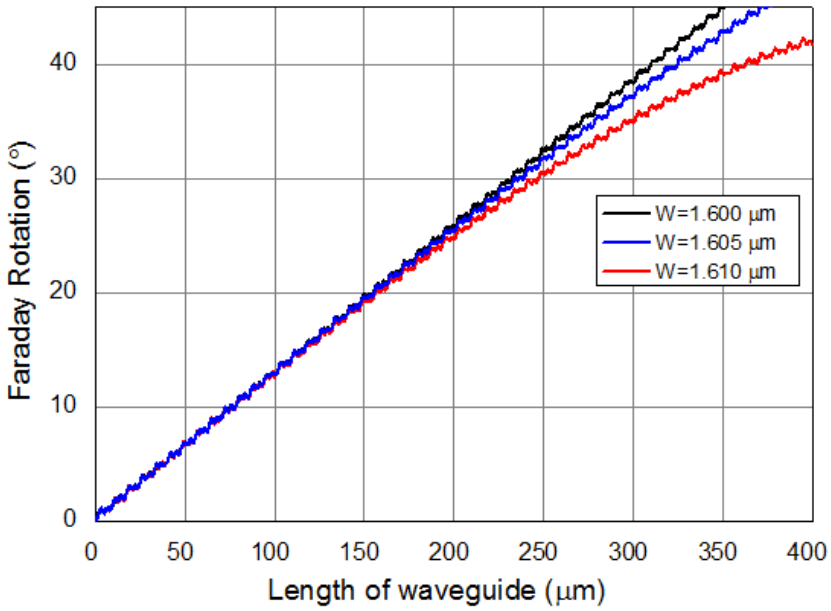

Figure 3-38: FDTD simulations of push-pull TIG (+500°/cm)/Ce:YIG (-3700°/cm) waveguides of thickness or height (H) = 0.8 μm with varying width (W).

Figure 3-38 shows the result of the FDTD simulations of push-pull TIG (+500°/cm)/Ce:YIG (-3700°/cm) waveguides of thickness or height (H) = 0.8 μm with varying width (W). The waveguides are segmented with a QPM beatlength of 3.85 μm on fused quartz substrate. This figure shows that width variations within +/- 5nm from a specified width have negligible impact on device performance. If fabrication error yields widths with more variation, the height can be etched to match the QPM condition with the obtained width (see Figure 3-39). Etch rates are easily slow enough to maintain this tolerance. Note: the cross section in this example is very asymmetric to demonstrate the power of QPM, but designs with more isotropic cross sections (W=H) will be less sensitive.

Figure 3-39 shows the result of the FDTD simulations of the waveguides are segmented with a QPM beatlength of 3.85 μm on fused quartz substrate. Heights within +/- 1nm

from specified height only have negligible impact on device performance. Etch rates are easily slow enough to maintain this tolerance. Note: the cross section in this example is very asymmetric to demonstrate the power of QPM, but designs with more isotropic cross sections (W=H) will be less sensitive.

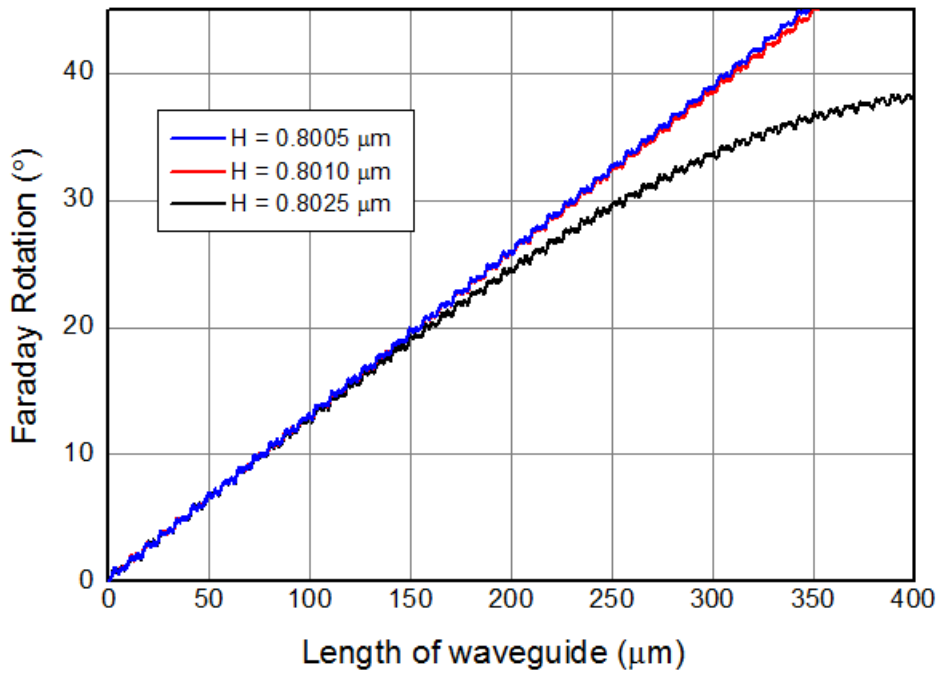

Figure 3-39: FDTD simulations of push-pull TIG (+500°/cm)/Ce:YIG (-3700°/cm) waveguides of width (W) = 1.6 µm with varying thickness or height (H).

Figure 3-40 shows the result of the FDTD simulation of push-pull TIG (+500°/cm)/Ce:YIG (-3700°/cm) waveguide of thickness or height (H) = 0.802 µm and width (W)=1.610 µm. The waveguides are segmented with a QPM beatlength of 3.85 µm on fused quartz substrate. This figure uses the QPM beatlength that was optimized for height (H) = 0.800 µm and width (W)=1.600 µm. If, however, the waveguide was +10nm from specified, an additional height of 2nm will restore device performance as the new W/H

pair will also meet the specified QPM beatlength. Of course, the films will need to be made slightly thicker if it is known that the width patterning will vary in the + direction to allow proper etch back.

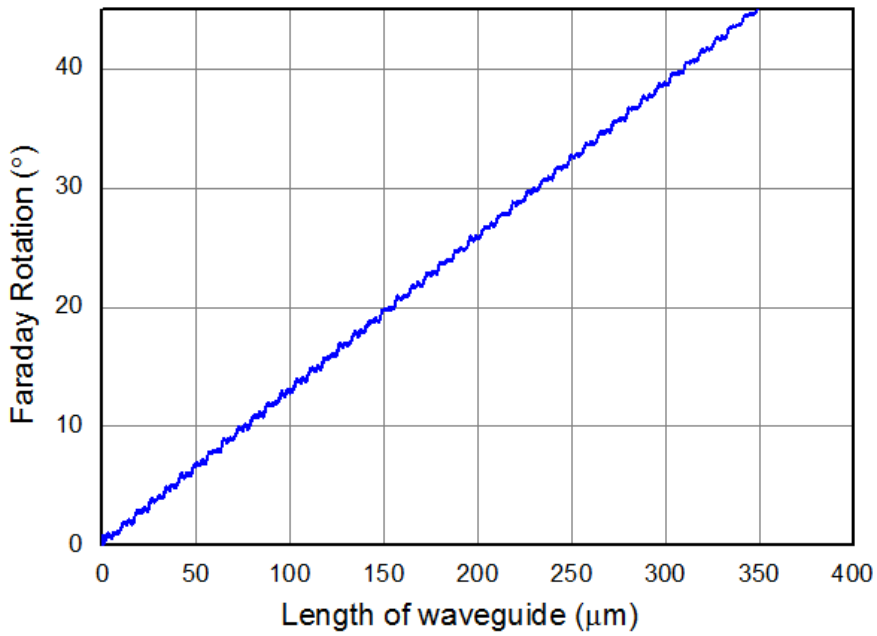

Figure 3-40: FDTD simulation of push-pull TIG (+500°/cm)/Ce:YIG (-3700°/cm) waveguide of thickness or height (H) = 0.802 μm and width (W)=1.610 μm.

To summarize the fabrication tolerance results, a waveguide that is within +/- 10nm in width (Figure 3-38) of the intended value could be etched back to a height that is within +/- 2nm of the matching QPM height (Figure 3-40) to regain full performance. Control of garnet etch rates is straightforward using temperature during a phosphoric acid etch (1nm/sec at 120°C [78] and slower at room temperature), so this tolerance would be easy to obtain. To verify this technique, a matching width/height pair was simulated (Figure 3-40) to show full device performance. Once optimized, it is important to

appreciate that, unlike interferometers, these devices allow complete polarization diversity, meaning they can be applied for all polarizations from TE to TM photonic integrated circuits.

4 Fabry-perot Faraday Rotators

4.1 Introduction

A Fabry-Perot interferometer comprises of two partially reflecting surfaces parallel to each other. When light enters the cavity, it gets reflected multiple times and can constructively or destructively interfere depending upon the relationship between the size of the cavity and the wavelength of light. A schematic of the process is shown in Figure 4-1. Constructive interference occurs if the cavity length is evenly divisible by a half-wavelength. This is mathematically shown in Equation 4.1, where *d* is the cavity length, *n* is an integer and λ is the wavelength.

$$d = \frac{n\lambda}{2}$$

Equation 4.1: Condition for constructive interference in a Fabry-Perot interferometer.

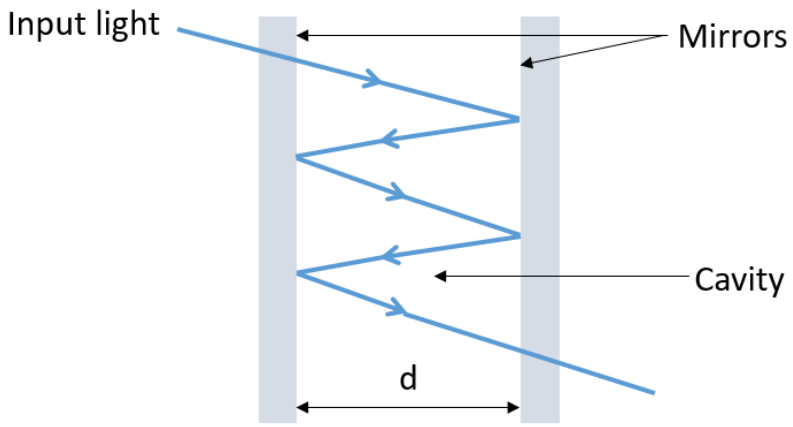

Figure 4-1: Schematic of the Fabry-Perot interferometer.

4.2 Integrating Faraday rotator with Fabry-Perot interferometer

A novel idea inspired by integrating the idea of a Fabry-Perot interferometer with garnet was explored. The goal was to achieve an intensification in Faraday rotation by using a garnet film as the cavity with reflecting surfaces on either side. Garnet films were grown on a reflective substrate. While the substrate acted as one of the mirrors, the other reflecting surface was designed using a multi layered stacks with different refractive indices. A conceptual diagram is shown in Figure 4-2. Here, the films with different indices act as semi-reflecting mirrors. Incoming light would pass through these stacks and resonate while experiencing a rotation in polarization due to the Faraday effect in the garnet layer. A peak in reflection occurs with a peak in Faraday rotation when the resonant condition is met by the cavity.

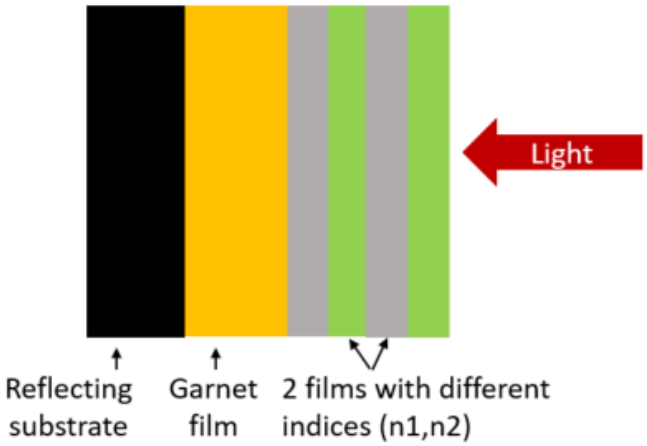

Figure 4-2: Schematic of the proposed reflective Fabry-Perot Faraday rotator.

4.3 Materials development and characterization

Mirror and the garnet defect layer (cavity) materials were developed for 780nm wavelength. While crystalline Ce:YIG (Ce-doped yttrium iron garnet) was used as the magneto-optical layer in order to cause the polarization rotation, amorphous YIG (yttrium iron garnet) and SiO_2 (silicon dioxide) were picked as the semi-reflecting mirror stacks.

4.3.1 Material growth and characterization

The samples were fabricated using multi-target Radio Frequency (RF) sputtering in a sputter down configuration (discussed in section 1) on single side polished Si substrates that were placed at the center of a stage rotating at 30 RPM. To ensure the cleanliness of the substrates, they were subjected to a 5-minute sonication of acetone, followed by methanol, isopropanol and deionized water in a cleanroom facility.

4.3.1.1 Magneto-optical (defect layer): Ce:YIG

The Ce:YIG layer was developed first. However, since Ce:YIG cannot be grown directly on the Si substrates (this leads to the formation of CeO_2 rather than garnet), a thin layer of YIG (seedlayer) was deposited and annealed prior to growing Ce:YIG. For the seedlayer, a Y_3Fe_5 target was sputtered at 240W, flowing in Ar at 20sccm and O_2 at 2.0 sccm. The chamber pressure varied between 2.2×10^{-3} – 2.4×10^{-3} Torr. Following the deposition, the YIG seedlayer was then annealed using rapid thermal annealing (RTA) for

2 minutes at 900°C in an O_2 environment. Next the Ce:YIG defect layer was grown by sputtering a Ce metal target at 40W along with the Y_3Fe_5 target (240W). O_2 was flown in at 1.8sccm. Just like the YIG seedlayer, the Ce:YIG film was also annealed using RTA for 2 minutes at 900 °C in an O_2 environment.

4.3.1.2 Test for potential mirror materials; amorphous YIG and SiO_2

The amorphous YIG film was grown on Si substrate by sputtering the Y_3Fe_5 target at 240W. The SiO_2 film was grown by sputtering the Si target at 250 W. Both were done at an Ar flow rate of 20 sccm and O_2 flow of 2.0 sccm.

4.3.2 Crystallinity characterization of Ce:YIG

X-ray diffraction (Bruker D8 Discover) was used to analyze the crystal structure of the YIG seedlayer and the Ce:YIG film.

The results are shown in Figure 4-3 which prove that both the YIG seedlayer and the Ce:YIG films are single phase (garnet). Note that the mirrors (YIG and SiO_2 stacks) were not annealed, and hence they stayed amorphous.

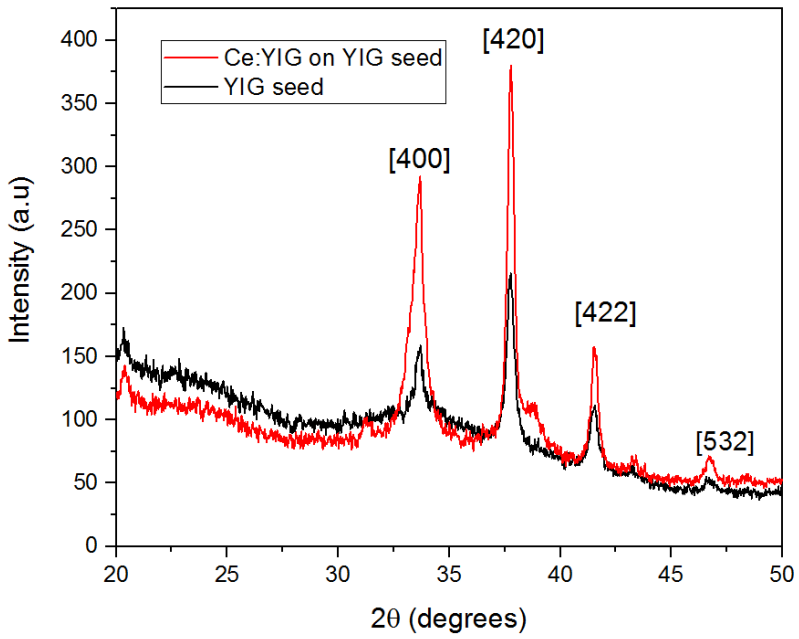

Figure 4-3: XRD of YIG seedlayer and Ce:YIG grown later on the same YIG seedlayer on Si substrate.

4.3.3 Compositional characterization of defect layer

Since the refractive index of the Ce:YIG varies depending upon the Ce- concentration, it is important to keep the composition uniform. The composition of this film was measured using EDS and the result is shown in Table 4-1.

Element	Weight %	Atomic %
Fe	47.50	62.13
Y	34.96	28.72
Ce	17.55	9.15
Total	100	100

Table 4-1: Compositional analysis of Ce:YIG film used as the defect layer.

4.3.4 Measurement of optical constants and thickness

Control in thickness and accurate refractive index measurement of each film is important to achieve the enhancement in Faraday Rotation at the intended wavelength.

Optical constants, i.e. refractive index (n) and extinction coefficient (k) of each of the films were measured using a VASE spectroscopic ellipsometer doing a wavelength sweep. The data is shown in Figure 4-4. The thickness of each film measured using profilometry is shown in Table 4-2.

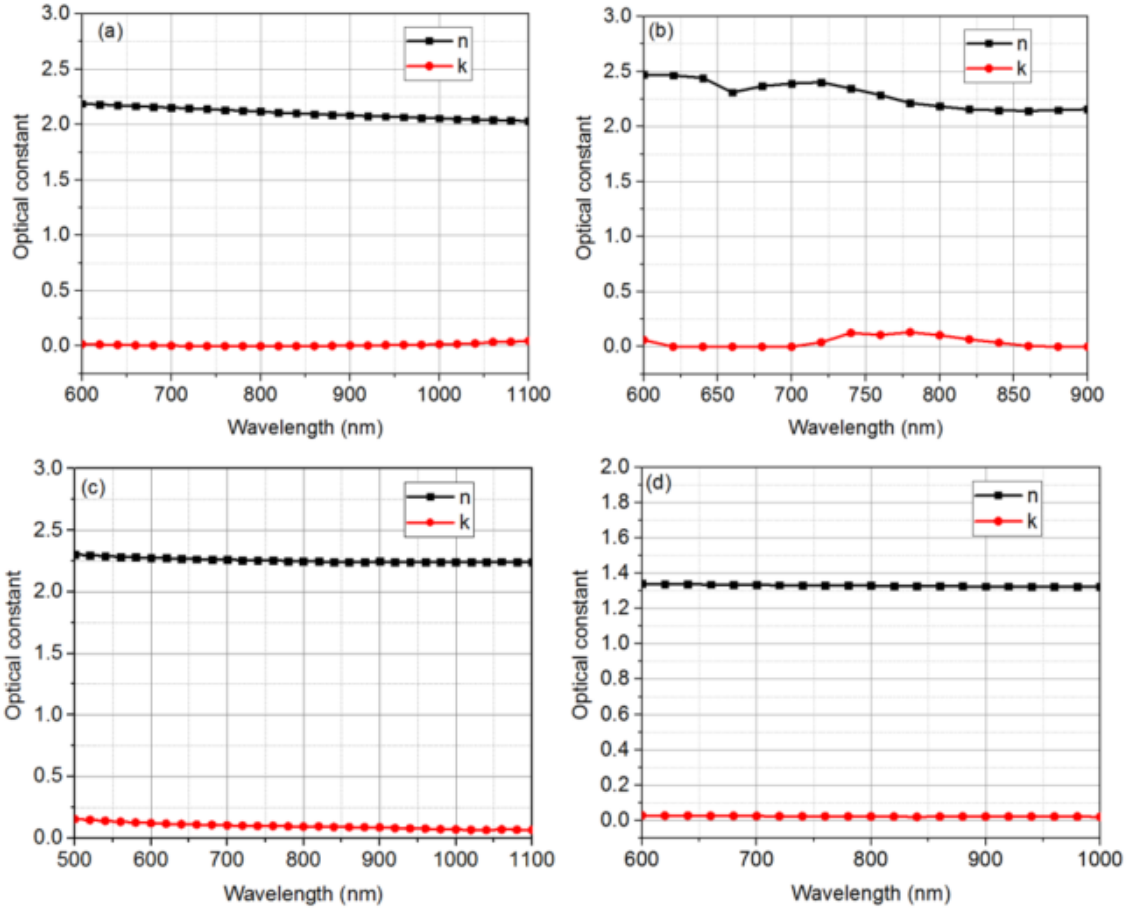

Figure 4-4: Optical constants of (a) Annealed YIG (b) Ce:YIG (c) amorphous YIG and (d) SiO_2.

Film	Thickness (nm)
Annealed YIG	55
Ce:YIG with YIG seed	300
Amorphous YIG	55
SiO_2	30

Table 4-2: Thickness of each film measured using profilometry.

4.3.5 FDTD simulations of reflective Fabry-Perot rotators

The stack thicknesses needed for 780nm Fabry-Perot Faraday rotator were calculated using Equation 4.1. The resulting thicknesses are indicated in the schematic in Figure 4-5.

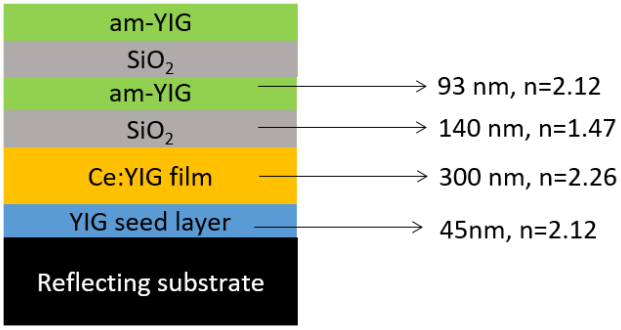

Figure 4-5: Fabry-Perot Faraday rotator stack simulated with FDTD. am-YIG refers to unannealed or amorhous YIG.

FDTD simulations were performed on the stack shown in Figure 4-5. First, the reflectance of several materials (only substrates, no stacks) were simulated using the material database in FDTD solutions software package from Lumerical solutions. The results are shown in Figure 4-6, which are in compliance with literature values [36], [51].

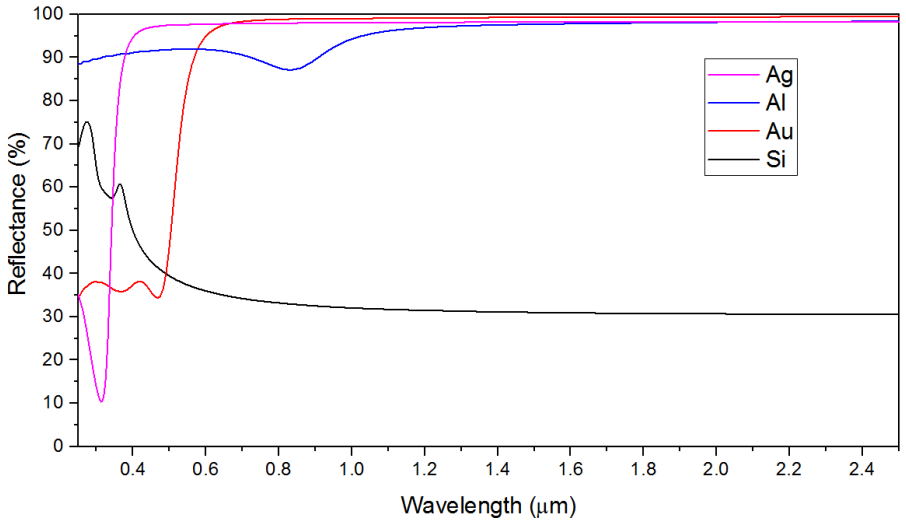

Figure 4-6: Reflectance of 0.5mm Ag, Al, Au and Si substrates.

Next, a simulation was done to see the difference between just a Ce:YIG film vs a Ce:YIG film with the 2 pairs or 4 mirrors on Ti substrate. The results are shown in Figure 4-7. The obvious difference is in the dip at approximately 840nm caused due to the transmission through Ce:YIG.

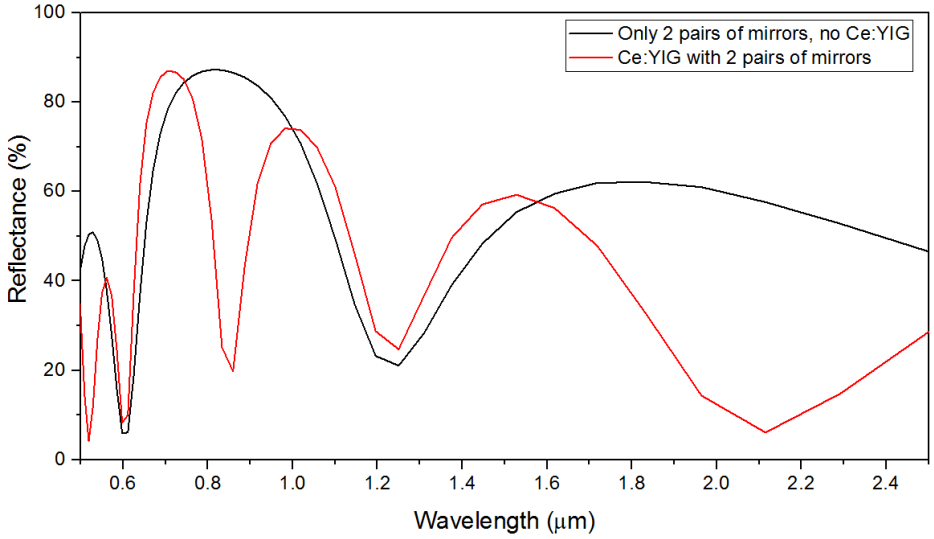

Figure 4-7: Reflectivity of Ce:YIG with and without the mirror stacks. Ti substrate.

A test of thickness tolerance was done adding 10% on the thickness of the mirrors on the stack with Ce:YIG on Ti substrate (Figure 4-8). Following this, a tolerance of index change was tested, changing the index of the a-YIG from 2.2 to 1.9 (Figure 4-9). A slight shift in the entire spectra is observed in both cases which highlights the need for good control in thickness/deposition rate and refractive index of the material.

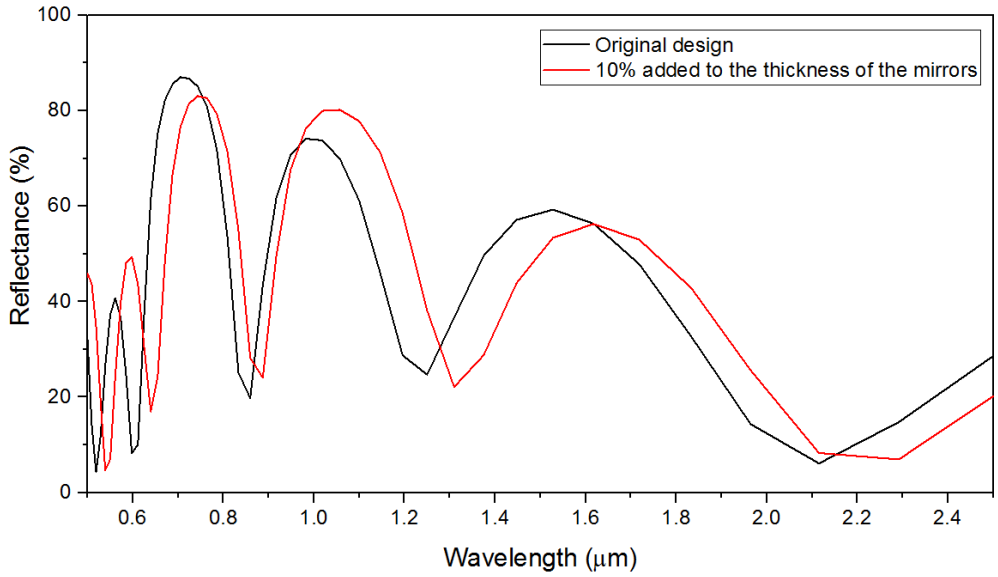

Figure 4-8: Test of thickness tolerance; original design vs design with 10% added to the thickness of the mirrors. Ti substrate.

Further simulations, reducing the mirror thickness to half of the schematic in Figure 4-5 were done to see the effect at the intended wavelength. Results, which are shown in Figure 4-10 indicate that half thickness leads to much less reflectance as compared to the original thickness.

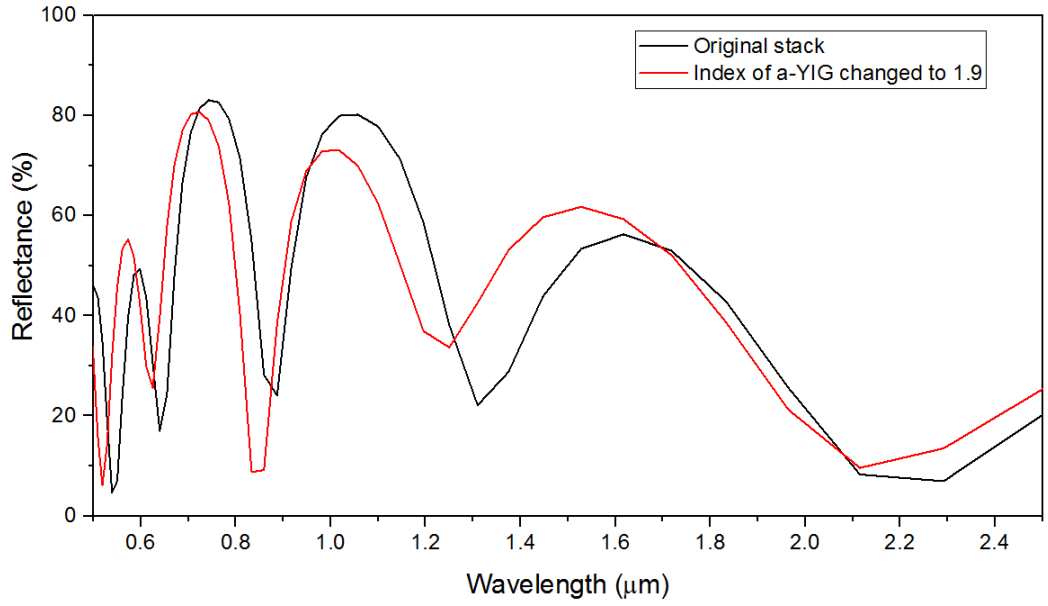

Figure 4-9: Test of tolerance in index change; reflectance of original stack vs stack with the index of amorphous YIG changed to 1.9. Ti substrate.

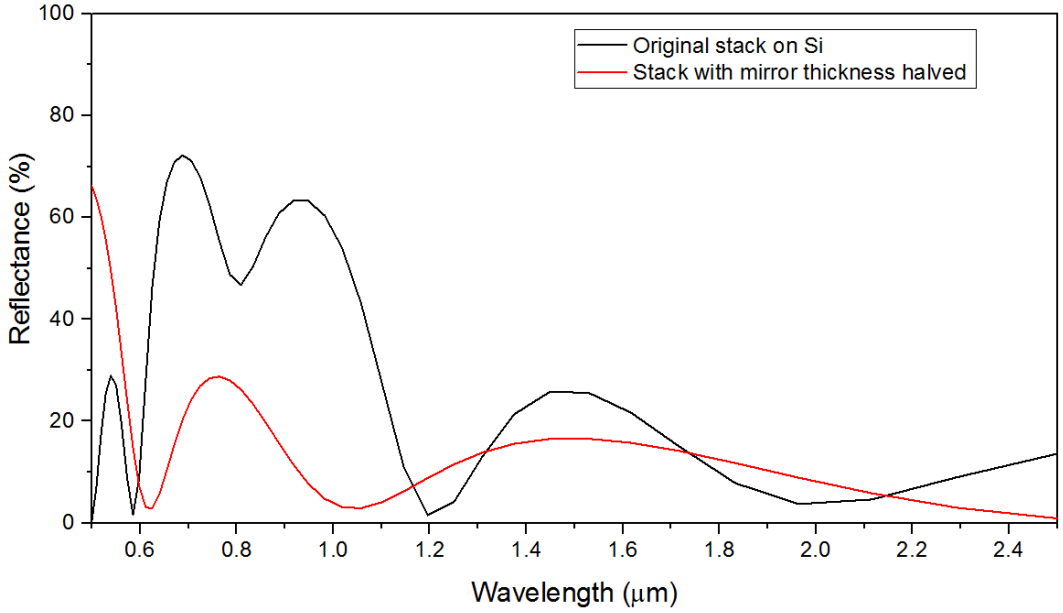

Figure 4-10: Reflectivity of original stack compared to stack with mirror thickness (both a-YIG and SiO_2 halved). Simulation on Si substrate.

Furthermore, the effects of the reversing the order of the mirrors was also simulated.

Result (Figure 4-11) shows that the original mirror order leads to best results for the

targeted wavelength (780nm) but tuning the reflectance based on wavelength can be done by reversing the mirror order.

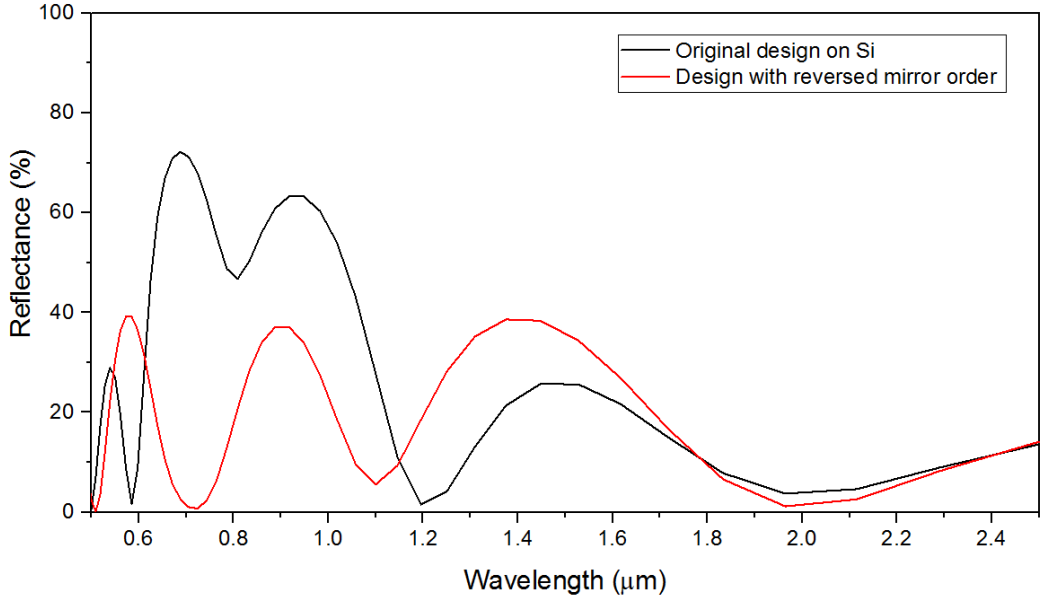

Figure 4-11: Reflectivity of original stack on Si vs stack with mirror order reversed.

4.3.6 Fabrication of stacks for reflective Fabry-Perot rotators

Based on the knowledge from the simulations, Si substrate was used to grow the stacks. 2 pairs and 5 pairs (i.e. 4 and 10 stacks respectively) of mirrors were grown on the samples to see how the effect enhanced by increasing the number of mirrors. Reflectance measurement was done in a Perkin Elmer Lambda 950 UV-VIS spectrometer. The result is shown in Figure 4-12. The data shows a standard interference pattern expected for a Fabry-Perot stack. However, it shows a peak in reflectance at almost twice the target wavelength of 780nm. This hints that the target wavelength can be achieved by making the layers half as thick as the current design. It is

also likely that this design could work for a transmission rather than a reflection at telecommunication wavelengths.

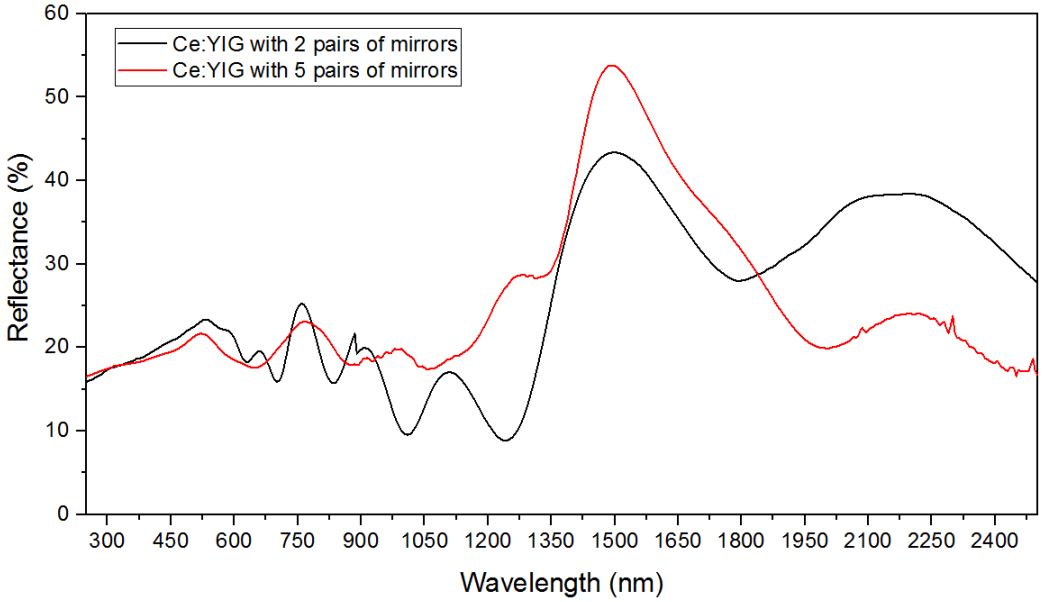

Figure 4-12: Reflectance measurement (experimental) of Fabry-Perot Faraday rotators on Si substrate with different number of mirror stacks (2 pairs and 5 pairs).

Faraday rotation was measured at 1400nm, 1500nm and 1600nm wavelength in a reflection setup described by the procedure in section 2.7. The data (Figure 4-13) shows that the Faraday rotation produced by both samples at 1600nm is 10x of what was observed at other wavelengths. This corresponds to the surge in reflectance at around 1600nm as seen in Figure 4-12.

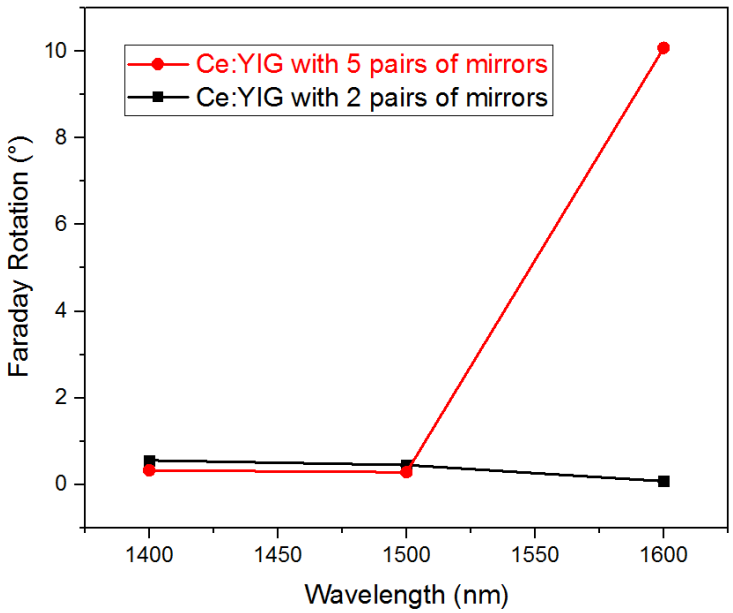

Figure 4-13: Faraday rotation measurement of Ce:YIG films with 2 pairs and 5 pairs of mirrors measured at 1400, 1500 and 1600nm.

In summary, this experiment was a proof of concept, which is yet to work at the target wavelength, but the enhancement of reflection (Figure 4-12) and Faraday rotation (Figure 4-13) at 1500-1600nm shows that the concept is viable and that more work is needed to achieve the result at the intended wavelength.

4.3.7 Transmitting Fabry-Perot rotators

Fabry-Perot rotators in a transmission setup were explored. A schematic of the transmitting design is shown in Figure 4-14. Here, the idea is that the light enters perpendicular to the sample, and experiences an intensified Faraday rotation due to the resonance from the mirror cavities and transmits through the substrate.

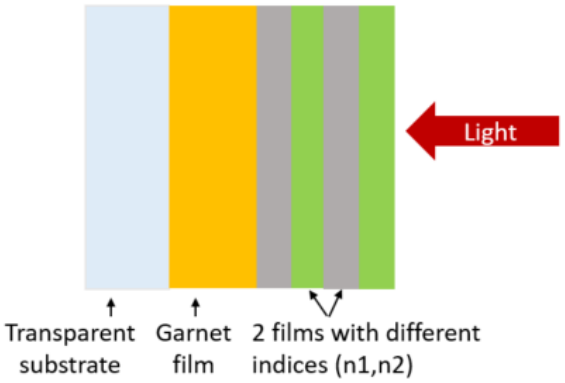

Figure 4-14: Schematic of transmitting Fabry-Perot Faraday rotator.

Various factors are important when it comes to designing such a structure. Material properties is the primary consideration. To crystallize, the garnet needs to be annealed at 900°C. Hence, it is important to pick a substrate that has a comparable coefficient of thermal expansion (CTE) and somewhat different refractive index (to cause reflections and allow for resonance) than garnet. Considerations of substrates were based on the following materials parameters of YIG; CTE= 9.9-11.4 ppm / °C and unit cell= 12 Å and n=2.1 at 780nm. The summary of these parameters, along with their respective costs for three different materials is given in Table 4-3.

Substrate	Cost (per pc) US$	n (780nm)	CTE (ppm / °C)	Unit cell (Å)
Sapphire (Al_2O_3)	29.95	1.76	7.5	A=4.758 C=12.99
YSZ (Cubic Y_2O_3 stabilized ZrO_2)	29.95	2.1366	10.3	5.125
GGG (Gadolinium gallium garnet)	99	1.95	8.3-8.7	12.376

Table 4-3: Parameters of transparent substrates (780nm).

Table 4-3 shows that although GGG is the closest to garnet considering the similarity in material properties, the cost is fairly high. Hence sapphire (Al_2O_3) and cubic yttrium-stabilized zirconia (YSZ) were chosen as substrates to use for these transparent rotators.

First step was to grow garnet on both YSZ and sapphire substrates. Upon annealing at 900 °C, the films remained intact and produced single phase garnets as shown by the XRD data in Figure 4-15. Mirror stacks on top of the Ce:YIG films are currently being developed at the University of Minnesota.

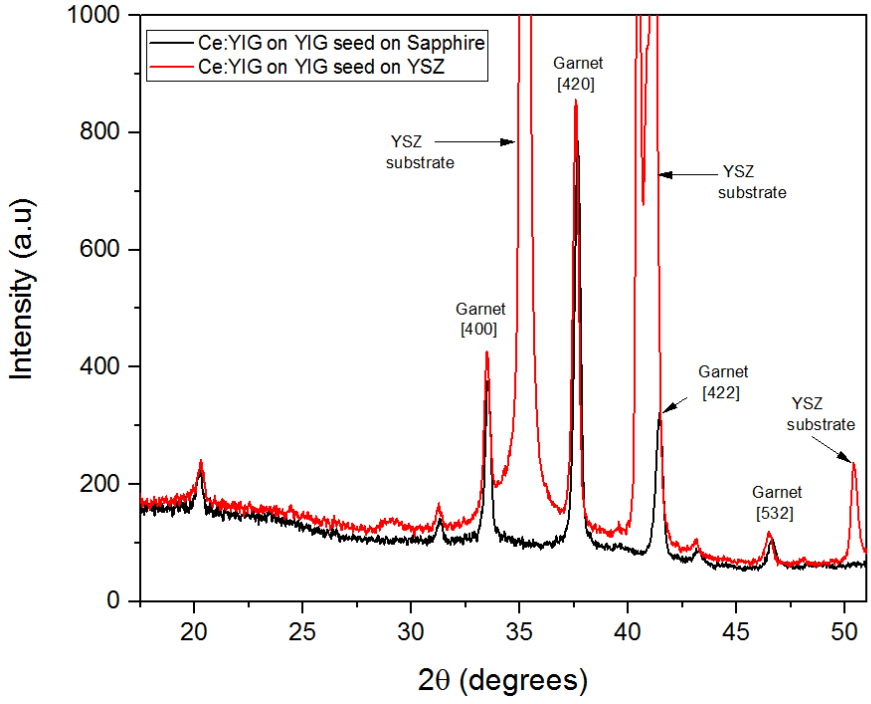

Figure 4-15: Ce:YIG grown on YIG seedlayer on transparent sapphire and YSZ substrates.

5 Development and Characterization of Gold Thin Films for Heat Assisted Magnetic Recording

As introduced in section 1.2, heat assisted magnetic recording (HAMR) is a promising magnetic recording technique that employs novel recording heads utilizing the principles of plasmonics. Using a combination of laser and near field transducers (NFTs), the recording head heats up the media above its Curie point. This reduces the coercivity of the media, making it easier to write the data. Writing is followed by immediate cooling to store the data. Different shapes of the NFTs have been explored. One of the commonly reported shape is the 'lollipop' shaped NFT [35], [80]. In this design, the laser light generates surface plasmons which oscillate at resonance along the peg length and couple the energy into the recording medium. This design allows for high efficiency coupling in order to heat very small spots (50nm) in the recording media. Gold (Au) is a commonly used material to develop NFTs because of its plasmonic properties, chemical inertness and high melting point of 1060°C [81].

The plasmonic resonant frequency of the NFT depends upon the morphology of the film, which in turn affects how the data is written on the recording medium. The success of HAMR relies on the efficient heating the recording medium, which involves heating the NFTs. Heating deforms the gold nano NFTs which changes the resonant frequency [35]. Thus, the understanding of the morphology and the deformation process of the NFT material is crucial for a HAMR system.

5.1 Crystal structure and thermal deformation of gold films

Gold nanoparticles demonstrate different crystallographic orientations based on their nanostructures. Studies show that stable Au nanorods are composed of {110} facets whereas Au nanospheres are made up of {111} and {100} structure [82]. Table 5-1 gives the comparison of the surface energy of the different facets of gold. As deposited films have a very strong {111} texture because it is the lowest energy state and hence the {111} facet tends to be the most stable [83]. Upon thermal treatment, {100} facets tend to reconfigure to the lower energy and hence more stable {100} and {111} orientations [84].

Surface	Energy (J/m^2)
{111}	1.283
{100}	1.627
{110}	1.700

Table 5-1: Surface energy of different orientations of Au [85].

5.2 Crystallographic study of Au thin films using Electron backscattered diffraction

A crystallographic study of Au films was performed using electron backscattered diffraction (EBSD). Background and working principle of this technique have been discussed in section 2.6. The resolution of EBSD depends upon the interaction volume of the electrons with the samples [86]. To decrease the interaction volume (which increases the resolution), EBSD for the Au films was done in a transmission mode (t-EBSD). 25nm thick Au films (provided by Seagate Technology) were deposited on commercially available TEM membranes with electron-transparent 5nm thick Si_3N_4

windows purchased from TEMwindows.com as shown in Figure 5-1. With the help of a custom-made t-EBSD holder (courtesy: Nick Seaton, UMN Characterization facility), the TEM membranes were placed at a -10° tilt as shown by the blue line in Figure 2-7. Data analysis and post-processing of the t-EBSD was performed using HKL Channel 5 EBSD software modules (Tango, Mambo, Salsa).

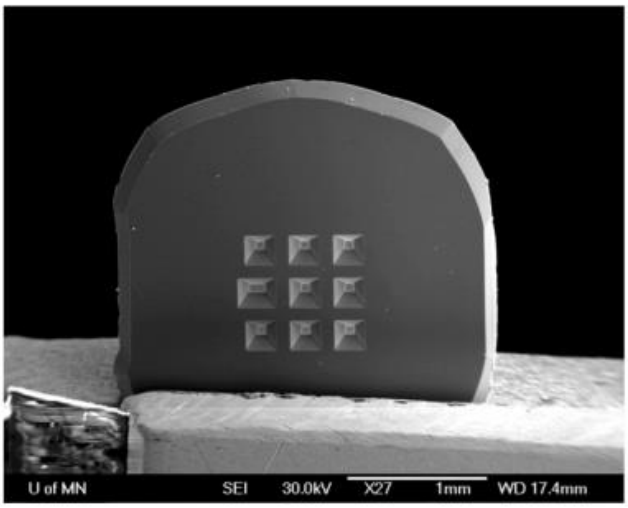

Figure 5-1: SEM image of the membrane used for the t-EBSD of Au films. Courtesy: Eliot Estrine.

Information on the crystal structure of the Au films was extracted from the Kikuchi diffraction patterns obtained from t-EBSD. An example of the Kikuchi diffraction patterns from Au is shown in Figure 5-2. The grey lines in the figure represent the experimentally obtained Kikuchi patterns which are juxtaposed with the pattern available on the EBSD database (red lines). This matching/indexing is automatically performed by the EBSD software. The pattern in Figure 5-2 corresponds to the <111> crystallographic orientation that is perpendicular to the substrate which is represented by the cube in the inset.

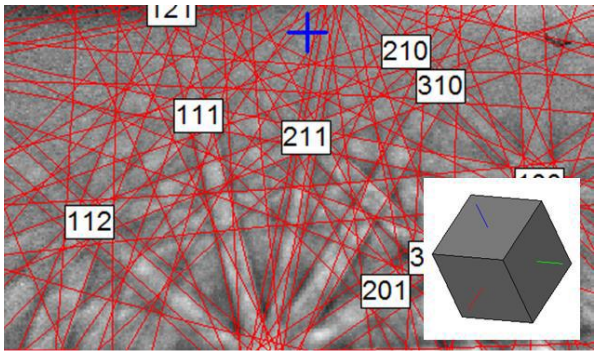

Figure 5-2: Kikuchi pattern of Au film deposited on 5nm thick Si_3N_4 windows.

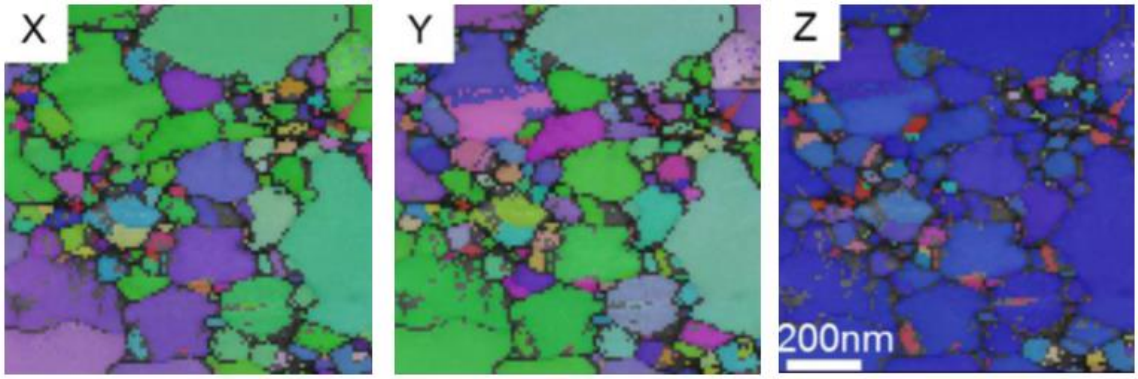

Figure 5-3: Euler map of crystallographic orientation of the Au grains in X, Y and Z directions. X and Y are the directions parallel to the plane of the film/substrate and Z is the perpendicular direction. Legend of the color scheme is shown in Figure 5-4.

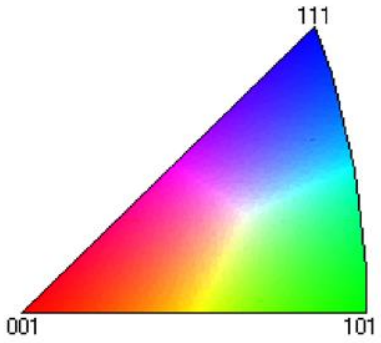

Figure 5-4: Coloring scheme legend of the inverse pole figure mapping shown in Figure 5-3.

In addition to obtaining the Kikuchi diffraction patterns, the electron beam raster scans to produce a (Euler) crystallographic mapping of the film. An example of such mapping of the as-deposited Au films is shown in Figure 5-3, where X, Y and Z represent the direction of the different crystallographic directions. X and Y are the directions parallel to the plane of the film/substrate, whereas Z direction represents the perpendicular direction. The color scheme represents the different crystallographic orientations which is shown by the index in Figure 5-4. As seen from the Z direction mapping, the Au films have a strong <111> texture.

5.3 Heat treatments of Au films

To begin studying the deformation of Au films, a two-step thermal treatment experiment was performed on a 25nm Au sheet film deposited by sputtering on the TEM membrane shown in Figure 5-1. The sample was first subjected to a 300°C anneal for 30 minutes. Following this, a t-EBSD mapping was performed on a specific region of the film. Another 30 minutes of annealing at 350°C was performed on the same sample, following which another EBSD mapping was repeated on the same region. The process and result is summarized by Figure 5-5. A subtle change in the Z-mapping resulted in this experiment. All the grains represented by the green regions (non <111> grains) observed after the first anneal step seem to have turned into blue colored <111> grains during the second anneal step. In addition to this, the dark blue grains seem to be getting closer to purple upon the second anneal step. This suggests two things; first is that upon thermal treatment, the grains closer to <101> orientation tend to orient

closer to the <111> direction. Furthermore, all the grains tend to structure slightly away from perfect <111>.

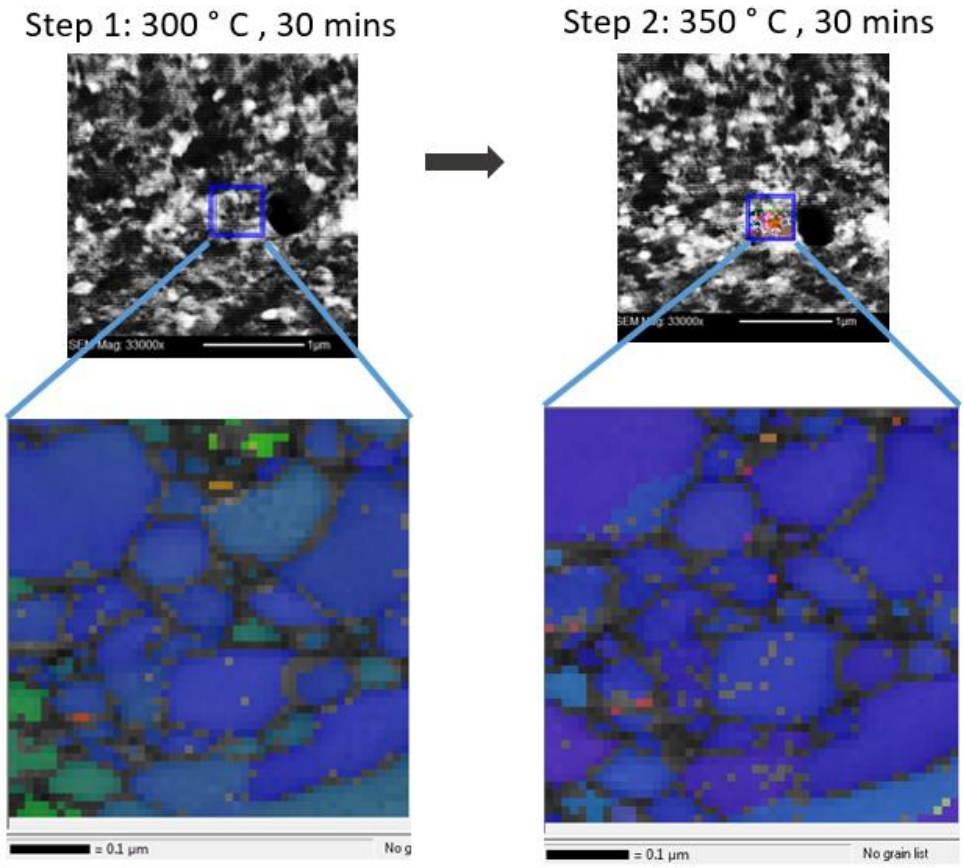

Figure 5-5: Top: SEM images of two step thermal treatment of Au film on TEM membrane along with their corresponding EBSD mapping (bottom) whose coloring scheme index is shown in Figure 5-4.

The observation from Figure 5-5 can be further explained with the statistics shown in Figure 5-6, which is a plot of the deviation (degrees) of the crystallographic orientation from <111> plotted against the relative frequency. The red curve shows the result of the first anneal step, whereas the black curve represents the result after both the anneal steps. While most of the grains (> 90%) are within 6° deviation from <111> for the first case, there is a rightward shift in this stat for the data obtained after the second anneal

step. More than 90% of the grains are within 9° deviation from <111> for this which suggests that some of the grains deviate farther from <111> upon the two-step thermal treatment.

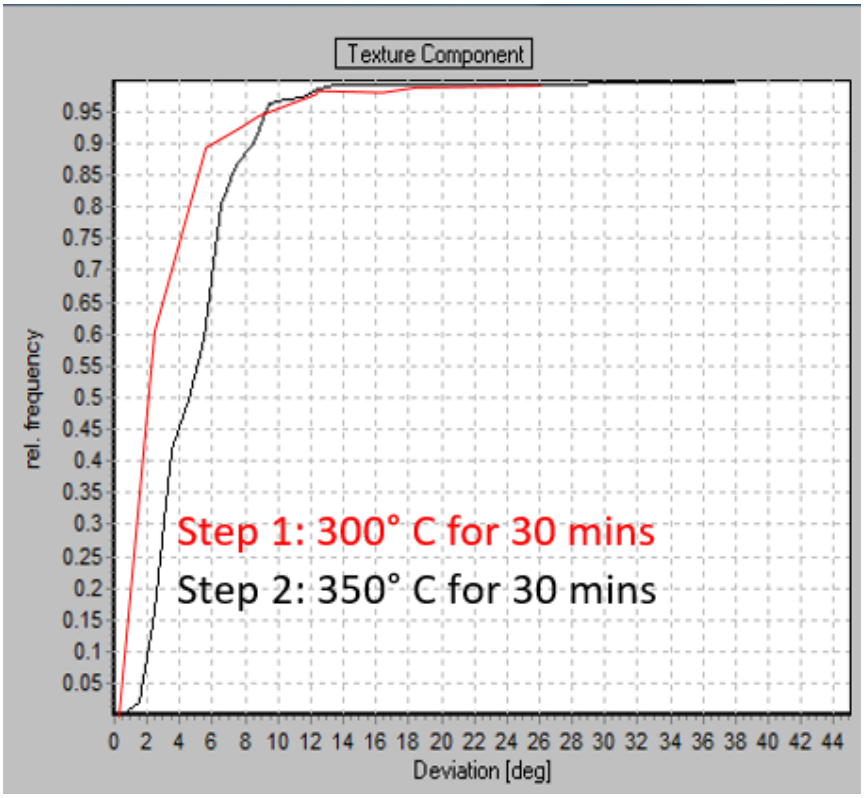

Figure 5-6: Deviation (degrees) of the grains from the <111> orientation plotted against relative frequency.

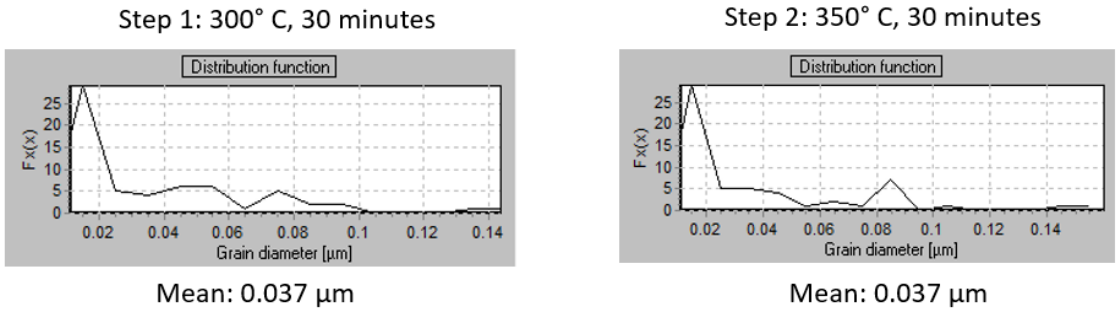

Figure 5-7: Average grain size statistics of the films annealed for the two step anneal experiment. Grain size plotted vs relative frequency.

Grain size and distribution was studied after each anneal. The result, which is shown in Figure 5-7 suggests that the grains remain fairly similar despite the change in texture.

5.4 Cantilever development and characterization

In order to develop and study a nanostructure of Au that closely resembled a plasmonic NFT for HAMR, the sheet films (25nm Au on 5nm thick Si_3N_4 windows) were patterned using focused ion beam (FIB) technique to create cantilever structures mimicking the NFTs for HAMR process. This is depicted in Figure 5-8.

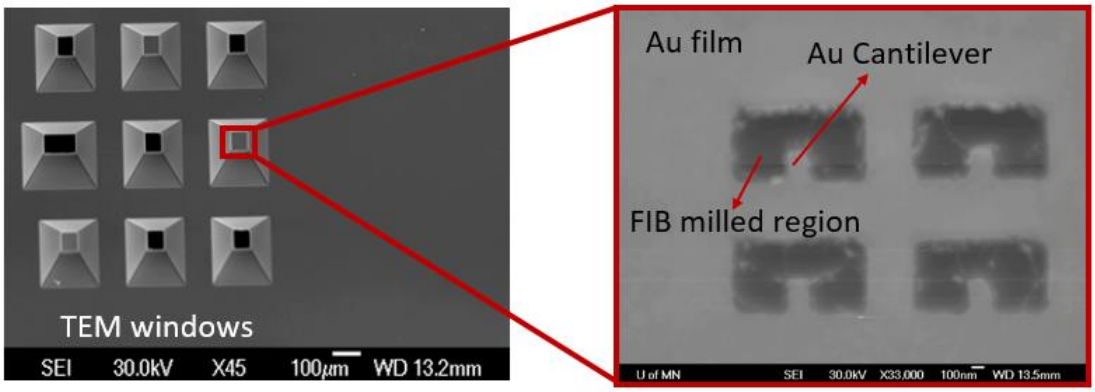

Figure 5-8: Left: TEM windows with 25nm Au films. Right: Au Cantilevers developed by FIB patterning.

T-EBSD of cantilevers was carried out after different heat treatments. Figure 5-9 summarizes the different temperature and time frames of the heat treatment along with their corresponding t-EBSD mapping result (bottom row).

As seen in Figure 5-9, heating the cantilevers at 200°C for 30 minutes produced very little indexing. 250°C for 30 minutes produced slightly better results, whereas a heat treatment at 300°C for 30 minutes significantly better mapping results without causing any deformation to the cantilever.

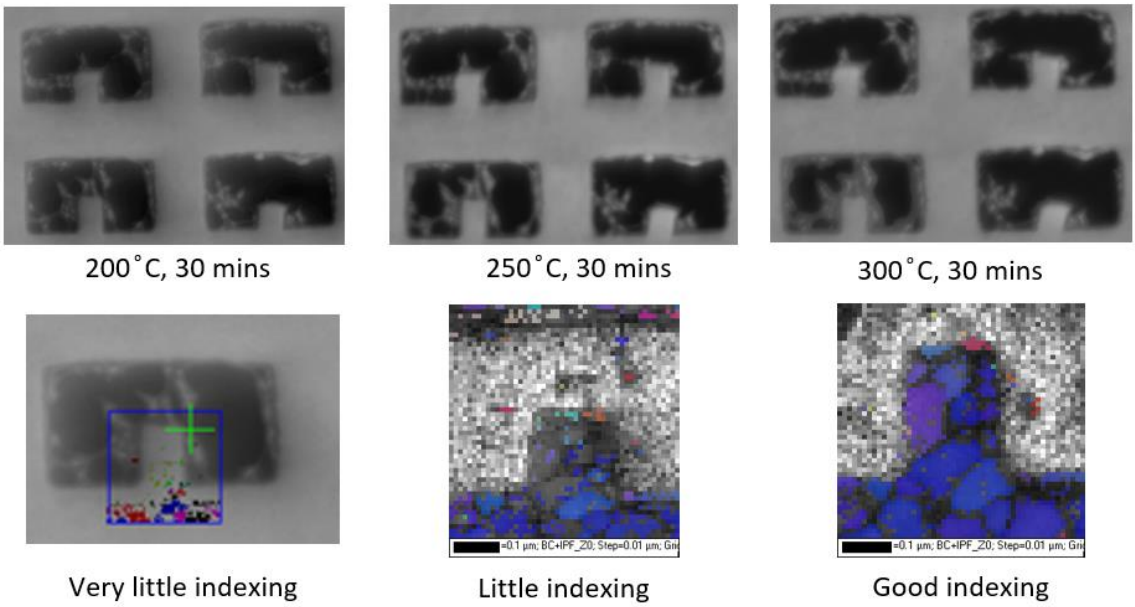

Figure 5-9: Top: Cantilevers after heat treatment at different temperatures. Bottom: Corresponding EBSD mapping/indexing. Better crystallinity and/or grain growth yields better indexing.

However, a thermal treatment at an elevated temperature of 400°C for 30 minutes led to different degrees of deformation in different cantilevers (Figure 5-10). The deformation of the cantilevers was categorized in 3 groups; (1) Undeformed, where cantilevers remain 100% intact upon the thermal treatment (2) Moderately deformed, where more than 50% remains intact and (3) heavily deformed, in which case less than 50% of the cantilever remains. An example of this classification is shown in Figure 5-10.

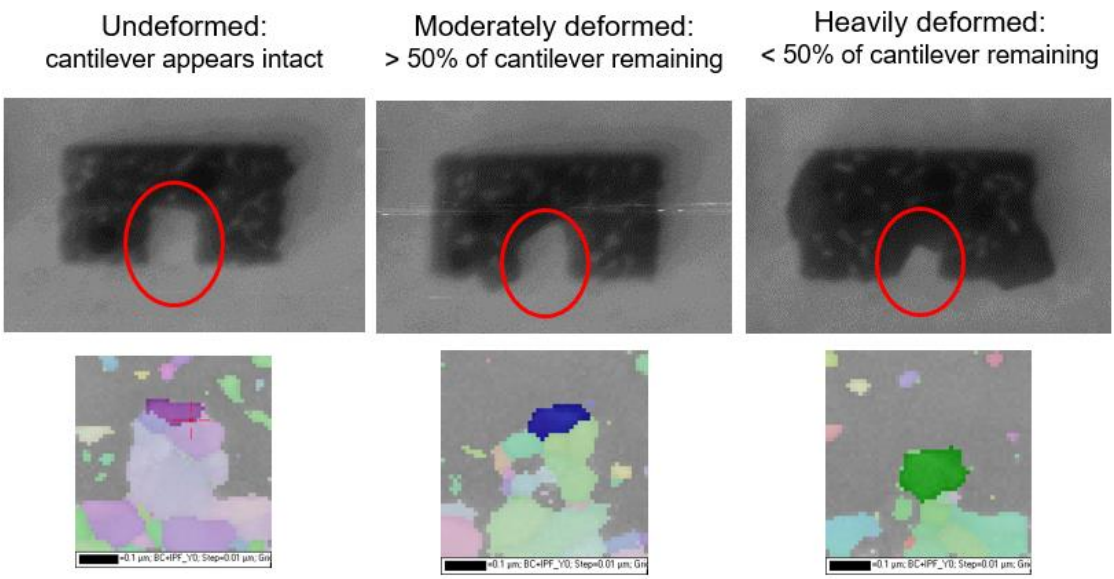

Figure 5-10: Top: SEM images showing different degrees of deformation of the cantilevers and their corresponding EBSD mapping (bottom). All samples heated at 400°C for 30 minutes.

5.5 Cantilever deformation statistics

As seen from Figure 5-10, the deformation of the cantilever starts from the edges, which means that the stability of edges is vital for the overall stability of the cantilever. Statistics was taken from 50 individual edge grains of different cantilevers (all degrees of deformation) which was possible due to the capability of the EBSD's post processing software. Size and crystallographic texture of the individual grains were analyzed. Figure 5-11 shows an example of this, where, only the edge grains (x, y direction, highlighted in dark blue and green) were selected for further analysis.

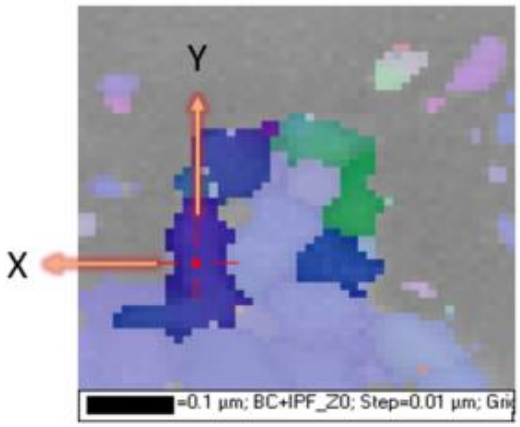

Figure 5-11: t-EBSD mapping showing edge grains of the cantilever (highlighted) and the in-plane directions.

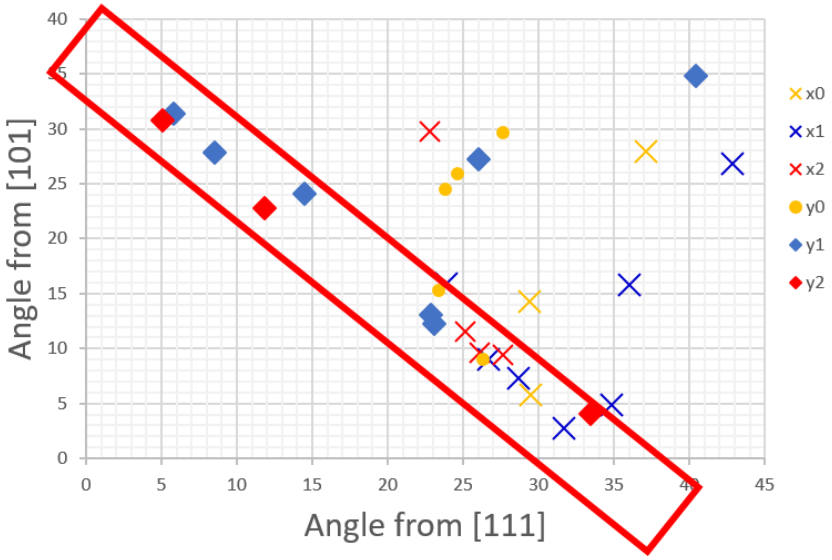

Figure 5-12: Edge grain statistics. X axis denotes deviation of the grains from [111] whereas y axis denotes the deviation from [101].

Figure 5-12 shows a graph in which the deviation from [111] direction is plotted against deviation angle from [101] for all 50 edge grains sampled. Here, the index (x0,x1,x2) and (y0, y1, y2) correspond to the grains that were deformed at different degrees (0-undeformed, 1-moderately deformed and 2-heavily deformed) in the x and y directions.

Most of the data points lie along the [101] and [111] orientations which is highlighted by the red box in Figure 5-12.

$$\cos\varphi = \frac{h_1h_2 + k_1k_2 + l_1l_2}{\sqrt{{h_1}^2 + {k_1}^2 + {l_1}^2}\sqrt{{h_2}^2 + {k_2}^2 + {l_2}^2}}$$

Equation 5.1: Equation used to find angle between [111] and [101] (edge grains)

Further analysis involved calculation to find the angle (φ) between [101] and [111]. This was done using the relation in Equation 5.1. This operation resulted in a value of ≈35° or, 10° off of the <111> orientation. This suggests that most of the grains that remained intact till the end were the ones that were deviated 10° of <111> in the z direction. This analysis suggests that if the NFTs can be developed in such a way that the Au grains are oriented at a 10 ° deviation from <111> in the z direction, that would result in the most thermally stable NFTs for HAMR technology.

6 Conclusion

Development of magneto-optical materials for isolator applications comprised most this work. Ce and Bi doped YIG films have dominated the field of magneto-optical materials for photonic non-reciprocal devices. However, these films require undoped YIG seedlayers when integrated with non-garnet substrates. Simulations done in this work show that these seedlayers can significantly counteract the non-reciprocity brought about by the doped garnets in SOI devices. Simulations were also used to compare modal interactions with various published MO cladding/seedlayer pairs, and the best monolithic cladding to date which uses 45nm YIG seedlayers to produce Ce:YIG with -3700°/cm of Faraday rotation [21]. To mitigate seedlayer issues, three new seedlayer-free garnets; TIG, Bi:TIG and Ce:TIG were presented here. These garnets can be used as single-layer claddings for ease of manufacturing with either positive or negative nonreciprocity and Bi:TIG was shown to be an excellent seedlayer for Ce:YIG with matching chirality. Furthermore, TIG, Bi:TIG and Ce:TIG were successfully grown on lower refractive index fused quartz substrates, so they can be easily used in garnet-core devices with push-pull quasi phase matching to eliminate birefringence effects. This novel idea of using two different materials with opposite MO chirality has opened doors for the reduction in device footprint while also allowing for the polarization-diverse (TE-TM) isolators.

In addition to novel materials development and device simulations, our collaborative effort with Dr. Cui Zhang and Prof. David Hutchings at the School of Engineering, University of Glasgow has resulted in the development of an on-chip integrated TE-

mode SOI isolator. This is an important step in achieving new applications for photonic integrated circuits. These FR isolators are simple 2-component 1D (all in-line) waveguides with unique QPM claddings to overcome waveguide birefringence. Compared to non-reciprocal phase-shift (NRPS) devices, the design is sublimely simple, and the garnet claddings can be saturated at lower applied magnetic fields due to the longitudinal nature of FR which matches the garnet shape anisotropy. The devices presented here are also the only nonreciprocal devices to have used only lithography with sputter deposition, which are the workhorse processes in the semiconductor, hard drive, and photonics industries. This is a significant improvement in potential for commercial upscaling compared to the other garnet-integration methods of pulsed laser deposition and wafer bonding.

Integrating the idea of Fabry-Perot interferometers with Faraday rotators is a novel idea whose proof of concept was explored as a part of this work. Preliminary results show that while there is a lot of work needed to develop a device to work in a targeted wavelength, it is possible to achieve a significant enhancement of Faraday rotation by this approach. Success of this work will lead to the development of highly efficient, easily upscaled optical isolators.

The last part of this work was dedicated to the study of the relationship between the crystallographic orientations of Au films with the thermal stability of Au near field transducers (NFTs) for heat assisted magnetic recording. HAMR technology involves heating nano-spots on the recording medium exploiting the plasmonic capabilities of Au NFTs. Upon heating, the Au NFTs undergo structural deformation. This leads to changes

in the resonance frequency, which is critical for writing. Thus, the understanding of the morphology and deformation of gold nanoparticles is essential for the success of HAMR. Study of the deformation of gold using electron backscattered diffraction techniques show that the as-deposited films are highly textured in the <111> orientation in the direction perpendicular to the film. Upon heating, the grains tend to deviate slightly from <111>. Cantilever patterns that mimic the NFT structures were created using focused ion beam. Experiments involving thermal treatments were carried out while tracking the change in the size and orientation of the individual NFT grains. Results showed that the grains that withstood more thermal treatment compared to the rest were the ones that were oriented at an angle of 10° from <111> in the z direction. This suggested that if the films can be grown at a deviation at 10° from <111>, that would result in the most thermally stable grains and hence the most stable Au NFTs for HAMR.

7 Bibliography

[1] Intel, “What happens in an internet minute?” [Online]. Available: http://www.intel.com/content/dam/www/public/us/en/images/illustrations/embedded-infographic-600-logo.jpg. [Accessed: 01-Jan-2017].

[2] P. A. Gargini, “How to Successfully Overcome Inflection Points, or Long Live Moore’s Law,” *Comput. Sci. Eng.*, vol. 19, no. 2, pp. 51–62, 2017.

[3] E. Grochowski and R. D. Halem, “Technological impact of magnetic hard disk drives on storage systems,” *IBM Syst. J.*, vol. 42, no. 2, pp. 338–346, 2003.

[4] Seagate, “Seagate 12TB Enterprise hard disk drives,” 2017. [Online]. Available: http://www.seagate.com/enterprise-storage/hard-disk-drives/enterprise-capacity-3-5-hdd-10tb/. [Accessed: 01-Jan-2017].

[5] Z. Bandic and R. H. Victora, “Advances in Magnetic Data Storage Technologies,” *Proc. IEEE*, vol. 96, no. 11, pp. 1749–1753, 2008.

[6] A. Ghatak and K. Thyagarajan, *An introduction to fiber optics*. Cambridge university press, 1998.

[7] National research council of the national academies, *Optics and photonics; Essential technologies for our nation*. National Academic Press, 2013.

[8] L. C. Kimerling, “Silicon microphotonics,” *Appl. Surf. Sci.*, pp. 8–13, 2000.

[9] IBM, “IBM Silicon Photonics,” *News release*, 2015. [Online]. Available: https://www-03.ibm.com/press/us/en/photo/46840.wss.

[10] Intel, “100G Parallel Single Mode Data Center Connectivity,” *Product Brief*, 2016. [Online]. Available: www.intel.com/siliconphotonics.

[11] M. J. Paniccia, “A perfect marriage : optics and silicon,” *Optoelectronics*, no. 2, pp. 34–38, 2011.

[12] Y. A. Vlasov, “Silicon CMOS-Integrated Nano-Photonics for Computer and Data Communications Beyond 100G,” *IEEE Commun. Mag.*, no. February, pp. 67–72, 2012.

[13] B. J. H. Stadler and T. Mizumoto, “Integrated Magneto-Optical Materials and Isolators: A Review,” *IEEE Photonics J.*, vol. 6, no. 1, pp. 1–15, Feb. 2014.

[14] R. Lang and K. Kobayashi, “External Optical Feedback Effects on Semiconductor Injection Laser Properties,” *IEEE J. Quantum Electron.*, vol. QE-16, no. 3, pp. 347–354, 1980.

[15] Newport, “High power Faraday optical isolators.” [Online]. Available: https://www.newport.com/f/high-power-faraday-optical-isolators. [Accessed: 01-Jan-2017].

[16] S.-Y. Sung, “Integrating magneto-optical garnet isolators on semiconductor substrates.,” University of Minnesota, 2008.

[17] C. A. Ross, T. Tepper, and Y. Avrahami, “Magnetooptical isolator material,” US7006289 B2, 2002.

[18] M. Yanaga, Y. Shoji, Y. Takamura, S. Nakagawa, and T. Mizumoto, “Compact magnetooptical isolator with cobalt ferrite on silicon photonic circuits,” *Appl. Phys. Express*, vol. 8, no. 8, p. 82201, 2015.

[19] J. F. Dillon, “Origin and uses of the faraday rotation in magnetic crystals,” *J. Appl. Phys.*, vol. 39, no. 2, pp. 922–929, 1968.

[20] T. Sekijima, H. Kishimoto, T. Fuji, K. Wakino, and M. Okada, “Magnetic, optical and microwave properties of rare-earth-substituted fibrous yttrium iron garnet single crystals grown by floating zone method,” *Jpn. J. Appl. Phys.*, vol. 38, no. 10R, pp. 5874–5878, 1999.

[21] A. D. Block, P. Dulal, B. J. H. Stadler, and N. C. a. Seaton, “Growth Parameters of Fully Crystallized YIG, Bi:YIG, and Ce:YIG Films With High Faraday Rotations,” *IEEE Photonics J.*, vol. 6, no. 1, pp. 1–8, Feb. 2014.

[22] X. Y. Sun *et al.*, “Single-Step Deposition of Cerium-Substituted Yttrium Iron Garnet for Monolithic On-Chip Optical Isolation,” *ACS Photonics*, vol. 2, no. 7, pp. 856–863, 2015.

[23] T. Shintaku and T. Uno, “Optical waveguide isolator based on nonreciprocal radiation,” *J. Appl. Phys.*, vol. 8155, 1994.

[24] P. K. Tien, R. J. Martin, S. L. Blank, S. H. Wemple, and L. J. Varnerin, “Optical waveguides of single-crystal garnet films,” *Appl. Phys. Lett.*, vol. 21, no. 5, pp. 207–209, 1972.

[25] V. Fratello and R. Wolfe, “Epitaxial Garnet Films for Nonreciprocal Magneto-Optic Devices,” in *Handbook of Thin Film Devices*, no. January, Academic Press, 2000, pp. 93–141.

[26] P. K. Tien, R. J. Martin, R. Wolfe, R. C. Le Craw, and S. L. Blank, “Switching and modulation of light in magneto-optic waveguides of garnet films,” *Appl. Phys. Lett.*, vol. 21, no. 8, pp. 394–396, 1972.

[27] A. Murata, N. Koshizuka, T. Okuda, K. Ando, A. Ito, and K. Kawanishi, “Guided-

wave properties and mode conversions in $(BiNdLu)_3$ $(FeAlLu)_5O_{12}$ films," *IEEE Trans. Magn.*, vol. MAG-21, pp. 1657–1659, 1985.

[28] R. Wolfe *et al.*, "Thin-film waveguide magneto-optic isolator," *Appl. Phys. Lett.*, vol. 46, no. 9, pp. 817–819, 1985.

[29] H. Yokoi and T. Mizumoto, "Proposed configuration of integrated optical isolator employing wafer-direct bonding technique," *Electron. Lett.*, vol. 33, pp. 1787–1788, 1997.

[30] S. F. B. Morse, *Samuel F. B. Morse, His Letters and Journals In Two Volumes, Volume II.* Cambridge University Press, 2004.

[31] K. J. Anderson, "Magnetic Recording Materials," *MRS Bull.*, vol. 15, pp. 88–91, 1990.

[32] A. Moser *et al.*, "Magnetic recording: advancing into the future," *J. Phys. D. Appl. Phys.*, vol. 35, no. 19, pp. R157–R167, 2002.

[33] B. M. H. Kryder *et al.*, "Heat assisted magnetic recording," *Proc. IEEE*, vol. 96, no. 11, 2008.

[34] W. a. Challener *et al.*, "Heat-assisted magnetic recording by a near-field transducer with efficient optical energy transfer," *Nat. Photonics*, vol. 3, no. 4, pp. 220–224, Mar. 2009.

[35] W. A. Challener, T. W. McDaniel, C. D. Mihalcea, K. R. Mountfield, K. Pelhos, and I. K. Sendur, "Light delivery techniques for heat-assisted magnetic recording," *Japanese J. Appl. Physics, Part 1 Regul. Pap. Short Notes Rev. Pap.*, vol. 42, no. 2 B, pp. 981–988, 2003.

[36] D. Weller and A. Moser, “Thermal effect limits in ultrahigh-density magnetic recording,” *IEEE Trans. Magn.*, vol. 35, no. 6, pp. 4423–4439, 1999.

[37] O. Hellwig *et al.*, “Heat Assisted Magnetic Recording Media : Progress and Remaining Challenges,” *INTERMAG 2015, Beijing, China*, 2015. [Online]. Available: https://www.tu-chemnitz.de/physik/MAGFUN/dokumente/poster_HAMR.pdf.

[38] N. Zhou *et al.*, “Plasmonic near-field transducer for heat-assisted magnetic recording,” *Nanophotonics*, vol. 3, no. 3, pp. 141–155, 2014.

[39] G. Bräuer, B. Szyszka, M. Vergöhl, and R. Bandorf, “Magnetron sputtering - Milestones of 30 years,” *Vacuum*, vol. 84, no. 12, pp. 1354–1359, 2010.

[40] P. J. Kelly and R. D. Arnell, “Magnetron sputtering : a review of recent developments and applications,” *Vacuum*, vol. 56, pp. 159–172, 2000.

[41] M. Ohring, *Materials Science of Thin Films*. Academic Press, 2001.

[42] S. Kalpat and K. Uchino, “Highly oriented lead zirconium titanate thin films: Growth, control of texture, and its effect on dielectric properties,” *J. Appl. Phys.*, vol. 90, no. 6, pp. 2703–2710, 2001.

[43] S.-Y. Sung, X. Qi, and B. J. H. Stadler, “Integrating yttrium iron garnet onto nongarnet substrates with faster deposition rates and high reliability,” *Appl. Phys. Lett.*, vol. 87, no. 12, p. 121111, 2005.

[44] S.-Y. Sung, A. Sharma, A. Block, K. Keuhn, and B. J. H. Stadler, “Magneto-optical garnet waveguides on semiconductor platforms: Magnetics, mechanics, and photonics,” *J. Appl. Phys.*, vol. 109, no. 7, p. 07B738, 2011.

[45] W. D. Callister and D. G. Rethwisch, *Materials science and engineering: an*

introduction. New York: Wiley, 2007.

[46] "Bruker D8 Discover User Manual," *University of Minnesota College of Science and Engineering Characterization Facility*, 2012. [Online]. Available: http://www.charfac.umn.edu/instruments/Bruker_D8_Discover_2D_Manual_v2012.08.08.pdf. [Accessed: 01-Jan-2017].

[47] B. B. He, U. Preckwinkel, and K. L. Smith, "Fundamentals of two-dimensional X-RAY diffraction," *JCPDS-International Cent. Diffr. Data 2000,Advances X-ray*, vol. 43, pp. 273–280, 2000.

[48] L. Bi, "Magneto-optical oxide thin films and integrated nonreciprocal photonic devices," Massachusetts Institute of Technology, 2011.

[49] E. C. Estrine, "Development and Characterization of Magnetostrictive GaFe and Plasmonic Gold Thin Films," University of Minnesota, 2015.

[50] "Perkin Elmer LAMBDA 650 / 850 / 950 Hardware Guide," *UV-VIS Spectroscopy*, 2004. [Online]. Available: http://mdi.as.nyu.edu/docs/CP/4738/UV.pdf.

[51] M. A. Green and M. J. Keevers, "Optical properties of intrinsic silicon at 300 K," *Prog. Photovoltaics*, vol. 3, pp. 189–192, 1995.

[52] D. C. Hutchings *et al.*, "Quasi-Phase-Matched Faraday Rotation in Semiconductor Waveguides With a Magnetooptic Cladding for Monolithically Integrated Optical Isolators," *IEEE Photonics J.*, vol. 5, no. 6, pp. 6602512–6602512, Dec. 2013.

[53] D. C. Hutchings and B. M. Holmes, "A waveguide polarization toolset design based on mode beating," *IEEE Photonics J.*, vol. 3, no. 3, pp. 450–461, 2011.

[54] C. Zhang, "Integrated Waveguide Optical Isolator," University of Glasgow, 2017.

[55] M. Razeghi, P. L. Meunier, and P. Maurel, “Growth of GaInAs-InP multiquantum wells on garnet (GGG=$Gd_3Ga_5O_{12}$) substrate by metalorganic chemical vapor deposition,” *J. Appl. Phys.*, vol. 59, pp. 2261–2263, 1986.

[56] T. Mizumoto, Y. Shingai, Y. Miyamoto, and Y. Naito, “Crystal Growth of InP on a $Gd_3Ga_5O_{12}$ Substrate by Organometallic Chemical Vapor Deposition,” *Jpn. J. Appl. Phys.*, vol. 29, pp. 53–57, 1990.

[57] H. Yokoi, T. Mizumoto, K. Maru, and Y. Naito, “Direct bonding between InP and rare earth iron garnet grown on $Gd_3Ga_5O_{12}$ substrate by liquid phase epitaxy,” *Electron. Lett.*, vol. 31, no. 18, pp. 1612–1613, 1995.

[58] B. Stadler, K. Vaccaro, P. Yip, J. Lorenzo, Y.-Q. L. Y.-Q. Li, and M. Cherif, “Integration of magneto-optical garnet films by metal-organicchemical vapor deposition,” *IEEE Trans. Magn.*, vol. 38, no. 3, pp. 1564–1567, 2002.

[59] L. Bi, J. Hu, G. F. Dionne, L. Kimerling, and C. A. Ross, “Monilithlic integration of chalcogenide glass/iron garnet waveguides and resonators for on-chip non reciprocal photonic devices,” *Int. Soc. Opt. Photonics.*, vol. 7941, pp. 794105-794105–10, Feb. 2011.

[60] M. Gomi, H. Furuyama, and M. Abe, “Strong magneto-optical enhancement in highly Ce-substituted iron garnet films prepared by sputtering,” *J. Appl. Phys.*, vol. 70, no. 11, p. 7065, 1991.

[61] Y. Shoji, T. Mizumoto, H. Yokoi, I. W. Hsieh, and R. M. Osgood, “Magneto-optical isolator with silicon waveguides fabricated by direct bonding,” *Appl. Phys. Lett.*, vol. 92, no. 7, 2008.

[62] M.-C. Tien, T. Mizumoto, P. Pintus, H. Kromer, and J. E. Bowers, “Silicon ring isolators with bonded nonreciprocal magneto-optic garnets.,” *Opt. Express*, vol. 19, no. 12, pp. 11740–11745, 2011.

[63] S. Ghosh, S. Keyvavinia, W. Van Roy, T. Mizumoto, G. Roelkens, and R. Baets, “Ce:YIG/Silicon-on-Insulator waveguide optical isolator realized by adhesive bonding.,” *Opt. Express*, vol. 20, no. 2, pp. 1839–48, Jan. 2012.

[64] L. Bi *et al.*, “On-chip optical isolation in monolithically integrated non-reciprocal optical resonators,” *Nat. Photonics*, vol. 5, no. 12, pp. 758–762, 2011.

[65] X. Y. Sun *et al.*, “Single-Step Deposition of Cerium-Substituted Yttrium Iron Garnet for Monolithic On-Chip Optical Isolation,” *ACS Photonics*, vol. 2, no. 7, pp. 856–863, 2015.

[66] T. Shintaku, A. Tate, and S. Mino, “Ce-substituted yttrium iron garnet films prepared on GdScGaO garnet substrates by sputter epitaxy,” *Appl. Phys. Lett.*, vol. 71, no. March, p. 1640, 1997.

[67] S. Geller, “Crystal chemistry of the garnets,” *Zeitschrift für Krist. Mater.*, vol. 125, pp. 1–47, 1967.

[68] G. P. Espinosa, “Crystal Chemical Study of the Rare-Earth Iron Garnets,” *J. Chem. Phys.*, vol. 37, pp. 2344–2347, 1962.

[69] G. Winkler, “Magnetic garnets,” in *Vieweg tracts in pure and applied physics,volume 5*, Braunschweig ; Wiesbaden : Vieweg, 1981.

[70] P. Dulal *et al.*, “Optimized Magneto-optical Isolator Designs Inspired by Seedlayer-Free Terbium Iron Garnets with Opposite Chirality,” *ACS Photonics*, vol. 3, no. 10,

pp. 1818–1825, 2016.

[71] Y. Shoji, Y. Shirato, and T. Mizumoto, “Silicon Mach-Zehnder interferometer optical isolator having 8 nm bandwidth for over 20dB isolation,” *Jpn. J. Appl. Phys.*, vol. 53, no. 2 PART 1, 2014.

[72] R. Wolfe, J. Hegarty, J. Dillon, L. Luther, G. Celler, and L. Trimble, “Magneto-optic waveguide isolators based on laser annealed (Bi, Ga) YIG films,” *IEEE Trans. Magn.*, vol. 21, no. 5, pp. 1647–1650, 1985.

[73] S. K. Mondal and B. J. H. Stadler, “Novel designs for integrating YIG/air photonic crystal slab polarizers with waveguide Faraday rotators,” *IEEE Photonics Technol. Lett.*, vol. 17, no. 1, pp. 127–129, 2005.

[74] Y. Shoji, A. Fujie, and T. Mizumoto, “Silicon Waveguide Optical Isolator Operating for TE Mode Input Light,” *IEEE J. Sel. Top. Quantum Electron.*, no. c, pp. 1–1, 2016.

[75] S. Ghosh, S. Keyvaninia, Y. Shirato, T. Mizumoto, G. Roelkens, and R. Baets, “Optical isolator for TE polarized light realized by adhesive bonding of Ce:YIG on silicon-on-insulator waveguide circuits,” *IEEE Photonics J.*, vol. 5, no. 3, 2013.

[76] P. Pintus, F. Di Pasquale, and J. E. Bowers, “Integrated TE and TM optical circulators on ultra-low-loss silicon nitride platform.,” *Opt. Express*, vol. 21, no. 4, pp. 5041–52, 2013.

[77] B. M. Holmes and D. C. Hutchings, “Demonstration of quasi-phase-matched nonreciprocal polarization rotation in III-V semiconductor waveguides incorporating magneto-optic upper claddings,” *Appl. Phys. Lett.*, vol. 88, no. 2006, pp. 3–5, 2006.

[78] R. Wolfe, V. J. Fratello, and M. McGlashan Powell, “Thin-film garnet materials with zero linear birefringence for magneto-optic waveguide devices.,” *J. Appl. Phys.*, vol. 63.8, pp. 3099–3103, 1988.

[79] S. J. Licht, “Technique for controlled adjustment of bubble collapse field in epitaxial garnet films by etching.,” *J. Electron. Mater.*, vol. 4.4, pp. 757–768, 1975.

[80] A. Q. Wu *et al.*, “HAMR Areal Density Demonstration of 1 + Tbpsi on Spinstand,” vol. 49, no. 2, pp. 779–782, 2013.

[81] S. Inasawa, M. Sugiyama, and Y. Yamaguchi, “Laser-induced shape transformation of gold nanoparticles below the melting point: The effect of surface melting,” *J. Phys. Chem. B*, vol. 109, no. 8, pp. 3104–3111, 2005.

[82] Z. L. Wang, M. B. Mohamed, S. Link, and M. A. El-sayed, “Crystallographic facets and shapes of gold nanorods of di ff erent aspect ratios,” vol. 440, 1999.

[83] Y. Golan, L. Margulis, and I. Rubinstein, “Vacuum-deposited gold films I. Factors affecting the film morphology,” *Surf. Sci.*, vol. 264, no. 3, pp. 312–326, Mar. 1992.

[84] S. Link, Z. L. Wang, and M. a. El-Sayed, “How Does a Gold Nanorod Melt?,” *J. Phys. Chem. B*, vol. 104, no. 33, pp. 7867–7870, Aug. 2000.

[85] L. Vitos, A. V. Ruban, H. L. Skriver, and J. Kollár, “The surface energy of metals,” *Surf. Sci.*, vol. 411, no. 1–2, pp. 186–202, 1998.

[86] E. Estrine, N. Seaton, P. Dulal, and B. Stadler, “Transmission Electron Backscatter Diffraction (tEBSD) analysis of Au Thin Films,” in *Microscopy and microanalysis*, 2015, vol. 21, pp. 1671–1672.